UNIVERSIDAD POLITÉCNICA DE VALENCIA

DEPARTAMENTO INGENIERIA MECÁNICA Y MATERIALES

UNIVERSITAT POLITÈCNICA DE VALÈNCIA

Synthesis Of ZnO and TiO_2 By Biomimetization Of Eggshell Membranes And Its Evaluation As Anode In Dye-Sensitized Solar Cells

TESIS DOCTORAL.

AUTOR: Rubens Camaratta

DIRECTOR: Dr. Javier Orozco Messana

Septiembre 2018

To my Family and friends

“Little knowledge makes people feel proud. Much knowledge who feel humble.”
Leonardo Da Vinci

GREETINGS

This work could not be completed without the help of many people to whom I pay sincere tribute:

Firstly, Professor Dr. Javier Orozco Messana for his guidance and hospitality shown during the studies in Spain. Without his dedication and constant encouragement, this to PhD work could not be conclude.

Prof. Dr. Carlos Pérez Bergmann, because the excellent guidance, opportunity, full support, friendship and dedication demonstrated during the development of this work, as well as the eighteen years of living and continuous learning.

To PhD. Maria Dolores Tolosa Reyes for her friendship, hospitality and for her great contribution to the development of this thesis.

To Prof. PhD. Maria Ángeles Hernández Fenollosa for the friendship and the great help with the optical analysis performed in this thesis.

To my friend and colleague Álvaro Correia Lima Niedersberg who accompanied me in this thesis especially the time spent in Spain.

To my friend and colleague Felipe Antonio Lucca Sanchez because the indication to subscribe in the scholarship program Erasmus Mundus and because the help in the analysis of spectrofluorometry.

To my friend and colleague Lauren Arrusul Carús for the great help in editing the Figures and Tables in this thesis.

To all the staff and teachers from UPV (Polytechnic University of Valencia) who in one way or another contributed to this work, in particular, Fidel, Inma, Mari Carmen and Motaz, I express my deep gratitude.

To Federal University of Rio Grande do Sul to be public, free and with quality, as well as all teachers PPGE3M because the technical knowledge transmitted, and the deep friendships formed.

To Prof. Mario Lucio Moreira from Federal University of Pelotas (UFPel) who contributed for the characterization of the DSSCs.

To PhD students Luciano Timm Gularte and Cristian Dias Fernandes whom were fundamental to construct the solar cells and with great importance in the discussion of the photovoltaic characterization results.

To CAPES for the financial support for this work;

To the European program of scholarships Erasmus Mundus, that provided financial support of a doctoral scholarship of 22 months supporting the immeasurable experience of living in Valencia (Spain).

To all the people who work in Relinter (International Relations sector of UFRGS) and the area of international affairs at the UPV, especially Lizângela Guerra and Begoña Lluzar Julian.

And especially to my wife Camila Vizzotto Meinen, my parents, José Carlos Camaratta and Varna Regina Cortezia, and my brother Douglas Camaratta for their unconditional support.

RESUMEN:

Esta tesis presenta un conjunto original de procedimientos para la síntesis de nanoestructuras de TiO_2 y ZnO por biomimetización de membranas de cáscara de huevo obteniendo materiales valiosos para fotovoltaica como se muestra en su evaluación de rendimiento como ánodo en células solares sensibilizadas por colorante. "El manuscrito está dividido en 7 capítulos.

En el primer capítulo, titulado Introducción, se presentan las bases teóricas para la comprensión de los procesos de biomimetización, membranas de cáscara de huevo, síntesis de ZnO y TiO_2, y células solares sensibilizadas por colorantes (DSSC). Después del capítulo introductorio, el Capítulo 2 revela los objetivos generales y específicos de esta investigación. Posteriormente, el Capítulo 3 describe el procedimiento experimental utilizado para las síntesis y caracterizaciones de ZnO y TiO_2, así como el procedimiento utilizado en el ensamblaje y la caracterización de las células fotovoltaicas.

En el capítulo 4 se presentan y discuten los resultados obtenidos con las síntesis y la aplicación de los polvos como fotodoles en DSSC. En este capítulo, hemos decidido subdividirlo en secciones específicas para explicar cuestiones científicas específicas sobre el tema.

En el capítulo 5 se presentan las conclusiones del estudio en vista de los diferentes aspectos: obtención de TiO_2 biomimético y ZnO, diferencias entre los polvos sintetizados por biomimetización de las membranas de cáscara de huevo, y la caracterización de las células construidas con los polvos biomiméticos.

ABSTRACT:

This thesis introduces an original set of procedures for the Synthesis of ZnO and TiO_2 nanostructures by biomimetization of eggshell membranes obtaining valuable materiales for photovoltaic as shown on their performance evaluation as anode in Dye-Sensitized Solar Cells". The manuscript is divided into 7 chapters.

In the first chapter, entitled Introduction, it is presented the theoretical bases for the understanding of the biomimetization processes, eggshell membranes, ZnO and TiO_2 syntheses, and dye-sensitized solar cells (DSSC). After the introductory chapter, Chapter 2 reveals the general and specific objectives of this research. Subsequently, Chapter 3 describes the experimental procedure used for the syntheses and characterizations of ZnO and TiO_2 as well as the procedure used in the assembly and characterization of the photovoltaic cells.

In chapter 4 are presented and discussed the results obtained with the syntheses and application of the powders as photoanodes in DSSC. In this chapter, we have chosen to subdivide it into specific sections to explain specific scientific issues on the subject.

In chapter 5 the conclusions of the study are presented in view of the different aspects: obtaining ZnO and biomimetic TiO_2, differences between the powders synthesized by biomimetization of eggshell membranes, and the characterization of the cells constructed with the biomimetic powders.

RESUM:

Esta tesi presenta un conjunt original de procediments per a la síntesi de nanoestructuras de TiO_2 i ZnO per biomimetització de membranes de corfa d'ou obtenint materials valuosos per a fotovoltaica com es mostra en la seua avaluació de rendiment com a ànode en cèl·lules solars sensibilitzades per colorant.

El manuscrit està dividit en 7 capítols. En el primer capítol, titulat Introducció, es presenten les bases teòriques per a la comprensió dels processos de biomimetización, membranes de corfa d'ou, síntesi de ZnO i TiO_2, i cèl·lules solars sensibilitzades per colorants (DSSC) . Després del capítol introductori, el Capítol 2 revela els objectius generals i específics d'esta investigació. Posteriorment, el Capítol 3 descriu el procediment experimental utilitzat per a les síntesis i caracteritzacions de ZnO i TiO_2, així com el procediment utilitzat en l'acoblament i la caracterització de les cèl·lules fotovoltaiques.

En el capítol 4 es presenten i discutixen els resultats obtinguts amb les síntesis i l'aplicació de les pols com fotodoles en DSSC. En este capítol, hem decidit subdividir-ho en seccions específiques per a explicar qüestions científiques específiques sobre el tema. En el capítol 5 es presenten les conclusions de l'estudi en vista dels diferents aspectes: obtenció de TiO_2 biomimético i ZnO, diferències entre les pols sintetitzats per biomimetización de les membranes de corfa d'ou, i la caracterització de les cèl·lules construïdes amb les pols biomimétics.

LIST OF ABBREVIATIONS AND ACRONYMS

Acet CP – precipitated ZnO produced with zinc acetate

Acet RP - precipitated ZnO produced with zinc acetate residual solution

BET - Brunauer–Emmett–Teller

CBD - chemical bath deposition

CIGS - copper indium gallium selenide

CVD – chemical bath deposition

DLE – deep level emission

DNA - deoxyribonucleic acid

DTA - differential thermal analysis

DSSC – dye sensitized solar cell

EDS - energy dispersive system

ESD - electrostatic spray deposition

ESM – eggshell membranes

ESOP – excited state oxidation potencial

FTO - fluorine-doped tin oxide

FWHM - full width at half maximum

FURG – federal university of Rio Grande

HTM - hexametilenteramine

IM – inner membrane

ITO – indium tin oxide

LACER – laboratory of ceramic materials

LBZA - layered basic zinc acetate

LHZC - layered hydroxide zinc carbonate

LM – limiting membrane

NBE – near band edge

Nit CP – precipitated ZnO produced with zinc nitrate

Nit RP - precipitated ZnO produced with zinc nitrate residual solution

OM – outer membrane

PEG – polyethylene glycol

PVP - polyvinyl porrolidone

QD – quantum dots

QDSSC – quantum dots sensitized solar cell

SEM – scanning electron microscopy

SMU - source/measure unit

STC – standard test conditions

TBT - titanium tetra-n-butyl

TCO – transparent conductive oxide

TDA – thermodiferencial analysis

TEM – transmission electronic microscopy

TGA – thermogravimetric analysis

TG – thermogravimetric

UFPel – federal university of Pelotas

UFRGS – federal university of Rio Grande do Sul

UPV – polytechnic university of Valencia

UV-Vis -ultraviolet-visible

XRD – X-ray diffraction

Summary

1- Introduction 18

1.1 Biomimetics 18

1.1.1 Biomineralization 19

1.1.2 Biomorphic materials 22

1.1.3 Use of biotemplates to obtain nanomaterials 25

1.1.4 Use of eggshell membranes as biotemplates 26

1.1.5 Synthesis of ZnO and TiO_2 by biomimetization of eggshell membranes 27

1.1.6 The eggshell and its membranes 28

1.2 Zinc oxide (ZnO) 30

1.2.1 ZnO synthesis methods 32

1.2.2 Preparation of ZnO nanoparticles by chemical routes 32

1.2.3 Preparation of thin films of ZnO 35

1.2.4 ZnO Synthesis with the use of eggshell membranes as a biotemplate 38

1.3 TIitanium Dioxide (TiO_2) 43

1.3.1 TiO_2 synthesis by solution routes 45

1.3.2 Synthesis of macroporous TiO_2 networks 48
1.3.3 Biomimetic synthesis of TiO_2 49
1.3.4 Synthesis of TiO_2 using ESM as biotemplates 50
1.4 The functioning of the DSSC 52
1.4.1 Improvements in DSSC 53
1.4.2 The use of ZnO and TiO_2 as electrodes in DSSC 59
1.4.3 Solar cell measurement parameters 62
2- Objectives 67
2.1 Objective of the thesis 68
3- Experimental Procedure 69
3.1 Materials 71
3.2 Methods 72
3.2.1 Synthesis of ZnO and TiO_2 72
3.2.2 Preparation of the photovoltaic devices 74
3.3 Characterizations 76
3.3.1 Loss of mass and thermodiferencial analysis 76
3.3.2 X-ray Diffraction 76
3.3.3 Morphology 78
3.3.4 Optical properties 78
3.3.5 Surface area analysis 79
3.3.6 Chemical composition analysis 80
3.3.7 Photovoltaic characterizations 80
4- Results and Discussion 81
4.1 Morphologic study of the eggshell 81
4.2 Morphological differences between TiO_2 powders produced with different membranes 84

4.3 Decomposition of the in natura and hybrid membranes with titanium (effect of the firing atmosphere)..... 86

4.4 Decomposition of hybrid membranes prepared with different sources of zinc..... 88

4.5 Effect of the thermal treatment temperature on the phase formation of biomimetic TiO_2 89

4.6 Effect of the thermal treatment temperature on the phases formation for biomimetic and precipitated ZnO..... 92

4.7 Effect of thermal treatment temperature on the morphology of biomimetic oxides 96

4.8 Identification of contaminants of biomimetic ZnO..... 99

4.9 Optical properties of biomimetic TiO_2 thermal treated in different temperatures 103

4.10 Optical properties of biomimetic ZnO thermal treated in different temperatures 105

4.11 Surface area and porosity of biomimetic TiO_2 111

4.12 Characterization of biomimetic and commercial powders used for DSSC production 112

4.13 Characterization of the DSSC produced with biomimetic and commercial powders..... 118

5- Conclusions 122

6- References..... 125

7- Future works 139

1-Introduction

1.1 Biomimetics

The concept of getting ideas from nature and implementing them in technology is known as biomimetics and has awakened particular interest in the development of materials at the nanoscale (Lagziel-Simis et al., 2006). Reis (2003) suggests that biomimicry is a very important field of science that studies how nature designs, processes, and assembles/disassembles blocks for the manufacture of composite mineral/high performance polymers (e.g. mollusk shells, teeth, bones, etc.) and/or soft materials (cartilage, skin, tendons) and then tries to transfer these processes to obtain new molecules and materials with unique properties for use in engineering.

Engineers, scientists and artists have looked to nature for inspiration for a long time. During the nineteenth century, biomimetics was used with aesthetic purposes. An example of this can be seen in the entrance gate to the World Fair in Paris of 1900 (Figure 1-1). The designer responsible for the project, René Binet, claimed that his inspiration, from the overall composition

to the smallest details, was Ernst Haeckel's study on radiolarians (Ball, 2001).

Figure 1-1. Entrance created by René Binet for the World Fair held in Paris in 1900, inspired by the drawings of radiolarians (Ball, 2001).

1.1.1 Biomineralization

The term biomineralization is defined by the formation of minerals by organisms. This is a widespread phenomenon in various creatures, from microorganisms to vertebrates. The morphological aspects of biominerals usually differ from its inorganic counterparts, just as is the case for its mechanical properties, chemical composition and stability. This is a consequence of the differences in the environments where precipitation occurs and, in particular, the presence of biological macromolecules that are activated during the process of biomineralization (Aizenberg, 2006).

Biomineralization processes are largely dominated by macromolecules whose complementarity with the surface structure is the basis for pattern recognition molecules. This

complementarity may result in the control of crystal growth and morphology, or in inducing the nucleation of a crystal. These macromolecules may be involved in a wide variety of functions, such as in cell adhesion, ion transport, construction of the matrix, crystal nucleation and crystal growth control (Addadi et al., 2001).

Most of the mineralized tissue consists of crystalline materials. These crystalline materials are formed inside of organisms, both under normal conditions and pathological conditions. When formed in normal conditions, the inorganic crystals are used by the body to perform different functions, the most common of these provide rigidity to parts of the skeleton (Addadi et al., 2001).

Functions of these biological mineralized materials include a supporting skeleton in vertebrates, spikes in marine animals, shells to protect soft tissues, such as in clams, egg shells, shells from crustaceans, and the teeth for grinding food of many vertebrates and invertebrates (Addadi et al., 2001). Although a wide variety of minerals are used, most skeletons produced by organisms are constituted of stable forms of calcium carbonate - calcite and / or aragonite (Aizenberg, 2006).

Organisms use two main strategies to design their calcite skeletons. In the first strategy, crystals are used as a stiffening agent in a preformed organic matrix. As a result, a composite material, such as the shells of mollusks, is formed (Figure 1-2). Such ceramic structures are widely used by humans in the manufacture of synthetic composites (Douglas, 2003).

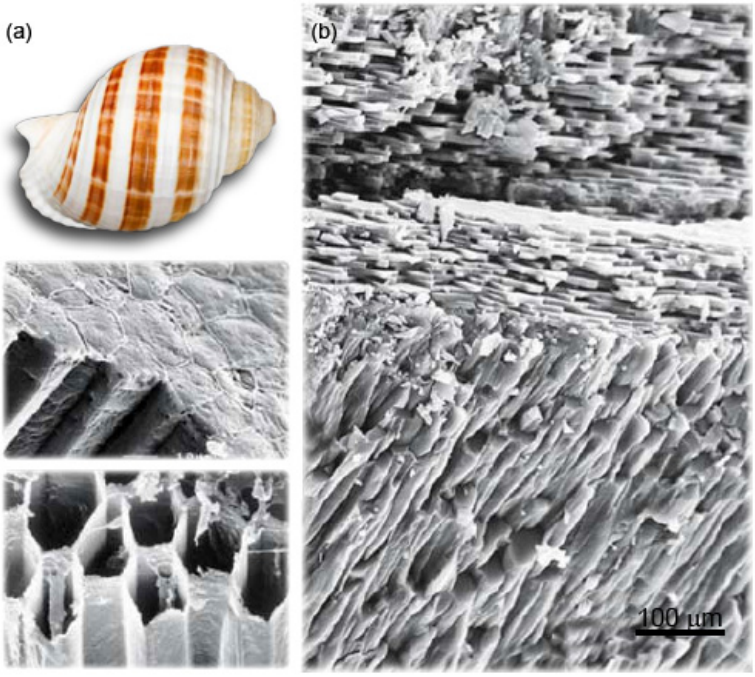

Figure 1-2. Natural ceramic material of a clam shell. a) photograph of the entire shell of the mollusk. b) scanning electron microscopy (SEM) of the interface between the nacreous (top) and prismatic (bottom) layer of the shell. At higher magnifications, one can see the prisms wrapped in an organic layer (upper micrograph) and the demineralized organic layer (lower micrograph) (Aizenberg, 2006).

Many groups of organisms use a different strategy and produce a composite structure of one single reinforced fiber. This tactic is used by organisms to build their skeletons with one large single crystal, such as echinoderms, calcareous sponges, foraminifera, among others (Aizenberg, 2006).

The basic concept of combining a rigid component with a flexible one still applies, but in this case the functions are reversed. In these peculiar composites, the host is a single crystal and the guests are the macromolecules that are there for the deliberate purpose of obstructing the single crystal in a specific crystal plane. This kind of composite has not yet been explored

for synthetic materials. In both cases, mineralized tissues are tailored to specific functions.

Douglas (2003) studied the structure in nature of apparently monocrystalline biominerals, such as the sea urchin's spine (Figure 1-3). He found a content of up to 0.05% in weight of organic macromolecules mixed with the inorganic part.

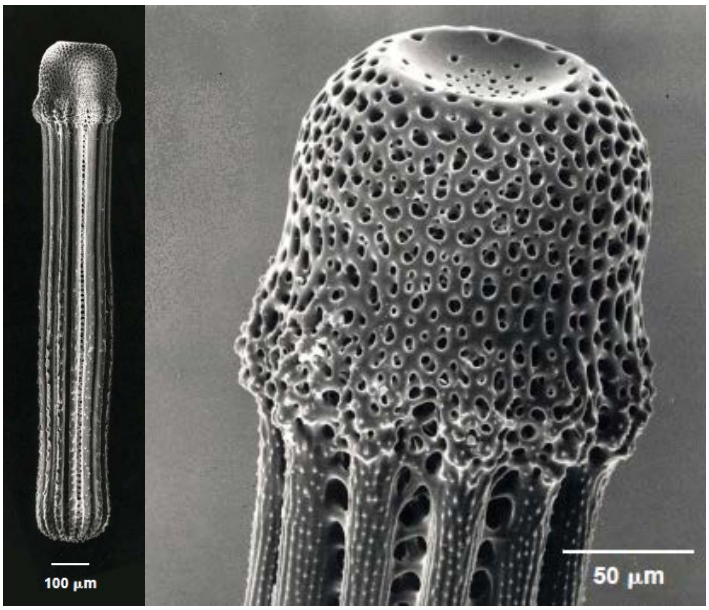

Figure 1-3. Micrographs of a porous single crystal of a spine of a sea urchin, which is composed of organic macromolecules and oriented $CaCO_3$ (calcite) (Douglas, 2003).

1.1.2 Biomorphic materials

The biomorphic mineralization is a multi-disciplinary subject related to materials science, biology, nanotechnology, physics, and other scientific disciplines. This technique applies biostructures as templates for the mineralization to produced materials with morphologies and structures that mimic those

found in living beings. The product, called biomorphic materials, combine the natural geometry with the chemical synthesis of materials.

Compared with conventional material production methods, biomorphic mineralization is easy, environmentally friendly and economical. Usually, biomorphic mineralization has few requirements for equipment and can be conducted in relatively mild conditions. Most biotemplates can be obtained in large quantities and at low costs by making effective use of natural materials and by converting waste into useful materials. Figure 1-4 presents the focus of biomorphic mineralization and biomorphic materials (Fan et al., 2009a).

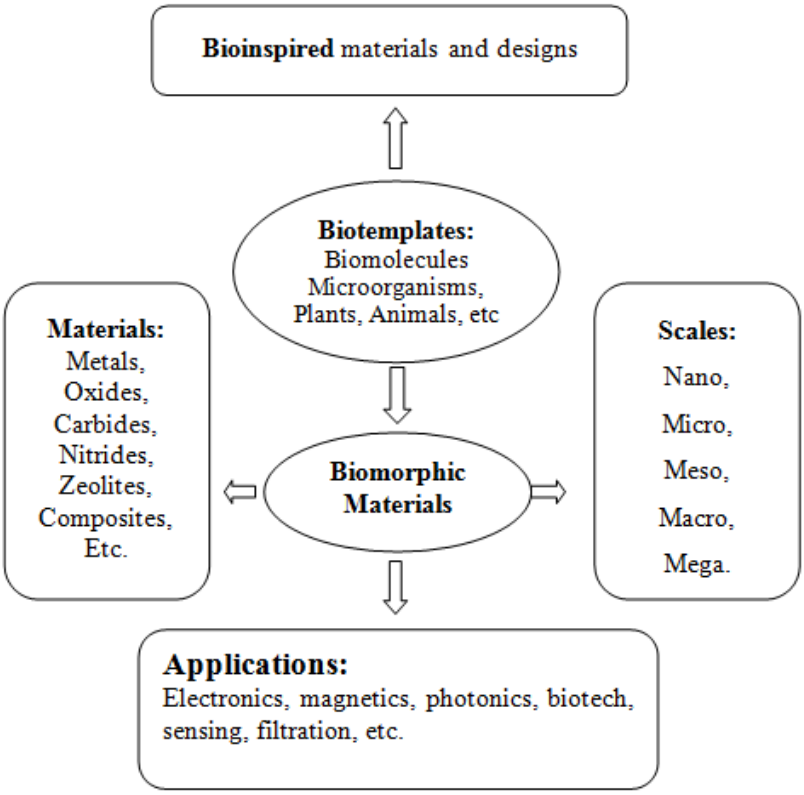

Figure 1-4. Focus of biomorphic mineralization and biomorphic materials (Fan et al., 2009b).

Biotemplates are applied in a multi-scale range that goes from the nano to the micro, macro and megametric scale. Nanodimensioned templates include biomolecules (DNA, proteins, peptides, lipids, etc.) and microorganisms (viruses, bacteria, fungi and yeasts). Their nanoscale dimensions make them templates to produce nanomaterials. The superstructure of these natural nanoparticles (i.e. arrangements of viral particles, bacterial particle arrays, arrays of biomolecules) may serve as a skeleton and direct the assembly of predetermined inorganic nanoparticles, forming inorganic architectures or nanocomposites with a high order of complexity.

The templates above the nanoscale include plant material (cellulose fibers, barks, leaves, roots, wood, marine sponges, pollen grains, beans, ESMs, mushrooms, etc.). Some of them have a hierarchical porous structure and can be converted into materials with multi-scale porosity. Some have photonic structures that can be converted into attractive functional materials, such as Au, Ag, TiO_2, ZnO, ZnS, which possess unique optical properties arising from the optical properties of the templates. Others have ultra-thin aspects that range in the nanoscale (on the surface and/or body) despite their macroscopic forms, which can result in the formation of delicate inorganic nanostructures (Fan et al., 2009b).

Biomorphic mineralization can be roughly divided into three types of processes: i) chemically converting biotemplates into biomorphic materials, ii) making a mold of the template using precursors, which are later converted into inorganic materials and iii) assembling preformed particles (usually in the nanometer range) in ordered structures, using natural molecules as building blocks, or natural superstructures and scaffolds as templates, using such processes as electrostatic interactions, metal-ligand interactions, and inter-biomolecular interactions. The materials that can be developed this way include metals, carbides, oxides, sulfides, nitrides and composites in general (Fan et al., 2009b).

1.1.3 Use of biotemplates to obtain nanomaterials

One way to obtain nanostructured materials is using biotemplates, since these have proteins that are capable of guiding the nanostruturaction of the inorganic material. Recently, two key advances have been made in this field. First, the number of successfully applied biotemplates has increased, including three-dimensional crystal structures. Second, the production of mutations located in the protein of the template, or the development of peptides that exhibit sequences for biorecognition inorganic structures. This has resulted in significant improvements in our ability to control the synthesis of materials mediated by the proteins of biotemplates (Lagziel-Simis et al., 2006).

A wide variety of biological structures with complex morphologies has been used as sophisticated templates for the preparation of porous materials in tailored structures. Typical examples of biotemplates include bacteria threads (Davis et al., 1997), plates of echinoderms skeletons (Meldrum and Seshadri, 2000), ESMs (Dong et al., 2007c)(Dong et al., 2007b)(Dong et al., 2006b); (Dong et al., 2007d)(Yang et al., 2003);(Liu et al., 2004); (Liu et al., 2005);(Dong et al., 2006a)(Yang et al., 2002); (Su et al., 2007)(Su et al., 2008a)(Su et al., 2008b), insect wings (Cook et al., 2003), pollen grains (Hall et al., 2003; Valtchev et al., 2003), leaves (Valtchev et al., 2003), wood (Shin et al., 2001), cellulose matrices such as filter paper (Shin et al., 2004), fabrics and cotton (Huang and Kunitake, 2003). In addition, crystalline networks with hierarchical structures with have been produced by carbothermic reduction of cellulose paper coated with titania (Shin et al., 2005).

Most porous structures that are produced using natural biotemplates, however, do not display a completely ordered structure. Many of them are made of irregularly shaped perforations and formed by interconnected fibers without any order. The only exceptions are bacteria threads (Davis et al., 1997) and echinoderms (sea urchin) (Meldrum and Seshadri, 2000). This happens because the original template (multicellular

filaments in the bacteria and the pores of the echinoderms plates) has a hexagonal arrangement. Subsequently, the porous structures derived from these two particular biotemplates also contain pores with a regular arrangement (Hoa et al., 2006).

1.1.4 Use of eggshell membranes as biotemplates

ESMs are a semipermeable material with high surface area and a structure composed of interwoven and interconnected fibers. These fibers are made of an organic material that contains functional groups of amine, amide and carboxylic types on its surface. In a sol-gel type process, these groups can interact with the precursor, anchoring the precursor molecules to the surface of the membrane fiber, where it can form a coating by gelling (Yang et al., 2002).

These characteristics have inspired scientists to use ESMs as a biotemplate in a sol-gel process to obtain fibrous structures, such as ESMs structures, composed of various oxides. Examples of materials synthesized using this process are ZrO_2 (Yang et al., 2003); $BaCrO_4$ (Liu et al., 2004); $CaWO_4$ (Liu et al., 2005); TiO_2 (Yang et al., 2002)(Dong et al., 2007d) (Dong et al., 2007a), SnO_2 (Dong et al., 2006a);(Dong et al., 2007b); ZnO (Dong et al., 2007c)(Su et al., 2007), Co_3O_4 and PdO (Dong et al., 2007b). Pd-PdO/TiO_2 nanocomposites have also been synthesized using ESMs (Su et al., 2008a). Another kind of nanocomposite that has already been synthesized is a hybrid nanocomposite consisting of ESM coated with nanoclusters of lead sulfide (Su et al., 2008b). In addition to these ceramic materials, ESM biotemplates have been used for the synthesis of polyaniline nanotubes (Gao et al., 2008).

In all studies, the removal of the membranes is the first step in the process. The isolation of these membranes can be done manually or with the aid of an acidic solution capable of removing the inorganic part of eggshells. After removal of the membranes, an experimental route usually follows a step where the membrane

is immersed in a solution containing the cations of interest. Here the gelation will occur and then a coating will form on the ESM fibers. After this step, the material is dried and calcined. The works using to ESMs as biotemplates for the synthesis of oxides have in common the success in mimicking the structures of the ESMs because of the self-assembly of the building blocks. The obtained materials are typically nanocrystalline, forming tubular structures with diameters of 200 to 400 nm with a micrometric porosity because of to the structure of intertwoven fibers and a nanometric porosity on the fiber walls.

1.1.5 Synthesis of ZnO and TiO_2 by biomimetization of eggshell membranes

To the best of our knowledge, besides the publication of the author of this thesis (Camaratta et al., 2015), there are currently three others publications on the synthesis of ZnO by mimicking ESMs. (Dong et al., 2007c)(Dong et al., 2007b)(Dong et al., 2008). In common to these publications, a 0.5 M solution of $Zn(NO_3)_2$ in ethanol was used. The influence of calcination temperature on the ZnO formed was the main focus of the studies. The immersion time of ESMs ranged between 13 and 15 hours and the structures of ESMs could be replicated with variations in their texture by varying some process variables, such as temperature or pH calcination.

The synthesis of TiO_2 using ESMs as biotemplates was described in four other publications (Dong et al., 2007a)(Dong et al., 2007d)(Su et al., 2008a)(Yang et al., 2002) besides the author of this thesis publication (Camaratta et al., 2013). The procedure has always involved the removal of the inorganic part ($CaCO_3$) of the ESMs, followed by the immersion of the membranes in the precursor solution. Typically, the literature describes ESMs as two membranes: the inner membrane (IM) and outer membrane (OM). The method of removing the membrane may influence the type of membrane that is obtained, IM or OM.

In the work of Yang et al. (2002) the outer membrane (OM) was isolated by removing the inner membrane in a three step process: i) manual removal of the IMs. ii) immersion of the remaining material (OM and inorganic material) in a solution of HCl to dissolve the inorganic part. iii) removal of the supernatants OMs using a forceps. With this procedure, the OMs are isolated. In other publications (Dong et al., 2007a)(Dong et al., 2007d)(Su et al., 2008a), the membranes used were removed manually, and probably should have been used only the IM.

In these works, the precursor solution is the solution that will provide the Ti ions and the conditions of synthesis. Yang et al. (2002) used a solution of 10% by volume of TBT (titanium tetra-n-butyl) in 2-propanol as the source of Ti. In the other studies (Dong et al., 2007a)(Dong et al., 2007d)(Su et al., 2008a), the precursor was $TiCl_4$ in an aqueous solution. In the article of Su et al. (2008a), the production of TiO_2 structures with Pd-PdO nanoclusters located inside the fibers was described. This was achieved by immersing the ESMs in a solution of $PdCl_2$ prior to the immersion in TiO_2. The immersion times used ranged from 4 to 13 hours. After soaking the membranes in the precursor solution, the hybrid ESMs are removed and dried. They are then calcined at temperatures preferably above 550°C, so that only the inorganic material remains after the heat treatment.

1.1.6 The eggshell and its membranes

The shells of poultry eggs are made of an organic matrix (3.5 wt%), which comprises the membrane and some constituents embedded in a layer of calcium carbonate (95%) in the form of calcite. The eggshell of a chicken egg is a natural porous bioceramics, which results from the sequential deposition of different layers within segments of the oviduct over a predetermined period. This is a perfectly ordered structure with a polycrystalline organization through the calcified shell, which has been described in many reviews (Wu et al., 1995)(Nys et al., 2004)(Gautron and Nys, 2007).

There are two membranes (called inner membrane -IM and outer membrane - OM) and they constitute the foundation of the shell (Wu et al., 1995) (Hunton, 2005). These membranes contain organic collagen types I, V, and X and glycosaminoglycans are stable in aqueous and alcoholic solutions, and undergo pyrolysis when heated (Dennis et al., 2000).

According to Nys and Gautron (2007), six layers can be observed, structurally speaking, from the inside to the outside that form a shell . The inner membrane is about 20 µm and is in direct contact with the albumen. The outer membrane has about 50 µm and is located between the inner membrane and the calcified shell. The mamilar layer or mamilar cones are about 70 µm thick and contain the assemblies with calcium reserves. This is where the inorganic $CaCO_3$ is adhered. Next, comes the palisade layer which consists of columnar grains of $CaCO_3$. This is the thickest layer of the eggshell, measuring about 200 µm in thickness. Finally comes the cuticle (~ 10 µm), a final outer layer of the shell, which contains most of the egg's pigments. In the inner part of the cuticle, we can also observe a layer of hydroxyapatite crystals.

ESMs are therefore a fibrous organic material mainly composed of proteins, which control the biochemical reactions that determine the growth of the physical structure of the inorganic portion of the eggshell. The structure of ESMs together with the porosity found in the inorganic part of the eggshell serves as an organ for gas exchange (Tullett, 1984). The Figure 1-5 shows the layers that form the eggshells.

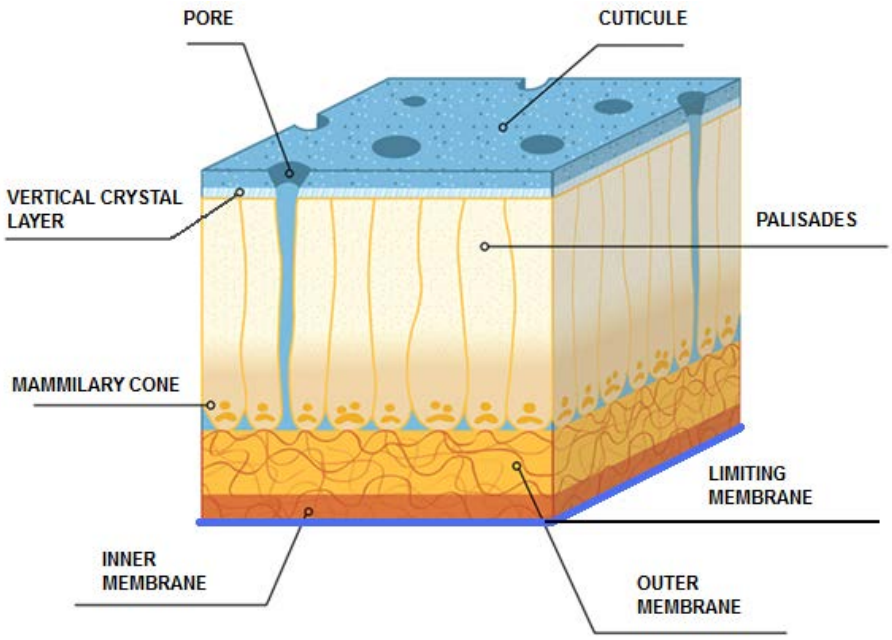

Figure 1-5 Schematic showing the structure of an eggshell (adapted from Hincke et al. (2012).

1.2 Zinc oxide (ZnO)

ZnO is a semiconductor material of the II-VI family. The difference in electronegativities between zinc and oxygen produces a high degree of ionicity in its bonds, making it into one of the more ionic compounds of this family. Well known as a n-type semiconductor, ZnO has a quite large direct bandgap (3.37 eV) and substantial excitation energy at room temperature (60 meV) (Arya et al., 2012). The crystal structures of ZnO are wurzite, zinc blende and rock salt (Figure 1.6) (Izyumskaya et al., 2007). However, at normal temperature and pressure conditions, ZnO will usually crystallize in a wurzite structure with a hexagonal lattice and two interconnected subnetworks of Zn^{2+} and O^{2-}, with the zinc ion surrounded by oxygen ions in a tetrahedral shape, and vice versa. This coordination yields a tetrahedral polar symmetry along the hexagonal shaft, which is responsible for many of the physical and chemical properties of

ZnO, including its piezoelectricity and spontaneous polarization. The structure is a key factor for ZnO crystal growth and the generation of defects. The variation in electrical properties, such as conductivity, is dictated by the presence of oxygen vacancies, zinc interstitial hydrogen impurities and other point defects like donors. In addition, the region near the surface of ZnO can be highly conductive because of the presence donors and the electron density (Arya et al., 2012).

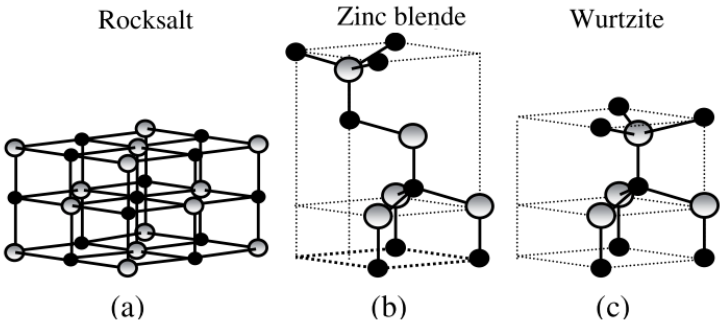

Figure 1-6 Representation of the different crystal structures of ZnO. (a) cubic rock salt. (b) cubic zinc blende. (c) hexagonal wurzite. Gray and black spheres represent atoms of Zn and O, respectively (Izyumskaya et al., 2007).

The wurzite structure (most common) belongs to the space group P63mc (C46v) and can be described as a combination of alternating planes of oxygen atoms and zinc atoms mounted along the c axis, with a displacement of 0.38 c between them, where c is the lattice parameter in the vertical direction. The network parameter values for this material under normal temperature and pressure range between 3.2475 Å and 3.2501 Å for a, and 5.2042 Å and 5.2075 Å for c (Izyumskaya et al., 2007).

From a technological point of view, ZnO is an important, multifunctional material with applications in transparent electronics, smart windows, piezoelectric devices, UV lasers, UV photodetectors, gas sensors, chemical sensors, biosensors and dye-sensitized solar cells (DSSCs). Additionally, the ferromagnetic properties of ZnO doped with rare earth metals show potential for spintronic mechanisms. Moreover, because of

the combination of its biocompatibility with its antibacterial properties, ZnO has been used in a variety of applications, such as drug-delivery treatment in cancer, medical products, sunscreens, skin lotions, etc. Its excellent electronic communication and chemical stability with a high isoelectric point (about 9) make the ZnO matrix attractive for applications in biosensors. In addition, the characteristics of ZnO can be modified by chemical functionalization of the surface (Arya et al., 2012).

1.2.1 ZnO synthesis methods

Until now, many methods have been used to produce ZnO. Chemical Vapor Deposition (CVD), thermal evaporation, sputtering, spray pyrolysis, and freeze-drying are some examples. However, strict conditions and complicated procedures drastically restrict large-scale applications in industry. The chemical routes, on the other hand, are showing themselves to be a promising option because of their simplicity, speed and cheaper resources. The main methods employed are hydrothermal synthesis, sol-gel and micro-emulsion growth. Meanwhile, the number of reports on various morphologies of ZnO, such as rods, wires, hollow microspheres, towers, bells, flowers and nuts, has been growing rapidly (Xie et al., 2011). It is well established that crystal formation in solution can be divided into two stages: crystal nucleation, which is followed by crystal growth from the nuclei. The nucleation and growth rates are therefore responsible for the formation of ZnO with different morphologies.

1.2.2 Preparation of ZnO nanoparticles by chemical routes

There are several publications on the synthesis of ZnO nanoparticles from solutions at room temperature. The synthesis of these particles is based mainly on alcoholic hydrolysis of zinc precursors, hydrothermal methods, and electrochemical routes.

Spanhel and Anderson (1991) explained the synthesis of ZnO nanocrystals using zinc acetate and ethanol as precursors with a distillation apparatus. They obtained a high concentration of colloidal crystals ranging from 3.5 to 5.5 nm in diameter. Hossain et al. (2005) modified this technique by employing the reflux method to achieve nanobelts of 700 μm in length. Many studies used an encapsulating agent, such as PVP (polyvinylpyridine), PEG (polyethylene glycol), etc., to prevent agglomeration of the particles and to obtain nanoparticles with sizes smaller than 5 nm (Rani et al., 2008).

The growth of ZnO using zinc acetate dihydrate as a precursor in the sol-gel process usually takes place in four stages: solvation, hydrolysis, polymerization and transformation into ZnO. The zinc acetate dihydrate is first solvated in methanol and then hydrolysed considered as the removal of acetate ions intercalated, resulting in a colloidal gel of zinc hydroxide (Eq. 1. 1).

$$Zn(CH_3COO)_2 \cdot 2H_2O + 2NaOH \rightarrow Zn(OH)_2 + 2CH_3COONa + 2H_2O \quad \text{(Eq. 1. 1)}$$

The size and activity of the solvent are obviously of influence on the reaction process and product. Methanol has a small size and its -OH and -OCH_3 groups are the most active. Methanol can react easily to form a precursor polymer with a high degree of polymerization, which is necessary to convert the sol in a gel. This zinc hydroxide is divided in the Zn^{2+} cation and the OH- anion according to the reactions (Eq. 1.2). This is followed by the polymerization of the hydroxylated compound to form Zn-O-Zn bridges. Only then does transformation into ZnO finally occur (Eq. 1.3) (Rani et al., 2008).

$$Zn(OH)_2 + 2H_2O \rightarrow Zn(OH)_4^{2+} + 2H^{2+} \quad \text{(Eq. 1. 2)}$$

$$Zn(OH)_4^{2+} \Leftrightarrow ZnO + H_2O + 2OH^- \quad \text{(Eq. 1. 3)}$$

When the concentration of OH^- is low, i.e. the pH is low, the growth of ZnO particles does not occur because no $Zn(OH)_2$ is formed in the solution. In the sol-gel method, however, there is a pH limit above which the nanostructure can be formed. In the study of Rani et al. (2008), the solution with pH < 7 had insufficient concentrations of OH^- groups to synthesize ZnO. Since pH controls the rate of ZnO formation, this affects the size and type of combinations necessary to get to a steady state. Because the newly formed nuclei are unstable in solution, there is a tendency to grow into large particles. The largest crystallite size was observed at pH 9. If the concentration of OH^- is further increased from this point, the crystallite size of ZnO is reduced. It is presumed that this occurs because of the dissolution of ZnO (the reverse reaction of Equation 1.3), when the ZnO reacts with the OH^-.

Perraud et al. (2012) investigated the production of ZnO by combustion methods. As previously described, this method involves an exothermic reaction between solids, liquids, liquid/solid or gas/solid. The process can be divided into two stages, the initiation of the reaction and then, depending on the experimental conditions, the wave propagation of the combustion throughout the compact. In a very short time, the reactants are completely converted into products. This method has many potential advantages. such as low processing cost, high efficiency and high production rates. Because of the high exothermicity, the direct synthesis of ZnO from Zn and O_2 does not allow a control of porosity of the final product because the reaction is much too explosive ($\Delta_f H$ ZnO = -348 $kJmol^{-1}$). Some studies describe the combustion synthesis of ZnO using glycine and zinc nitrate as reagents to obtain ZnO with a controlled morphology. Other studies report Zn and NH_4NO_3 as reagents.

Perraud et al. (2012), first synthesized compact ZnS monoliths from Zn and S ($\Delta_f H$ ZnS = -189 $kJmol^{-1}$), and then converted these into ZnO with thermal treatment in air. They observed that ZnS is transformed into ZnO with a heating in air between 577°C and 770°C, with an exothermic reaction peak at 738°C and 15% in mass loss.

Experimental results of absorbance showed a jump in absorbance in the blue region depending on the morphology and particle size of ZnO. This blue jump increases as the particle size of ZnO decreases. The absorption jump occurred with a blue shift of about 10 nm in the oval structure when compared with the flower-like structures.

1.2.3 Preparation of thin films of ZnO

Nanocrystalline ZnO film derived from sol-gel derived:

Just as is the case for TiO_2, sol-gel is a traditional method of synthesizing ZnO nanoparticles. In the case of ZnO, ethanol solutions and lithium hydroxide and zinc acetate precursors are usually used. The resulting sol contains nanoparticles with an average size exceeding 10 nm. For the formation of thin films, a subsequent process (commonly spin coating or dip coating) is carried out with the sol. During this process, the sol liquid is converted into a gel and, subsequently, dried and heated to obtain a porous structure in the form of a film.

The method known as doctor blade is also frequently adopted for the preparation of a nanocrystalline ZnO film. In this method, Triton X-100 (1% by volume) is conventionally added to the sol to facilitate film formation. The organic residues are then removed by a subsequent thermal treatment at temperatures that typically range from 300 to 400 °C (Zhang et al., 2009).

Deposition of films by Eletrostatic Spray:

The basic principle of ESD (Electrostatic Spray Deposition) is the generation of an aerosol using organic solvents containing inorganic or organometallic precursors under the influence of a high voltage. An aerosol is defined as a dispersion of solid particles or droplets in a gaseous environment. The liquid precursor is pumped through a metal needle in order to obtain a micrometric aerosol droplet size. Usually, a spherical drop is formed at the tip of the needle, but if a high voltage (typically 6-

15 kV) is applied between the needle and the grounded substrate, this drop at the needle tip takes on a conical shape and detaches itself to form a spray of highly charged droplets. The electrically charged droplets are attracted to the grounded substrate and heated as a result of the potential difference applied. Consequently, the droplets collide with the substrate, where they lose their charge. After complete evaporation of the solvent, a thin inorganic layer is left on the substrate (Zhang et al., 2009). The advantages of the ESD technique are:

i. A wide variety of morphologies of the films;

ii. The possibility of controlling the chemical composition of the coatings;

iii. The high deposition efficiency, since the electric field directs the droplets directly to the substrate.

Eletrochemical Deposition:

Electrochemical deposition is a simple and low cost route for the preparation of nanoporous films with a large surface area. The advantage of this method is that the growth orientation, morphology, and thickness of the film can be controlled by adjusting the deposition parameters (voltage, current density, temperature, etc.).

A typical electrochemical deposition process is described by (Xi et al., 2008). In this work, the authors used a system with two electrodes: a zinc plate as the anode, and glass coated with indium tin oxide (ITO) as the cathode. The electrolyte contained 0.04 M of zinc nitrate and 0.04 M of hexametilenteramine (HMT) in a solvent made up of a mixture of distilled water and ethanol 1:1. The HMT was used as a buffer, maintaining the pH at about 6. The ethanol acts as dampener agent to improve the thickness and uniformity of the surface coating. The deposition was conducted at 40°C in a water bath at a voltage of 0.5-0.7 V. They demonstrated that when a voltage of only 0.5 V was applied, the obtained films acquired a leave-type morphology, and that with

higher voltages polycrystalline particles were observed in the form of pellets of about 250 nm in diameter (20 - 30 nm in crystallite size). These particles are interconnected with pore sizes from 500 nm to 2 micrometers. Other voltages produce films with more irregular porous structures. The thickness of the deposited film is correlated with the voltage and deposition time. Typically, a thickness of 2.6 µm can be achieved with 0.5 V for 30 min. 2.4 µM with 0.7 V for 20 min. 0.7 µM with 3.4 V for 30 min. The temperature of the water bath also shows an influence on the film structure. An increase in temperature to 70°C results in a film with a less porous, compact structure.

In electrochemical deposition, the nucleation rate can significantly affect the structure of the film, especially in terms of porosity. The use of a surfactant to mediate nucleation can result in more porous ZnO. Porrolidona polyvinylchloride (PVP) has been described as an effective surfactant that produces ZnO with good photovoltaic efficiency when combined with electrochemical deposition. The films were shown to have a structure of interconnected crystalline grains.

The grain size, and therefore the surface morphology, of ZnO may be strongly influenced by the concentration of PVP. Increasing the concentration of PVP results in a reduction of the grain size. Typically, when the concentration is 4 g/L, the grain size was reduced to 20-40 nm. However, no ZnO film can be formed if the concentration is greater than 6 g/L. The DSSCs formed with films synthesized by this method have obtained an extremely high efficiency of 5.08% under illumination of 53 mW/cm^2, with the photoelectrode consisting of a nano-porous ZnO film of about 8 microns thick film over a 200 nm thick, compact nanocrystalline film.

Chemical Bath Deposition: Chemical Bath Deposition (CBD) has been developed to produce ceramic films from aqueous solutions at low temperatures through the pyrolysis of metal hydroxide layers. This technique has also been used for the manufacture of nanoporous films of ZnO. A typical CBD

manufacturing process goes through the following steps (Zhang et al., 2009):

i. The formation of the Layered Basic Zinc Acetate (LBZA), $Zn_5(OH)_8(CH_3COO)_2 \cdot 2H_2O$, through the hydrolysis of the dihydrate zinc acetate in methanol;

ii. The deposition of the LBZA film on the substrate at 60°C by heterogeneous nucleation;

iii. Heat treatment at temperatures above 150°C to transform the LBZA film in crystalline ZnO.

A similar method that has also been used to form a nanoporous ZnO film is depositing a layer of hydroxide zinc carbonate (LHZC) from a solution of zinc nitrate hexahydrate and urea in water (Hosono et al., 2005). Films synthesized through this method showed a nest-like morphology and a porous structure. Detailed studies have shown that films manufactured with CBD are composed of grains in sheet form with ZnO crystallites of about 11 nm, a pore size of about 12 nm, and surface areas of about 25 m^2/g (Zhang et al., 2009).

1.2.4 ZnO synthesis with the use of eggshell membranes as a biotemplate

Just as for TiO_2, the preparation of ZnO using ESMs as a biotemplate has been reported in a few previous studies. In the particular case of ZnO, all the studies found used zinc as source and zinc nitrate as the precursor of the synthesis. In his first publication on the synthesis of ZnO by biomimetization of ESMs, Dong et al. (2007c) immersed the ESMs in a solution of $Zn(NO_3)_2$ in ethanol for 13 hours. Afterwards, they were dried at room temperature for 10 hours and calcined at 400, 550 and 700°C for 1.5 hour. The characterizations by differential thermal analysis (DTA) and thermogravimetric analysis (TGA) revealed that the membranes begin to pyrolyze at 200°C and were completely burned at 550°C, while membranes impregnated with the

precursor solution had a constant residual mass of 17.9% (wt.) of inorganic material above 550°C.

(Dong et al., 2007c) concluded that the loss of weight between 200 and 350°C could be the result of the carbonization of organic ESM. Above 550°C, the products of the carbonization were burned. DTA curves showed two peaks at 357 and 531°C with an interval of about 100°C, which should represent the decomposition of $Zn(NO_3)_2$ and ESMs, respectively. Through XRD analysis, and based on the DTA and TGA analyses, the authors concluded that at 550°C all the diffraction peaks can be attributed to zincite (GD: P63mc, JCPDS 36-1451) and that the broadening of these peaks implies small sized nanocrystals.

Through scanning electron microscopy (SEM) analyses, the biomorphic microstructure of ZnO calcined at 550°C could be observed, which showed a structure of interwoven fibers similar to the ESMs. Further magnifications revealed that the diameter of the fibers was between 0.2 and 1.5 micrometers. The samples calcined at 400 to 700°C also showed the same structure, but as the crystallites grows with the increasing temperature, the surface of the ZnO fibers burned at higher temperatures appear to become coarser because of the large particle size. The SEM images show that the fibers consist of semi-enclosed ZnO channels, which are probably formed because of the nucleation of the nanocrystals along the membrane fibers in solution and the subsequent removal of the template. A fiber of about 200 nm in diameter analyzed with transmission electron microscopy (TEM), reveals the uniform porous structure consisting of nanocrystals. Through the TEM image the authors found that the sample fired at 550°C had nanocrystals of about 4.5 nm and micropores of about 1 nm between the nanocrystals.

In another publication on the synthesis of ZnO using ESMs as biotemplates, (Dong et al., 2008) prepared samples using the same, previously described methodology, and analyzed the thermal evolution, phase formation, morphology and distribution of pores in samples calcined at three temperatures (450, 550 and 700°C) and two pH values (2 and 5). In this work

they used a solution of 0.5M of $Zn(NO_3)_2$ in ethanol. The X-ray diffraction (XRD) showed that the hybrid membranes, which were impregnated with the solution of $Zn(NO_3)_2$ but were not calcined, remained amorphous and partially crystalline at a temperature of 450°C with zincite structure. Estimating the crystallite size by the width of the diffraction peaks, and based on the Scherrer formula, they obtained the values of 3.5 and 5.5 nm in crystallite diameter for the samples treated at 450 and 550°C, respectively. In this paper, the authors also emphasize that the structure of interwoven fibers of natural ESM was preserved and that the fibers of ZnO are between 0.2 and 1.5 mm in diameter. With the sample prepared at pH 5 and heat treated at 550°C, they obtained a similar morphology to those prepared at pH 2, but with few flakes embedded in the surface of the fibers. Figure 1-7 shows the morphology of the membranes obtained in pH 5 and pH 2.

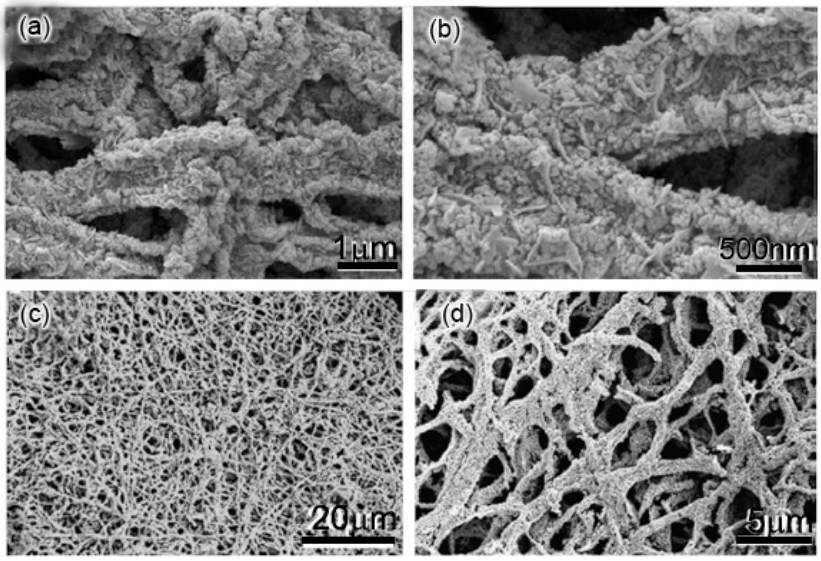

Figure 1-7. SEM images of ZnO calcined at 550°C. (a) view of the hierarchical structure of interwoven fibers obtained at pH 5. (b) higher magnification of image a. (c) Morphology of the structure obtained at pH 2. (d) higher magnification of image c.

The Fourier-transform infrared spectroscopy (FTIR) results from Dong et al. (2008) demonstrated the capture of Zn

ions through the membrane after immersion in the solution of this precursor, and the sample calcined at 450°C showed differences in the spectrogram when compared to the samples fired at 550°C and 700°C which have been assigned to the carbonization products membrane.

ESMs are not mineralized and consist of a matrix based on type I, V and X collagen, which is located in the center of each fiber covered with a layer of glycoprotein. In this regard, the macromolecular glycoprotein should act as soluble species to drive the reactions in the ESM fibers during the immersion in the solution, and preset the nucleation and growth of ZnO assembling the nanocrystallites in form of a hierarchical nanoarchitecture. This layer of the ESM fibers containing lysozyme is prone to dissociate in the impregnating solution is different from the collagenous core. Furthermore, lysozyme is an unstable protein unstable in weak acid pHs. The morphology of the material obtained is therefore inherently linked with the pH of the impregnating solution. This layer of lysozyme can exist at pH < 2.5, while the protein mantle may dissociate extensively at pH 5. So, lysozyme is partially activated at pH 2 and interacts with zinc ions. The inorganic precursors of Zn can cross-link and polymerize to form complexes that are mesoscopicaly ordered because of the self-assembling behavior of the hydrophilic groups of the glycoprotein.

Lysozyme is prone to dissociate in the precursor solution, in contrast to the collagenous core. The dissociation and disintegration of the coating of the fiber can lead to Peptidoglycan chains that interact with the initial zinc oxide nucleus. The face (0001) has lower surface energy and the peptide can control the crystal growth, which enables the accumulation of atoms on the face (0001). The formation of biomorphic hexagonal ZnO can be attributed to the surfactant function of the biomacromolecules of the ESMs. A special feature of this process is that inorganic structures are replicated in self-organizing assemblies, and the biotemplate provides both the chemical groups responsible for the reaction as the physical substrate (Dong et al., 2008). Figure 1-8

shows how interactions should occur between the fibers of the ESM and the precursor of Zn.

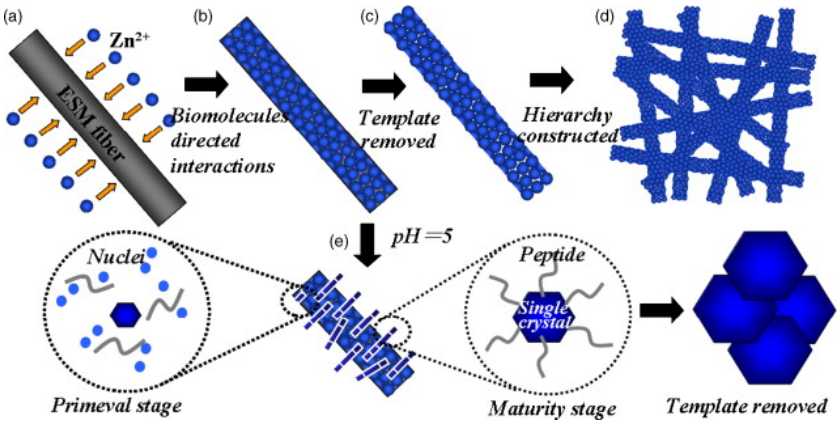

Figure 1-8. Schematic illustration of the process of imitation guiding the synthesis of hierarchical ZnO: (a) the interactions between the zinc ions and the ESM fiber (b) The assembly guided by ESM biomolecules in a pH = 2. (c) formation of the porous ZnO fibers after removal of the ESM, (d) construction of hierarchical structures, (e) the flakes encrusted in the fibers prepared at pH 5. Inserts (e) shows the initial stage, maturation stage, and the process after removal of the ESM, respectively, (Dong et al., 2008).

Dong et al. (2008) also listed the samples as type IV of the Brunauer classification after performing isotherms on the sample prepared at pH = 2 and heat treated at 550°C, which means they have a mesoporous structure. In addition, the pore size distribution was also calculated by desorption of the nitrogen isotherm using the Barrett-Joyner-Halenda method revealing an average porosity between 20 and 30 nm. The surface area, measured by Brunauer–Emmett–Teller (BET) theory, did not present significant variations for the different thermal treatment temperatures, being 9.86, 8.92 and 7.58 m^2/g for the samples fired at 450, 550 and 700°C, respectively.

1.3 Titanium Dioxide (TiO_2)

TiO_2 is an oxide with many engineering applications. Titanium dioxide is used, for example, in heterogeneous catalysis, in photovoltaic solar cells for the production of hydrogen and electricity, as gas sensor, as white pigment (for paints and cosmetic products), as protective coating against corrosion, as optical coating, in ceramics, and in electrical apparatus such as varistors (Diebold, 2003).

Titanium dioxide crystallizes in three main structures, rutile (tetragonal D_{4h}^{14} - $P4_2/mnm$, a = b = 4.584 Å, c = 2.953 Å) anatase (tetragonal, D_{4h}^{19} - $I4_1/amd$, a = b = 3.782 Å, c= 9.502 Å) and brookite, (rombohedral, D_{2h}^{15} - Pbca a = 5.436 Å, b = 9.166 Å, c = 5,135 Å). However, anatase and rutile dominate in TiO_2 applications. Their unit cells are shown in Figure 1-9. In both structures, the basic building block consists of a Ti ion surrounded by six oxygen ions in a slightly distorted octahedral configuration (Diebold, 2003).

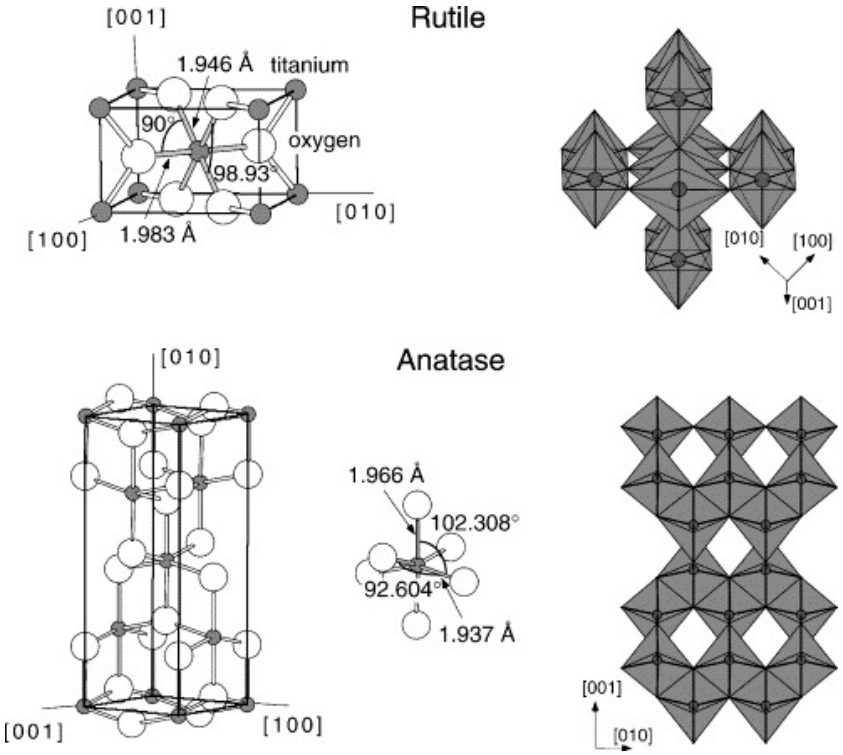

Figure 1-9. Rutile and anatase structures. The unit cell of tetragonal rutile has the dimensions of a = b = 4.584 Å, c = 2.953 Å, and anatase has a = b = 3.782 Å and c = 9.502 Å. In both structures, the slightly distorted octahedra are the basic unit of construction. The bond lengths and angles of the octahedrally ordered Ti atoms are indicated and the stacking of the octahedral structures is shown on the right (Diebold, 2003).

The photoactivity of TiO_2 is one of its most technologically attractive properties. The creation of an electron-hole pair by light irradiation, both in TiO_2 or in the adsorbed molecules, and the following chemical reactions or electron transfer are at the heart of devices based on TiO_2. Intense research has been initiated by Fujishima and Honda (1972) that water can be photocatalytically decomposed into hydrogen and oxygen. Because this discovery occurred at the height the oil price hikes in the 70s, it was immediately seen as a safe way to produce energy at low costs. However, the use of TiO_2 in the production

of hydrogen never reached the market, although there has been a recent revival in interest in this issue. The bandgap of TiO_2 is relatively large and its properties and absorption are not well matched with the spectrum of natural sunlight. The surface functionalization of TiO_2 by doping with molecules makes solar cells based on TiO_2 much more efficient in the conversion of solar energy into electrical energy (Diebold, 2003).

The photoelectric and photochemical properties of TiO_2 are still a focus of active research. The initial work of Fujishima and Honda (1972) on the photolysis of water with TiO_2 electrodes without external influence, and the idea that surface defect states may play a role in the decomposition of water into H_2 and O_2, have strongly stimulated recent work on TiO_2. Unfortunately, TiO_2 has a low quantum yield for the photochemical conversion of solar energy. The use of colloidal suspensions with the addition of dopant molecules have revealed an improvement in the efficiency of solar cells (Grätzel, 2001) and has increased the economic competitiveness of photoelectrochemical converters based on TiO_2 (Diebold, 2003).

1.3.1 TiO_2 synthesis by solution routes

TiO_2 can be prepared in the form of powder, fibers, thin films or crystals. Both powders and crystalline films can be built in sizes ranging from a few nanometers to several micrometers. It should be taken into consideration that the nanosized TiO_2 crystallites tend to agglomerate (Carp et al., 2004).

For some applications, processing in the liquid phase is one of the most convenient methods of synthesis. This method has the advantage that stoichiometry can be controlled, homogeneous materials can be produced, complex shapes are possible, and composite materials can be prepared. However, there are potential disadvantages, such as expensive precursors, long processing times and the presence of carbon as an impurity

(Carp et al., 2004). The most common routes to synthesize TiO_2 in solution are shown below:

Co-precipitation Method: This route involves the precipitation of hydroxides by adding a basic solution (NaOH, NH_4OH, urea) to the raw material, followed by calcination to crystallize the oxide. Typically, anatase is produced using sulfates or chlorides (Poznyak et al., 1998). In particular conditions, rutile can be obtained at ambient temperatures (Pedraza and Vazquez, 1999). The disadvantage is the lack of control of particle size and distribution, and the rapid (uncontrolled) precipitation often causes the agglomeration into larger particles instead of nanoparticles. $TiCl_3$ (Pedraza and Vazquez, 1999) or $TiCl_4$ (Poznyak et al., 1998) are most commonly used as raw material.

Solvotermic Method: This method applies chemical reactions in an aqueous (hydrothermal) or organic (solvothermal) (methanol (Yin et al., 2003), 1.4 butanol (Kang, 2003) and toluene (Kim et al., 2003) medium under self-produced pressures at low temperatures (typically below 250°C). Generally, but not always, a subsequent heat treatment is necessary to crystallize the material. The solvothermal treatment may be useful to control the grain size, particle morphology, the crystalline phase and the surface chemistry by adjusting the solution composition, reaction temperature, pressure, solvent properties, additives, and aging time.

Sol-gel Method: These methods are used for the synthesis of thin films, powders and membranes. Two routes are known: the route with alkoxides and without alkoxides. Depending on the synthesis approach, oxides can be obtained with different physical and chemical properties. The sol-gel method has many advantages over other manufacturing techniques, such as purity, homogeneity, flexibility in introducing dopants at high concentrations, stoichiometry control, easy processing, control over the composition and the ability to coat large and complex areas. The route without alkoxides uses inorganic salts (Bach et al., 1998); (Sivakumar et al., 2002) (such as nitrates, chlorides, acetates, carbonates, acetylacetonates, etc.). This route requires

the removal of additional inorganic anions. The alkoxide route (the most used), on the other hand, uses metal alkoxides as starting material ((Watson et al., 2003); (Haga et al., 1997)). This method involves forming a sol or gel of TiO_2 or its precipitation by hydrolysis and condensation reactions (with formation of a polymer) of titanium alkoxides.

More recently, sol-gel methods associated with the use of templates have been used to prepare phases of titania with large specific surface areas (Zhang and Reller, 2001); (Stone and Davis, 1998), which exhibit mesoporous structure. Ionic and neutral surfactants have been successfully used as templates to prepare mesoporous TiO_2 (Thieme and Schüth, 1999); (Cabrera et al., 2000); (Singhal et al., 1997)(Putnam et al., 1997)). Block copolymers can also be used as templates for the direct formation of mesoporous TiO_2 (Yang et al., 1998);(Li et al., 2003). In addition, many non-surfactant organic compounds have been used as pore formers, such as diolates (Thoms et al., 1998) and glycerin (Wang et al., 2004). Sol-gel methods associated with hydrothermal routes to obtain mesoporous structures (Wang et al., 2004) lead to a high surface area, even after heating at temperatures of up to 500°C. This can be explained as follows: usually mesopores collapse during calcination because of the crystallization of the wall. When hydrothermal treatment induces the crystallization of amorphous powders, the powders can effectively sustain tension during calcination, preventing the collapse of mesopores (Carp et al., 2004).

Microemulsion Methods: Water-in-oil microemulsion has been successfully used for the synthesis of nanoparticles. Microemulsion solutions can be defined as thermodynamically stable and optically isotopic solutions that are made of two immiscible liquids consisting of microdomains of one or both solutions, stabilized by an interfacial surfactant film. A surfactant molecule generally has a polar head (hydrophilic) and a long aliphatic chain (hydrophobic) on its tail. These molecules optimize their interactions at the interface between the two liquids. This significantly reduces surface tension. Despite promising initial studies, there are few publications on the

controlled synthesis of titania from these microemulsions ((Zhang and Gao, 2002); (Lim et al., 2004)). In particular, hydrolysis of titanium alkoxide microemulsions based on the sol-gel method has led to uncontrolled flocculation and aggregation (Pillai et al., 1995), except at very low concentrations (Chhabra et al., 1996). However, an improved method using carbon dioxide in place of oil has been used to produce nano-TiO_2 (Hong et al., 2003).

Combustion Synthesis: Combustion synthesis (hyperbolic reaction) leads to highly crystalline, thin particles with large surface areas ((Nagaveni et al., 2004b)(Nagaveni et al., 2004a)). The process involves a rapid heating of a solution containing compounds, mixtures or redox groups. During combustion, the temperature reaches about 650°C for a short period of time (1-2 min.), crystallizing the material. Because of the short time, the growth of TiO_2 particles and the transition to the rutile phase are avoided (Carp et al., 2004).

Eletrochemical Synthesis: Electrochemical synthesis can be used to prepare advanced thin films. By varying parameters, such as electrolysis potential, current density, temperature, and pH, one can easily control the characteristics of the films. The electrodeposition of TiO_2 films with several Ti compounds, such as $TiCl_3$ ((Kavan et al., 1993); (Zhang et al., 2001), $TiO(SO_4)$ (Karuppuchamy et al., 2013), and $(NH_4)_2TiO(C_2O_4)_2$ (Ishikawa and Matsumoto, 2001), have therefore been performed. The use of inorganic titanium salts in aqueous solutions is always difficult because of the high propensity of the salts hydrolyzing. Consequently, electrolysis requires an acidic environment and an environment free of oxygen (Zhitomirsky, 1998). Non-aqueous solutions are ideal to overcome this problem (Kamada et al., 2002).

1.3.2 Synthesis of macroporous TiO_2 networks

Many studies have been performed to synthesize materials with hierarchically ordered, macroporous structures with bimodal

porosity. These materials combine the wide availability of diffusion paths, because of the macroporous network structure, with a large surface area, selectivity, catalytic properties or ion exchange systems smaller porosities ((Davis et al., 1997); (Zhang et al., 2000)(Zhang et al., 2002); (Antonietti et al., 1998);(Lee et al., 2001)).

The synthesis of macroporous networks of TiO_2 and hollow fibers has attracted increasing interest ((Breulmann et al., 2000);(Caruso et al., 1998);(Caruso et al., 2001)(Liu et al., 2002). Coatings obtained by sol-gel (Caruso and Antonietti, 2001) have proven to be a simple and versatile method to obtain TiO_2 with these structures. For example, TiO_2 with a macroporous, "Coral type" network structure were manufactured through the sol-gel coating of a polymeric gel ((Caruso et al., 1998); (Caruso et al., 2001)), cellulose acetate membranes (Caruso and Schattka, 2000). In addition, TiO_2 pipes were produced by the sol-gel coating of polymer fibers obtained with eletrospinning (Caruso et al., 2001).

Also have been used for producing these macroporous structures consisted of bimodal porosity, synthetic templates as latex particles (Antonietti et al., 1998)(Antonietti et al., 1998) and polyurethane foam (Lee et al., 2001), some biological matrices, including bacterial threads ((Davis et al., 1997); (Zhang et al., 2000)), cellular structures from wood (Shin et al., 2001) and starch gels (Zhang et al., 2002).

1.3.3 Biomimetic synthesis of TiO_2

Because of the great potential for improving its properties, the synthesis of titanium dioxide using biotemplates is of particular technological interest. To the best of our knowledge, few studies have been conducted on the synthesis of TiO_2 using biotemplates, in particular on ESMs. These publications have in common that they emphasize the possibility of developing promising properties in various areas, such as photocatalysis and

photovoltaics. This is a consequence of the small crystallite size, the ability to obtain anatase and/or rutile phase and special morphologies.

To mimic the biomaterial, the sol-gel process is used. In this route, the ingredients of the sol should undergo gelation preferably on the biomaterial's surface, interacting with bioelements as proteins, polysaccharides and functional biowaste. Therefore, the synthesis guided by a biotemplate in a colloidal system has proven to be an ideal approach for the design and construction of advanced materials with advanced physical and chemical properties (Dong et al., 2007d).

1.3.4 Synthesis of TiO_2 using ESM as biotemplates

The first publication (Yang et al., 2002) studying the use of ESMs as a biotemplate investigated the synthesis of nanosized TiO_2 and reported the formation of TiO_2 with a macroporous network composed of intertwined and coalesced fibers with diameters between 0.3 and 1.5 µm. This structure was characterized by thermogravimetric analysis, X-ray diffraction, BET analysis and scanning electron and transmission microscopy. Using titanium tetra-n-butyl (TBT) as source of titanium in a neutral and in an acidic solution, hierarchical structures of TiO_2 were obtained with a tubular wall thickness smaller than 200 nm. Based on the TGA result, the firing temperature was established at 500°C, producing an anatase phase with a crystallite size of 5 to 10 nm. The main difference between the membranes obtained under different conditions involved their macroporosity. The membrane obtained in acidic solution had larger macropores than the membrane obtained in the neutral solution (4 µm for the acid mediun and 1.5 µm for the neutral medium). According to Yang et al. (2002), complexation of acetyl acetone with TBT occurred in acid hydrolysis. This results in slower hydrolysis and hence a more homogeneous deposition of TiO_2, producing a coating with less TiO_2 shrinkage after firing. The surface area measurement was 62 m^2/g and the

average pore size measured by BET was 8.2 nm, indicating the presence of mesopores in the walls of the tubes.

In the work of Dong et al. (2007a), membranes consisting of a TiO_2 nanoparticle network containing micropores and mesopores were successfully synthesized. For this, they used ESM as biotemplates. The synthesis conditions controlled were the concentration of the aqueous solution of $TiCl_4$ and the pH. The membranes used were manually separated from $CaCO_3$, rinsed in distilled water and dried naturally. These membranes were then dipped in the solution of $TiCl_4$ for 13 hours and then washed in distilled water and dried naturally. A heat treatment was performed to remove the biotemplate at 550°C for 1.5 hour. The authors found that the form of the phases depends on the pH of the synthesis. A pH around 1 produces the rutile phase and a pH of 4 or greater favors the formation of the anatase phase. Similarly, the concentration of the solution also influences the phases formed, with lower concentrations showing a greater tendency for the formation of anatase. The average crystallite size calculated by the Scherer's formula was 5.8 nm. The influence of pH was also observed in the morphology of the material obtained, since a clump structure and distorted fibers were obtained with higher pHs. Higher concentrations were also observed to form larger particles, while smaller nanocrystals are obtained with lower concentrations. An average crystallite size of 6 nm was confirmed with transmission electron microscopy. The diffraction patterns revealed the polycrystallinity of the TiO_2. The isotherms of membranes obtained from all pH were of type IV with type H3 hysteresis loop in the classification Brunauer, indicating a mesoporous system composed of interconnected pores and very high conductivity of pores according to the percolation theory. In addition, the authors evaluated the photocatalytic activity, which proved to be higher than P25, but not as high as expected (Dong et al., 2007a).

In another article, Dong et al. (2007d) described the effect of pH, temperature and heating rate of the calcination process in the production of TiO_2 membranes obtained from an aqueous $TiCl_4$ solution. In this work, the authors found that, prior to

calcination, the membranes are completely amorphous and that the anatase crystallization begins at 400°C and the rutile formation at 800°C. The morphology of the material was changed with increasing temperature, and mimetization was considered to occur until 700°C, since above 800°C laminated sieves started to appear. The authors concluded in this study that the titania membranes have pores that range from the nanoscale to the macroscale (2 nm to 8 microns). The isotherms revealed type IV with H3 hysteresis loop, indicating a mesoporous system with high pore connectivity. They also found that an increase in the calcination temperature results in less pores, but with larger dimensions. The pore size distribution is mainly affected by the calcination temperature and not by the heating rate.

1.4 The functioning of the DSSC

A major breakthrough in the production of dye-sensitized solar cells was achieved in 1991 when Grätzel and O'Regan published their study on the use of a mesoporous semiconductor electrode. The use of mesoporous electrodes has led to a paradigm shift in this area. Until then, it was believed that only semiconductors with a smooth surface could be used. The following is a typical configuration: The most important part of the device is the mesoporous oxide layer composed of an interconnected network of nanoparticles that were sintered together to create electronic conduction. Typically, the thickness of this layer is around 10 μm and the size of the nanoparticles is between 10 and 30 nm in diameter. The porosity is 50 to 60% (Hagfeldt et al., 2010). This mesoporous layer is deposited on the transparent oxide conductor called TCO (Transparent Conducting Oxide), which in turn is deposited on a glass or plastic substrate. The most commonly used substrate is glass coated with tin oxide doped with fluorine (FTO - Fluorine-doped Tin Oxide). A monolayer of the sensitizer is absorbed by the nanocrystalline oxide layer. The photoexcitation of the sensitizer results in the injection of an electron into the conduction band of the oxide, leaving the sensitizer in an oxidized state. The sensitizer is

restored to its initial state by an electron transfer from the electrolyte, usually an organic solvent containing an iodide/triiodide redox system. I^{3-} ions formed by oxidation of I^- diffuse a short distance (< 50 micron) through the electrolyte to the cathode, which is typically coated with a thin layer of platinum that serves as a catalyst. The regenerative cycle is completed by the reduction of I^{3-} to I^- (Hagfeldt et al., 2010). A schematic of the reactions that occur in a DSSC and the morphology of the oxide layer are presented in the Figure 1.10.

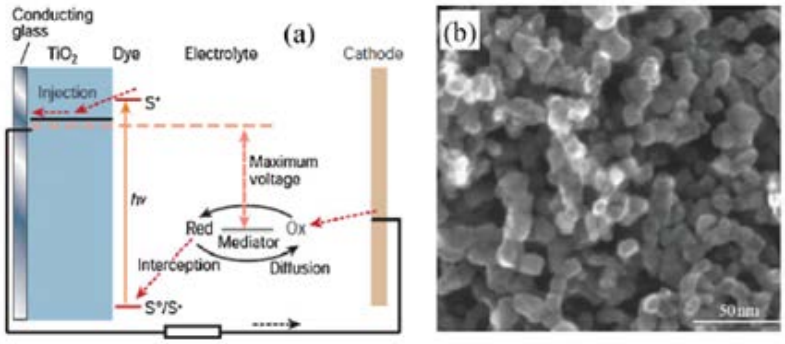

Figure 1-10: DSSC based electrochemical system. (a) Schematic of the construction and operating principle of the device. (b) SEM image of an electrode of nanocrystalline TiO_2 (~ 20 nm diameter) (Adapted from (Zhang et al., 2009).

1.4.1 Improvements in DSSC

All basic components of the DSSC have been worked upon by different researchers, and a number of improvements have been suggested. The improvements have been made mostly in order to obtain higher conversion efficiency, however, improvements in its components aiming lower cost of manufacturing are also fundamental to the implementation of this type of component on an industrial scale.

To Karthikeyan et al. (2006), the following requirements are the main characteristics of TiO_2 films for its efficient

functioning in solid-state dye sensitized solar cells: (i) pure anatase phase (ii) optimum porosity leading to high surface area for better dye absorption and hole conductor (iii) nanoparticle network for better electronic percolation. Besides the standard requirements, the films should also have optimum pore volume and pore diameter in the nanorange (10–50 nm). It can be deduced that for other semiconductors the optimum porosity and nanoparticle network characteristics is also necessary.

Using a blocking layer:

To prevent recombination in the FTO substrate/electrolyte interface, it can be used a blocking compact layer. This thin compact layer (~100nm) can be prepared by chemical bath deposition, spray pyrolysis, sputtering (Hagfeldt et al., 2010) or dip-coating technique (Gong et al., 2017). The idea of using a compact layer to enhance the conductive contact between semiconductor and FTO substrate is also applicable for ZnO-based dye-sensitized solar cells (DSSCs). Guan et al. (2012) introduced a ZnO compact layer prepared by a sol-gel method into photo electrode at the interface between fluorine-doped tin oxide (FTO) substrate and a mesoporous ZnO layer. It was found that the interfacial resistance of the ZnO (0.1 M)/FTO cell sample was considerably lower (6.77 Ω) compared to that of bare FTO substrate (11.57 Ω). In Figure 1-11 is shown how the compact a scheme of a ZnO DSSC assembled with a blocking ZnO layer made by sol gel (a) and a ZnO DSSC made without the ZnO blocking layer.

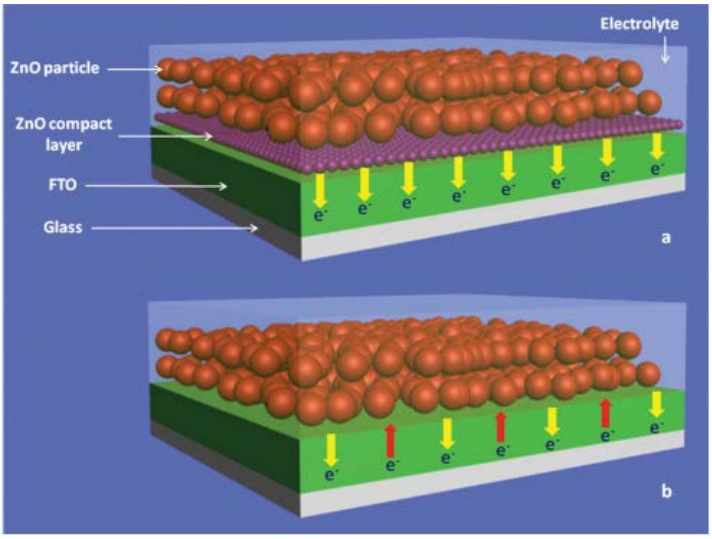

Figure 1-11: Schematic diagram of ZnO nanocrystalline photoelectrode with (a) and without (b) compact layer (Guan et al., 2012).

Metal oxide overlayers

At the TiO_2 photoanode/electrolyte interface, a conformal coating of insulating layers (such as SiO_2, Al_2O_3, and ZrO_2) on the TiO_2 films are shown to retard interfacial recombination dynamics (Palomares et al., 2003). It is important to have conduction band edge of these metal oxides more negative compared to both the TiO_2 conduction band edge and dye excited state oxidation potential (ESOP). Therefore, the metal oxide overlayers could function as physical barrier layers for both electron injection and charge electron recombination reactions ((Gong et al., 2017). In Figure 1-12 it is shown an example of an overlayer of Al_2O_3 coating TiO_2 particles and consequently slowing down the recombination process at the photoanode/electrolyte interface.

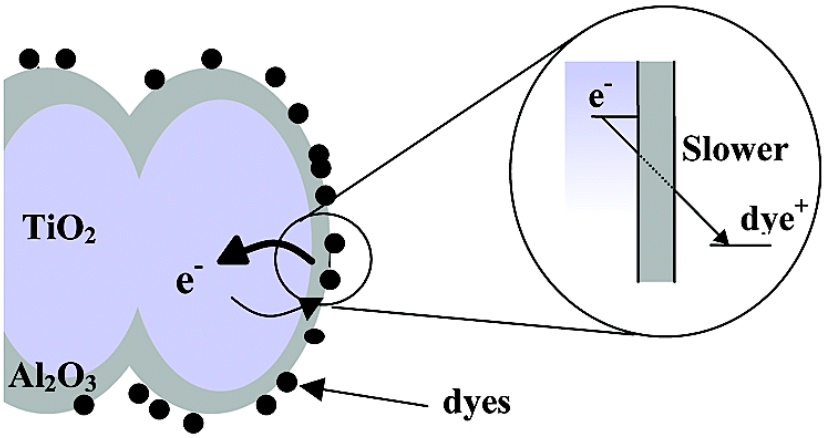

Figure 1-12: Schematic of TiO_2 particles coated with Al_2O_3 overlayer and dyes molecules (Palomares et al., 2003).

Light scattering

Light scattering is another way to improve the solar cell conversion efficiency. One way to enhance the light scattering is to incorporate larger particles as effective light scatters (Gong et al., 2017). The light scattering particles also can be coated on the top of active layer. Combining multi-layer architecture with hierarchically structured TiO_2 Chang et al. (2013) demonstrated a simple strategy for broadband light confinement without sacrificing dye-loading capacity. In *Figure 1-13* it is presented present a hierarchically structured multi-layer which demonstrate remarkable improvement in the overall efficiency compared with nanocrystalline single layer DSSC.

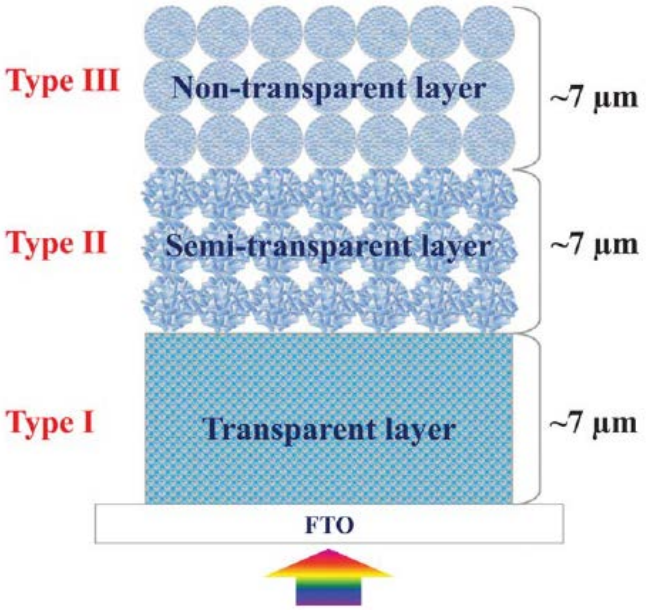

Figure 1-13: A hierarchically structured multi-layer TiO_2 architecture (Chang et al., 2013)

Light harvesting

For effective light harvesting, the dye-sensitizer plays a key role absorbing all incident light from the visible to the near-infrared region of solar spectrum up to the wavelength of approximately 920 nm. The best photovoltaic properties is presented by the dyes made with ruthenium (Ru) complexes due its broad absorption spectrum, suitable excited and ground state energy levels, relatively long excited-state lifetime, and good (electro)chemical stability (Hagfeldt et al., 2010). However, there are several draw-backs of them: the high cost and the limited amount of noble metals, and the sophisticated synthesis and purification steps. In general, metal free organic dyes are promising candidates to substitute the Ru complexes (Gong et al., 2017). Co-sensitization, combining two spectrum complementary dyes (i.e., blue and red absorbing sensitizers) into a DSSC, offers

a cost- effective route to the panchromatic sensitization.(Gong et al., 2017). In the *Figure 1-14* it can be seen the effect of different Ru dyes compared to blank TiO_2 in respect to the Incident Photon to Current Conversion (IPCC). The dyes are responsible for the absorption in visible region in the electromagnetic spectra.

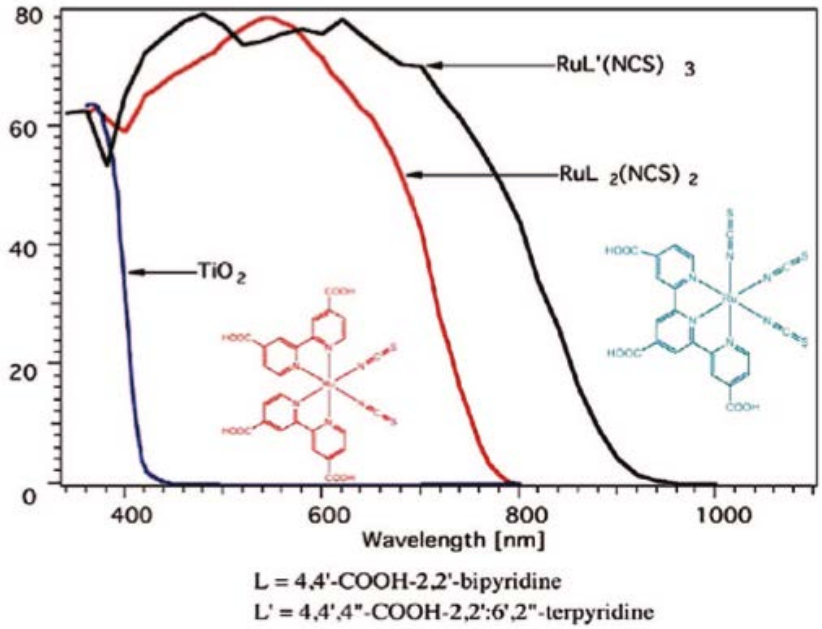

Figure 1-14: Incident photon to current conversion efficiency as a function of the wavelength for the standard ruthenium sensitizers N3 (red line), the black dye N749 (black curve), and the blank nanocrystalline TiO_2 film (blue curve). The chemical structures of the sensitizers are shown as insets(Hagfeldt et al., 2010).

Another way for light harvesting is the new class of solar cells called quantum-dot sensitized solar cells (QDSSCs). It has a similar device structure with traditional dye-sensitized solar cells except that replacing organic molecular dyes with inorganic semi-conductor quantum dots (QDs) (Wang et al., 2017). For high efficiencies, it is necessary to cover large areas of the semiconductor with small size quantum-dots. Semiconductors

such as CdS, PbS, Bi_2S_3, CdSe and InP, wich absorb light in visible can serve as sensitizers as they are able to transfer electrons to large band gap semiconductors such as TiO_2 or SnO_2 (Robel et al., 2006). The Figure 1-15 shows a scheme of an TiO_2/CdSe quantum-dot sensitized solar cell (Robel et al., 2006).

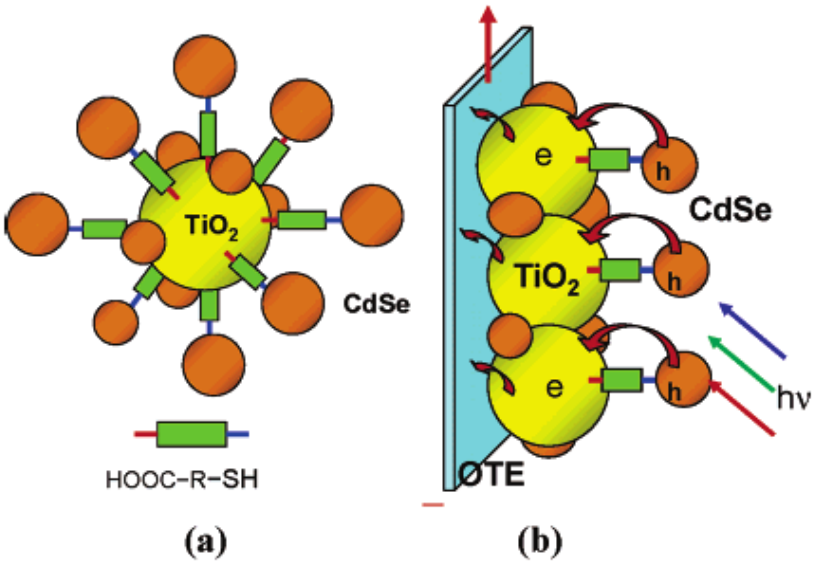

Figure 1-15: (a) Linking CdSe Quantum Dots to TiO_2 Particle with Bifunctional Surface Modifier; (b) Light Harvesting Assembly Composed of TiO_2 Film Functionalized with CdSe QDs on Optically Transparent Electrode (Not to Scale)(Robel et al., 2006).

1.4.2 The use of ZnO and TiO_2 as electrodes in DSSC

High performance in DSSC can be achieve by high electron injection from the dye and rapid electron transport. From the point of view of the photoanode, the electron-hole recombination rate should be low in order to achieve higher conversion efficiency. This can be achieve when electron transport rate is high (Sugathan et al., 2015). Electron Transport in Mesoporous Semiconductor Electrodes is dictate by electron diffusion, however for some reasons the electron diffusion is

diminished. The possible origin for this relatively slow diffusion are: i.) Traps located at the TiO_2/electrolyte interface; ii) Traps in the bulk of the TiO_2 particles; iii) Grain Boundaries; iv) electrostatic interactions between electrons and ions in the electrolyte causing ambipolar diffusion (Hagfeldt et al., 2010). The density of trap states will scale differently with nanoparticle size depending on their location. Zhu et al. (2006) affirms that transport-limiting traps are located predominately on the surfaces of the particles, thus decreasing the superficial area of the particles leads to a decrease in trap state density and an increase in electron diffusion coefficient. Galoppini et al. (2006), studying the electron transport in dye-sensitized solar cells found that electron transport in solar cells with ZnO nano-rods (without grain boundaries) was about 2 orders of magnitude faster (~30 μs) than the transport in cells with colloidal ZnO or TiO_2 films, thus the morphology plays a key role for electron transport properties. Also, they found no light dependence in the DSSCs prepared using single crystalline ZnO nano-rods.

Recently, various structures such as nano-rods, nano-tubes, nano-wires, nano-cones, nano-leaves or their mixture have been fabricated on transparent conductive glass for the semiconductor electrode (Sugathan et al., 2015). For many years, TiO_2 nano-structured materials and the ruthenium- bipyridyl dye families such as N719, N3 and C101 are the most efficient materials for the photoanode and have subjugated the highly efficient solar cells (Sugathan et al., 2015)

The TiO_2 nano-particles based photoanode is most commonly used in DSSC, but it has some limitations due to the presence of large number of grain boundaries, that lead to electron recombination losses. It also fails to achieve good efficiency in near infrared region (Sugathan et al., 2015).

Many semiconductor have been used, but the ZnO nano-particles having band gab similar to that of TiO_2 has been extensively used by researchers (Sugathan et al., 2015).

Just as TiO_2, ZnO is a semiconductor with a large bandgap and similar structure and physical properties (Table 1-1).

However, ZnO has a higher electron mobility, which favors electron transport and can reduce the recombination loss in DSSCs. Many studies have been performed with ZnO as a substitute for TiO_2 in DSSCs, but the efficiencies obtained, between 0.4 and 5.8%, are well below the 11% obtained with TiO_2. Even so, ZnO is still considered a prominent alternative to replace TiO_2 because of its easy crystallization and anisotropic growth. These properties enable ZnO to be produced in nanostructures that present various unique properties for electronic, optical or photocatalytic applications (Zhang et al., 2009).

Table 1-1: Comparison of physical properties of ZnO and TiO2 (Zhang et al., 2009)

	ZnO	**TiO_2**
Crystalline structure	Rock Salt, Zinc Blend and Wurzite	Rutile, Anatase and Brokite
***Bandgap* (eV)**	3.2 – 3.3	3.0 – 3.2
Electron Mobility (cm^2Vs^{-1})	205 - 300 (ZnO bulk) 1000 (ZnO nanowire)	0.1 – 4
Refractive index	2.0	2.5
Effective electron mass (m_e)	0.26	9
Relative dielectric constant	8.5	170
Electron diffusion coefficient (cm^2s^{-1})	5.2 (ZnO bulk) 1.7×10^{-4} (nanoparticulated film)	0.5 (TiO_2 bulk) $\sim 10^{-8}$ a 10^{-4} (nanoparticulated film)

1.4.3 Solar cell measurement parameters

For an analysis of the functioning of cells, we must use well defined environmental parameters (mainly in the comparison of cells and solar panels). One of the standards used in photovoltaic is the standard test conditions (STC), where the values for each magnitude are: irradiance equal to 1000 W/m^2 (also called "a sun", or full sun - SP), AM 1.5 and temperature of 25 degrees (Carvalho, 2014).

The I-V curve of a solar cell appears in the fourth quadrant (negative current and positive voltage - energy generator). For presentation purposes, this curve is always inverted, considering the current as positive (as observed in the example of Figure 1-16).

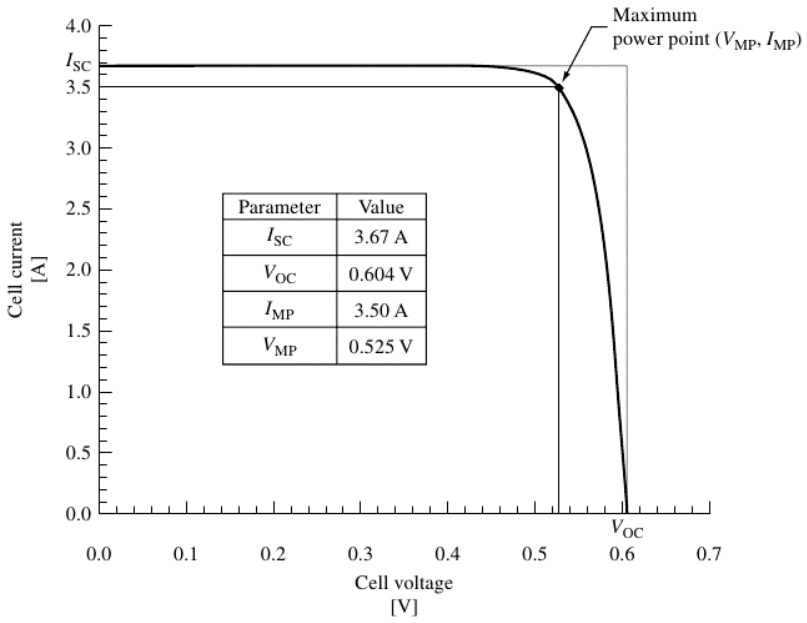

Figure 1-16: Current–voltage characteristic of the silicon solar cell (Luque and Hegedus, 2011)

With the I-V curve of a cell or panel, we can obtain several important quantities as:

Short-circuit current (I_{SC}): current displayed when the cell terminals are closed (i.e. a zero resistance) - is the point of intersection between the curve and the axis of the currents. The short-circuit current comes from another parameter, the short-circuit current density (relate through the area A of the cell):

$$I_{SC} = A \cdot J_{SC}$$

The values of J_{SC} vary according to the material and technology employed being usually about a few tens of mA/cm^2.

Open Circuit Voltage (V_{OC}): is the voltage displayed when the cell terminals are open (assuming an infinitely high resistive load connected at their terminals) - is the point of intersection between the curve and the axis of the voltages. As in the case of the I_{SC} current, the value of V_{OC} also depends on the material and the manufacturing technique used. The typical values described by Green et al. (2017) range from 0.5134 V for CZTSS ($Cu_2ZnSnS_{4-y}Se_y$) cells to 280.1 V for the tandem cell a-Si/nc-Si. The value for a DSSC from Sharp is 0.744 V.

Maximum power point (M_{PP} or P_{MAX}): is the point of the curve where the product between the voltage and the current is maximum; this operating point displays the maximum power that the cell can provide; At this point, the voltage and current values are called voltage (V_{MP}) and maximum power current (I_{MP}).

Fill factor:. The rectangle-defined V_{OC} and I provides a convenient means for characterizing the maximum power point. The fill factor, FF, is a measure of the squareness of the I –V characteristic and is always less than one. It is the ratio of the areas of the two rectangles shown in Figure 1-16 or:

$$FF = \frac{P_{max}}{V_{OC} I_{SC}} = \frac{V_{MP} I_{MP}}{V_{OC} I_{SC}}$$

High-quality cells have a factor greater than 0.7 (Grade A), while second-line cells (grade B) have a factor between 0.4

and 0.7. It is a quantity that also depends on the material and the technique of manufacture: c-Si, between 0.80 and 0.82; CdTe, 0.77; α-Si, 0.68, DSSC 0.71; c-GaAs, 0.8; InGaP / GaAs / InGaAs, 0.86 (Carvalho, 2014).

Efficiency of conversion or yield: We can also calculate the yield η of a cell, which is the relation between the power that reaches the cell (through the photons that affect the surface of the cell) and the power generated by it. Equating, we have:

$$\eta = \frac{P_{máx}}{I_{rr} A}$$

where I_{rr} is the irradiance, and A is the cell area. The power unit used in photovoltaics is Watt of peak power or W_P, which is associated with the standard test condition or STC.

Serie Resistance R_S: originated from the resistances of the semiconductor material itself, between the limits of the depletion region and the metal contacts. In the ideal case, its value is zero; the increase in the value of this resistance decreases the V_{OC} value (because there is a voltage drop in this resistance) and the fill factor, until a limit condition where the I-V curve is reduced to a line with a slope $1/R_S$. The magnitude of this magnitude is not commonly reported by manufacturers but is usually around thousandths to tens of Ω. Figure 1-17 shows the influence of the R_s on the I-V curve of a solar cell.

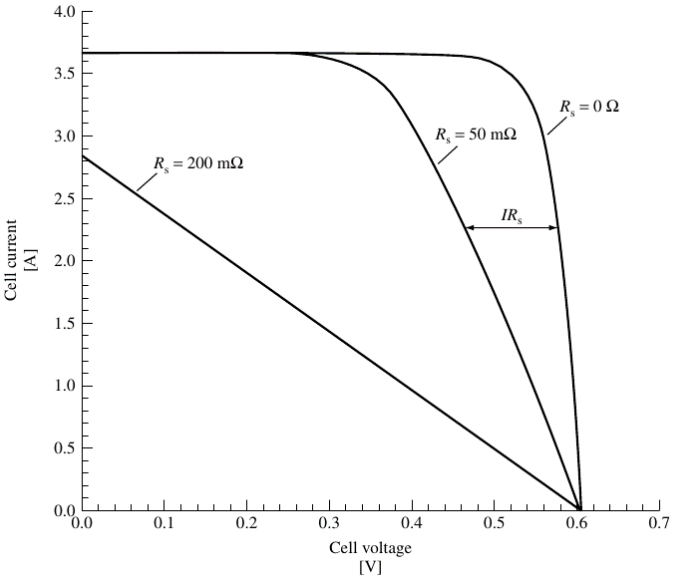

Figure 1-17: Effect of series resistance on the current–voltage characteristic of a solar cell ($R_{Sh} \rightarrow \infty$)

Parallel resistance R_{sh} (shunt): caused by leakage currents due to non-idealities and impurities near the P-N junction, besides imperfections in the structure, especially in the edges. Ideally, it has infinite value; however, by assuming lower values, the current passing through this resistance begins to increase, reducing the output current more and more drastically, until the point of the curve I-V becomes a straight line with slope 1 = R_{sh}. Typical values of this magnitude lie around units at tens of MΩ. Figure 1-18 shows the influence of the Rsh on the the I-V curve of a solar cell.

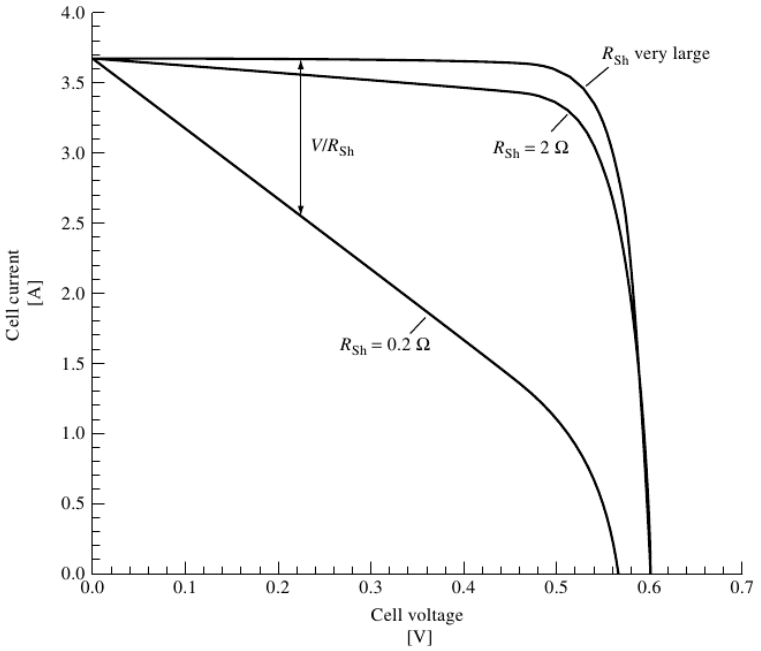

Figure 1-18: Effect of shunt resistance on the current–voltage characteristic of a solar cell (RS= 0)

2-Objectives

2.1 Objective of the thesis

The objective of this thesis is to investigate the biomimetic synthesis of ZnO and TiO_2 with suitable properties for use in DSSCs. In addition, compare performances of dye sensitized solar cells (DSSC) produced with the biomimetic powders with solar cells produced with commercial powders.

To reach the proposed objective, the following specific objectives need to be achieved:

- ✓ Characterize the ESMs that will be used as biotemplates;
- ✓ Evaluate the influence of parameters, such as type of precursor and heat treatment, on the synthesis of the oxides of interest in mimicking the ESMs;
- ✓ Characterize the material obtained regarding the properties of interest for DSSC applications;
- ✓ Compare characteristics of biomimetic powders with commercial powders;
- ✓ Produce DSSCs with different ZnO and TiO_2;
- ✓ Characterize the solar cells though current-voltage (I-V) curves.

3-Experimental Procedure

This thesis is divided into two parts. The first addressed the biomimetic production of ZnO and TiO_2, and its characterization compared with commercial ZnO and TiO_2. The second part of this work attempts to produced ZnO and TiO_2 DSSCs and compare the use of biomimetic or commercial powders in photovoltaic energy conversion in cells produced with and without use of dye.

Figure 3-1 shows a fluxogram of the methodology used for the production of ZnO and TiO_2 powders by the biomimetization of ESMs. At this stage of the study, chicken eggs were purchased from local markets and the membranes were manually separated. Once the membranes were removed and washed with water, they were submerged in a solution of acetic acid (cloridric acid also can be used) for about one day. Then they were removed, rinsed again in distilled water or ethanol (in the case of TiO_2 production) and submerged in the precursor solutions, where they stayed for 24 hours so the hydrolysis and condensation reactions could occur.

After the immersion period, the membranes were removed and air dried for at least 48 hours. The third step in the production of oxides was the calcination of the hybrid membranes. In this step the organic material is volatized and the oxides form. For this, we used a muffle furnace with a heating rate of 150°/h with a 30 min threshold. The calcination temperatures studied were 600, 700 and 800°C. Subsequently, the oxide materials formed were characterized.

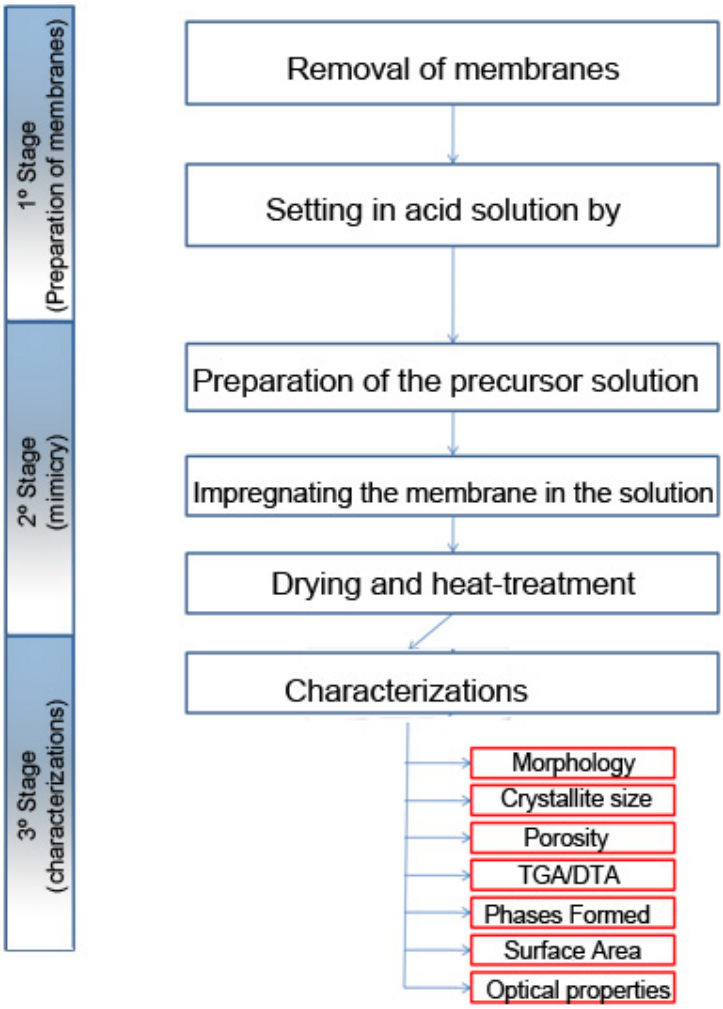

Figure 3-1. Flowchart of the steps to obtain the biomimetic zinc oxide and titanium dioxide.

The last part of our research was the comparison of the performance of the biomimetic powders in DSSCs. For this purpose, DSSCs were constructed with biomietic and commercial ZnO and biomimetic and commercial TiO_2 the as photoanode of the solar cells. DSSCs with these photoanodes were constructed with dye and without dye.

3.1 Materials

The complete list of materials used on the thesis reads as follows:

- Commercial white egg shell membranes.
- Zinc nitrate (pure hexahydrate from Thomas Scientific).
- De-ionized water (resistivity > >1 MΩ·cm).
- Acetic acid 99.8%, anhydrous (Scharlau).
- Titanium Isopropoxide, label Aldrich (97% purity).
- FTO glass (Sigma-Aldrich - 7Ω/sq).
- Ethanol (≥95.0% vol.).
- Ethylene glycol, anhydrous, 99.8% (Sigma-Aldrich).
- X100 Sigma-Aldrich Triton™ laboratory grade.
- 91245 Aldrich N749 Black Dye

Diluted acetic acid in distilled water was used to remove $CaCO_3$ in the laboratory. The acetic acid used was reagent grade glacial acetic acid of the Scharlau brand.

In the first part of the work, for the synthesis of biomimetic ZnO, aqueous solutions were prepared using distilled water, and, as the source of zinc, zinc nitrate hexahydrate, zinc acetate dihydrate and zinc chloride, all reagent grade and of the Scharlau brand. With zinc nitrate and zinc acetate solutions, was produced ZnO by precipitation method. In this case, the solutions were precipitated by addition drop by drop of NH_4OH (P.A. grade, label Synth). In the second part of the work (to produce biomimetic powders for the DSSCs) it was used zinc nitrate hexahydrate label Sigma-Aldrich, P.A. grade.

For the synthesis of TiO_2, an alcohol solution was prepared that used extra pure ethanol 96% v/v of the brand Scharlau. In the first part of the work (about the biomimetic synthesis), $TiCl_4$ from Fluka (98% purity) was used as a source

of Ti. In the second part of the work (for the production of biomimetic powders for DSSCs) it was used Titanium Isopropoxide, label Aldrich (97% purity).

3.2 Methods

The description of the methodology used in this study is divided into two sections. First, in section 3.2.1 we describe how nanostructured ZnO and TiO_2 was obtained, and, subsequently, in section 3.2.2 is described how the photovoltaic device assembly.

3.2.1 Synthesis of ZnO and TiO_2

First, the organic membranes must be removed from the inorganic ($CaCO_3$) eggshell. So, we first developed a method to isolate each membrane. The inner membrane (IM) is easily removed manually, leaving the outer membrane (OM) attached to the inorganic $CaCO_3$. Therefore, for the use of the IM isolated, it was removed manually from the shell with careful for not remove the OM. After that, the OM was isolated by dipping the remaining shell with the OM in an acid solution for about 48 hours. This leads to the dissolution of $CaCO_3$ and, therefore, to the isolation of the OM. In order to use both the OM and IM, the eggshell with the two membranes must be soaked in an acid solution for about 2 days until the $CaCO_3$ layer is completely dissolved. In all cases, the membranes are submitted to a new acid solution to make sure that $CaCO_3$ is completely removed. Table 3-1 summarize the methods used for isolating the membranes. Preliminary investigations were carried out with the three membrane isolation methods and the subsequent studies were performed by separating the membranes manually.

Table 3-1: Membranes obtained and their respective methods for the isolation.

Obtained membranes	Proceeding
Inner Membrane	Mannual Removal
Outer Membrane	After manual removal of the inner membrane, the remainder ($CaCO_3$ + outer membrane) is placed in an acid solution to remove the inorganic part of the shell.
Inner and Outer Membranes	Removal of $CaCO_3$ through its dissolution in acid solution.

The second stage of the experimental procedure involves the mimicking the ESMs. In this step, manually removed organic membranes were first washed with water and immersed in a solution of acetic acid for 24h. Subsequently, the ESMs were removed from the acid solution and rinsed again with distilled water (for ZnO synthesis) or with ethanol (for TiO_2 synthesis). After this, the ESMs were immersed in the precursor solution for 24h. The ZnO precursor solutions tested were 0.25 M aqueous solutions of three different precursors: zinc acetate, zinc nitrate and zinc chloride. The TiO_2 precursor solution was prepared using a 0.05 M solution of $TiCl_4$ or Titanium Isopropoxide in ethanol. After the soaking process, the membranes were placed on a flat surface and dried at room temperature for at least 24h. After drying, the membranes were calcined at different temperatures (600, 700, and 800°C) with a threshold of 30 min.

at the maximum temperature and a heating rate of 100°/h. Figure 3-2 is shows a simple, step by step schematic of the mimicking of ESMs.

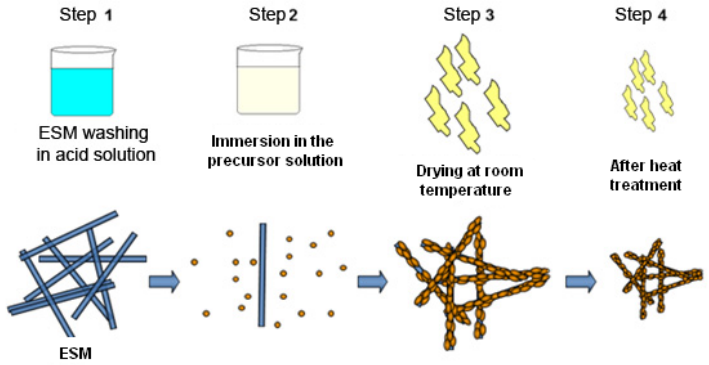

Figure 3-2: Schematic of the mimicking process of the ESMs.

For better understanding of the properties achieved with biomimetic synthesis of ZnO, ZnO obtained by biomimetization was compared with ZnO powders obtained by the precipitation method. To produce powders by precipitation, we started with aqueous solutions (zinc nitrate and zinc acetate) of in concentrations of 0.25 M each, and promote the precipitation adding slowly ammonium hydroxide (NH_4OH) until a white gel was formed. This gel was then filtered, dried and calcined. The powders of these solutions were called “nit CP” and “acet CP”, respectively. At the same time, from the remaining solution of the biomimetic synthesis, precipitated ZnO was produced with the addition of NH_4OH. These powders were called acet RP and nit RP when produced from the solution of zinc acetate and zinc nitrate respectively.

3.2.2 Preparation of the photovoltaic devices

To assemble DSSCs, Fluorine doped Tin Oxide (FTO) Glass from Sigma-Aldrich (surface resistivity ~7 Ω/sq) was used as substrate.

To prepare the glass substrates, FTO glasses were cut in the dimension of (30 × 15) mm. The counter electrode FTO glass was drilled with a 1 mm diamond drill in the geometric center. Subsequently, the assembly of the solar cells took place in the following steps.

FTO glass cleaning - The glasses were cleaned in an ultrasound bath for 10 minutes with 1% v/v detergent, 10 minutes with distilled water and 10 minutes with ethanol, in this order. The glasses were then dried with a jet of compressed air.

Deposition of porous oxide films in the photoanode - A slurry with the oxides was produced using approximately 0.3 g of oxide, 1 mL of ethanol, 18 μL of ethylene glycol, and 15 μL of Triton X-100. The deposition of a layer of TiO_2 or ZnO with 1 cm2 was made by doctor blade. The semiconductor layer was dried for approximately 5 minutes and then sintered in a muffle furnace at 450° C for 30min.

Deposition of the dye - Impregnation with the dye molecules was performed by leaving the glasses with the oxide layers dipped in a 0.2 mM alcohol solution of the commercial dye N749 BLACK DYE for 24 hours. After the immersion period, they were washed with ethanol and dried at room temperature.

Deposition of the catalyst and sealing of the cells - After drying, the perforated FTO glass was coated with graphite and carefully placed on the cell with a 50-micron thick polymeric spacer to form the counter electrode. The sealing of the cells was done with the aid of binder clips to facilitate the application of the epoxy adhesive along the contact edges.

Deposition of the electrolyte - The electrolyte used was the EL-HPE High Performance Electrolyte, brand Dyesol. It was deposited using a silicone nozzle syringe, which allows a good seal on the 1 mm hole in the counter electrode and the formation of a vacuum inside the cell as the plunger is moved out of the syringe body. After deposition of the electrolyte, the hole was sealed.

3.3 Characterizations

The characterization techniques used in this thesis are described in the following sections. Due to the work being developed in UPV and universities in Brazil, in some cases the characterizations were realized in more than one similar equipment. The Brazilian universities that collaborate to this work are UFRGS (Federal University of Rio Grande do Sul), UFPel (Federal University of Pelotas), FURG (Federal University of Rio Grande) and UFN (Franciscan University). A brief description of the techniques and equipment used is listed below:

3.3.1 Loss of mass and thermodiferencial analysis

To study the decomposition of the membranes when forming ZnO and TiO_2, termodiferencial analysis (TDA) and thermogravimetry analysis (TGA) was performed on two types of equipment. The first, located at UFRGS, was the Mettler (DTA/TGA A851e) apparatus, using a synthetic air atmosphere and a heating rate of 10°C/min until 800°C. Alumina was used as the reference material. The second device used was located at UPV and was a TA instrument, model Q50. This device was used with a heating rate of 10°C/min until 950°C using a nitrogen atmosphere.

For these analyses, small samples were prepared by cutting the pure or hybrid membranes into small pieces of approximately 1 mm^2. The calcined samples were easily transformed into powder using a mortar and pestle.

3.3.2 X-ray diffraction

To evaluate the formed phases and crystallite size of the obtained products, we used a PHILIPS X-ray diffractometer,

model X'Pert MPD, equipped with a graphite monochromator and a copper rotating anode, operating at 40 kV and 40 mA, and other two apparatus of the brand Bruker, model D2 PHASER, equipped with a copper anode and operating at 30 kV and 10 mA, but with a detector model lynxeye. The first equipment is located in LACER (UFRGS) and two Bruker equipment are located in the laboratory of surfaces (UPV) and analyses laboratory in UFN

The analyses were done in a scanning range of 2θ = 5° to 75°, with steps of 0.05°, for 1 second to identify the phases formed. To interpret the crystallite sizes, measurements were made in greater detail (steps of 0.01° with 8 seconds per step) in the range of the mains peaks of each phase according to Table 3-2:

Table 3-2: Angles of the measurements corresponding to the crystallite size analysis for each identified phase.

Phase	**2 θ**
Rutile	26.2° - 28.7°
Anatase	23.2° - 27.0°
Zincite	30.5° – 37.5°

Based on the broadening of the main peaks of each phase, the crystallite size was calculated with the Scherrer equation (Equation 3.1) using the EVA Bruker software.

$$d = \frac{K\ x\ \lambda}{\beta\ \mathrm{x}\cos\theta} \qquad \text{(Eq. 3.1)}$$

Where d is the crystallite size, λ is the incident wavelength, β is the peak width (taken at half height of the peak or full width at half maximum - FWHM) after correction of the instrumental error, θ is the Bragg angle and K is the Scherrer constant.

For all the XRD analysis, the samples were comminuted in an agate mortar and pestle.

3.3.3 Morphology

The morphology of the samples was first observed by scanning electron microscopy (SEM) and, afterwards, transmission electron microscopy (TEM) was used for higher magnifications. The scanning electron microscopy analyses were performed in the Center of Electron Microscopy of UFRGS and the Center of Microscopy of UPV. At UFRGS, we used a JEOL scanning electron microscope, model JSM 5800. At UPV, we used a JEOL scanning electron microscope, model JSM6300. The second microscope was used for the energy dispersive analysis of the semi-quantitative chemical composition of samples.

The TEM analyses were performed at the center of microscopy of UPV. We used a PHILIPS transmission electron microscope, model CM10.

3.3.4 Optical properties

Uv-Vis diffuse reflectance was used to estimate the direct bandgap. For this, the intensity of the reflected light is obtained by comparing it with a pattern (blank sample) whose properties are known. The reflectance measurement is then submitted to the following Equation 4.2

$$r_{am} = \frac{I_{am}}{I_{bra}} \times r_{bra} \qquad \text{(Eq. 3.2)}$$

Where r_{am} is the reflectance of the sample, I_{am} and I_{bra} are the intensities of the samples and of the reflected light by the blank sample.

The most widely used model for the interpretation of the data obtained from the reflectance spectrum is the Kubelka-Munk theory, from which the Kubelka-Munk remission function is obtained, which is given by Eq.4.3:

$$F(R_\infty) = \frac{(1-R_\infty)^2}{2R_\infty} = \frac{k}{s} \qquad \text{(Eq. 3.3)}$$

Where $F(R_\infty)$ is the sample reflectance, k is the absorption constant and s is the scattering coefficient. We can estimate the value of the bandgap of the semiconductor plotting the square root of the Kubelka-Munk function ($\sqrt[2]{(F(R_\infty))}$) by the excitation energy of the emitted photon. If we draw a straight line on the obtained graph, the value that intersects the x-axis (the axis E (eV)) is the estimated value of the bandgap.

The optical properties of the samples were measured in UPV using a Newport UV-VIS spectrophotometer in the wavelength range of 200-850 nm. The samples used to produce the solar cells were investigated using a spectrophotometer Ocean-optics HR-2000 equipped with an integrating sphere with two inches of diameter. Other measures were carried out in equipment Ocean Optics model DH-20000 equipped with an integrating sphere Ocean Optics model ISP-REF 2.2 located at departamet of physics of UFPel.

The fluorescence spectrum of the ZnO samples were analyzed using a Shimadzu RF5301 spectrofluorometer with excitation at 325 nm and observing the fluorescence of the sample in the range of 280 up to 700 nm.

3.3.5 Surface area analysis

The powders as obtained and commercial powders had their specific surface area determined from adsorption isotherms by the technique Branauer, Emmett and Teller (1938). The equipment used was the Autosorb Quantachrome (model NOVA

1200). This instrument calculates the total surface area of the sample through the volume of nitrogen adsorbed in the powder surface as a function of the relative pressure measured in the equipment. The specific surface area is then measured by dividing the total weight of the sample (g) by the surface area measured by the equipment (m_2). Prior to each analysis, the samples were held at 300° C for 3 hours to remove moisture.

3.3.6 Chemical composition analysis

Semiquantitative analyses were performed using energy dispersive X-ray detector (EDS) coupled to the SEM. X-ray. The SEM utilized for these analyses was the same JEOL model JSM6300 located in the Center of Microscopy of UPV. For each sample, 4-point measurements of EDS were made and the means were calculated.

3.3.7 Photovoltaic characterizations

Photocurrent-voltage I-V measurements were performed using a Source Measure Unit (SMU) with 4 channels interfaced and a stabilized polychromatic light source with irradiance equal to 1000 W/m^2.

4-Results and Discussion

In this section different aspects involved in the process to obtain the biomimetic oxides will be presented and discussed in the following sub-items.

The sub-items 4.1 to 4.11 are dedicated to present and discuss some results related to the biomimetic synthesis of ZnO and TiO_2. The sub-items 4.11 and 4.12 are dedicated to compare properties of the powders used for the construction of DSSCs and discuss the photoconversion performance of the mounted devices.

4.1 Morphologic study of the eggshell

Prior to the biomimetic synthesis, a morphological study of the eggshells was performed to a better understand of its morphology. The SEM images clearly revealed the structure of the eggshell and its membranes. Figure 4-1 shows the micrographs of the eggshells in natura (only cleaned and dried at 110°C).

In Figure 4-1 the morphological characteristics of the eggshells and its membranes can be observed. The thicknesses

measured in the images with the aid of the Image J software are consistent with those found in the literature. The inner membrane (IM) was approximately 19 µm in thickness and the outer membrane (OM) about 58 µm with the fibers ranging from 1.2 to 4.3 micrometers in diameter. We could also observe that the inner part of the IM (Figure 4-1,(f)) has a smooth surface with few pores. This inner surface is described by Hincke, et al. (2000), as the limiting membrane (LM). This is what separates the albumen from the ESMs. In Figure 4-1 (h) one can also observe that the outer surface of the OM has protrusions in the form of buttons. According to Nys and Gautron (2007), some organic centers are deposited on the surface of the OM during the passage of the egg through a given region of the oviduct. These are organic nucleating centers around which the calcium carbonate crystals begin to be deposited, starting with a spherulitic deposition of calcite microcrystals (calcium carbonate polymorphic shell) around these buttons, resulting in hemispheric nucleation centers. The internal mineralisation, however, is inhibited by the membrane structure and by the presence of collagen X, which facilitates this inhibition (Gautron and Nys, 2007).

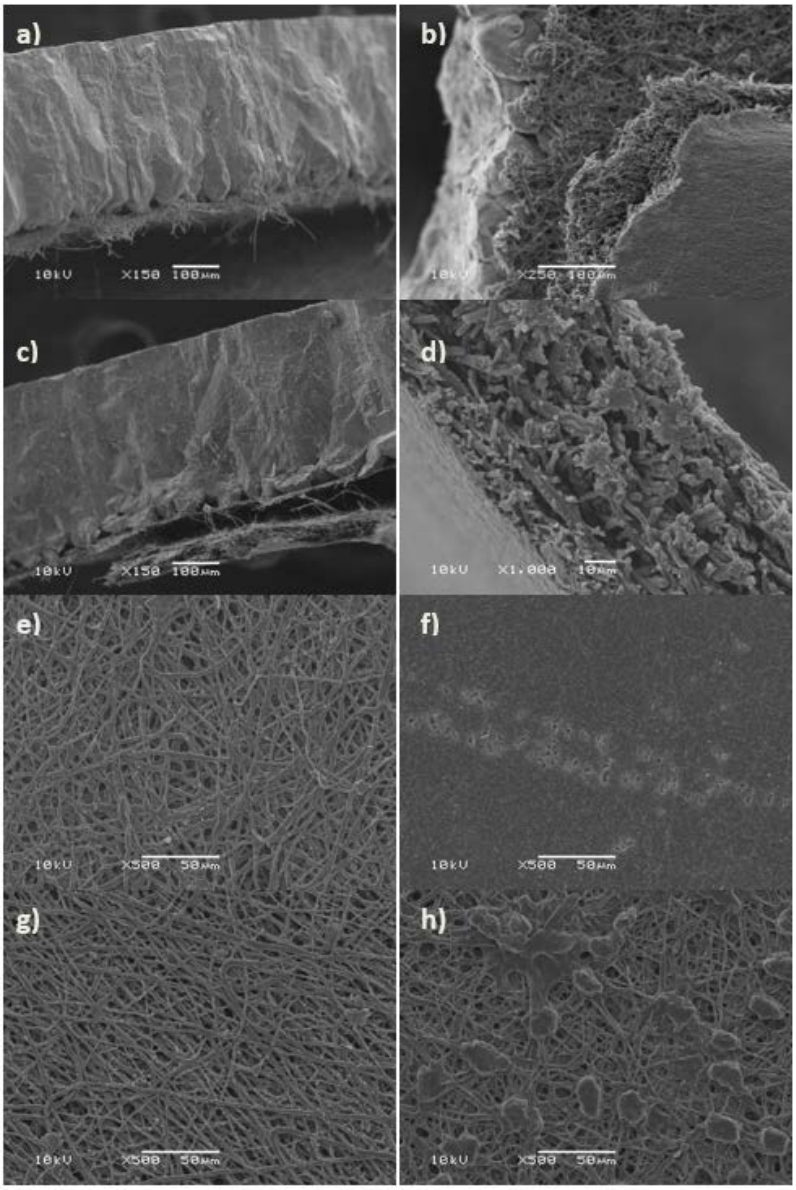

Figure 4-1: a) side view of an eggshell with its membrane partially removed. b) eggshell and its membranes. c) side view of an eggshell and its different layers. d) side detail view of an ESM. e) top view of the outer face of an IM. f) top view of the internal face of an IM. g) top view of the inner face of an OM. h) top view of the outside of OM.

4.2 Morphological differences between TiO_2 powders produced with different membranes

The removal procedure of the organic membranes from the inorganic part of the eggshells is an important step, and, with different extraction methods, it is possible to remove different types of membranes (IM, OM or both). In laboratory scale, manual removal is the fastest and easiest way to separate a small amount of ESMs, but by this way, usually occurs the removal of only the IM and the OM stay adhered in the inorganic part of the eggshell. To obtain ESMs in large scale, the manual removal process probably is not viable, because it would spend too much time and labor to obtain a reasonable amount of membranes. Dipping the entire shell in an acidic solution could be the most suitable alternative for obtaining a large amount of membranes. In this case, the isolation of the organic membranes occurs when the inorganic material is completely dissolved for an acid (e.g. hydrochloric acid or sulfuric acid). The documented procedures for the synthesis of TiO_2 by mimicking the ESMs, usually are done removing manually the membranes, but in the article of Yang et al. (2002), they use only the OM through the manual removal of the IM and subsequent washing the shell with the OM in acid. Therefore, using different methods of removal of the membranes and immerging in a 0.05 M $TiCl_4$ alcoholic solution (described in section 3.2.1), it was obtained the reproduction of the membrane structures in the form of TiO_2. The micrographs can be seen in Figure 4-2.

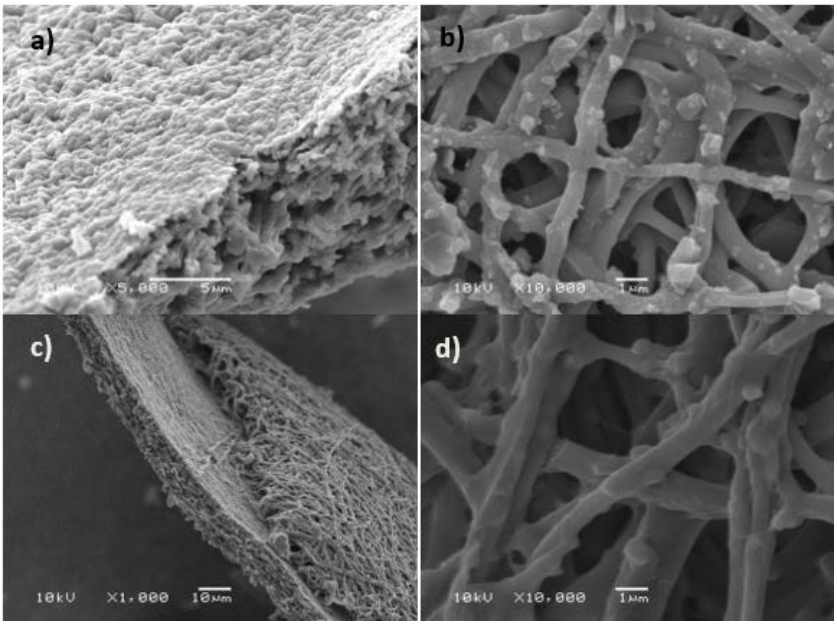

Figure 4-2: Micrographs of biomimetic TiO_2 obtained by the mimetization of the inner membrane (IM) (a) and (b), inner membrane (IM) over the outer membrane (OM) (c) and the outer membrane (OM) (d).

The measured thickness of the biomimetized membranes was 9.8 and 16.5 µm for IM and OM, respectively. The fiber diameter varied from 0.36 to 1.4 µm. The IM fibers apparently had slightly smaller diameters than the OM fibers as well as smaller sizes than the sample of ESM in natura. It is also possible to observe in Figure 4-2 (a) that the calling Limiting Membrane (the innermost part of the IM) is also replicated. It is therefore possible to conclude that the membrane structure was accurately mimicked in TiO_2, with a considerable reduction in its dimensions.

4.3 Decomposition of the in natura and hybrid membranes with titanium (effect of the firing atmosphere)

The mimicking process involves the thermal decomposition of the membranes so that its organic structure is volatilized, leaving the new inorganic structure. At this stage we studied the thermal decomposition of the membrane first under a synthetic air atmosphere and then under a N_2 atmosphere. Figure 4-3 shows the TG and TD analysis carried out in a synthetic air atmosphere for a dried ESM. This analysis shows that initially (until 120°C) a small mass loss of about 10% occurs, associated with evaporation of the adsorbed water in the membrane. At about 250°C, a marked weight loss occurs that is associated with an exothermic peak because of the pyrolysis of the organic membrane. In air atmosphere, the membrane is completely pyrolyzed only at temperatures close to 600°C. The temperature values to start the pyrolysis of ESMs differ slightly in the literature. Yang et al. (2002), state that the membrane starts to pyrolyze at 270°C and that it is completely pyrolyzed at 500°C. In the study of Dong et al. (2007a) and Dong et al. (2007d), the authors stated that the membrane starts pyrolysis at 200°C and that the complete burning of the membranes occurs at 550°C.

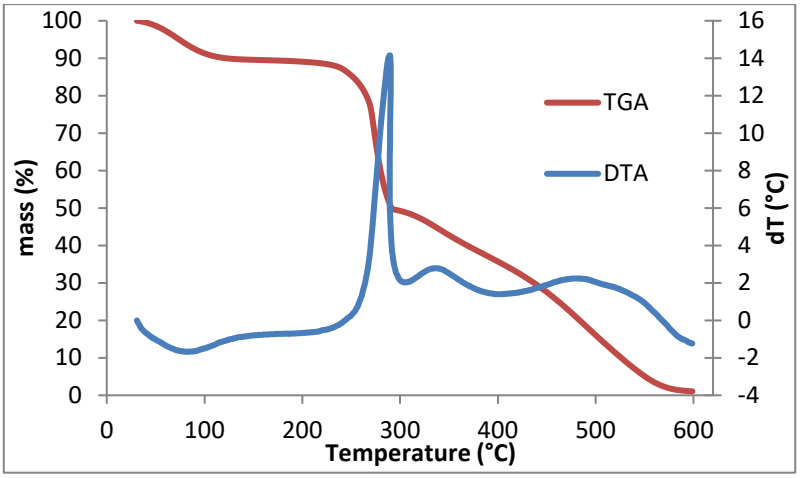

Figure 4-3: TGA/TDA of a dried sample of ESM

These differences in values could be attributed to small differences in the analyzed samples, or to instrumental factors. In Figure 4-3, three exothermic peaks can be seen at approximately 288, 335 and 476°C. These peaks can probably be attributed to the pyrolysis of different proteins present in the ESM structure.

The TG analysis under N_2 atmosphere (Figure 4-4) revealed a distinct decomposition behavior of the membrane in natura compared to the decomposition in artificial air atmosphere. This is due to the lack of oxygen for the volatilization of organic material in the form of CO_2 when the sample is burned in neutral atmosphere (N_2). By contrast, the hybrid sample fired in N_2 atmosphere showed a more rapid volatization of the organic matter and the stabilization of its mass occurred with temperatures exceeding 600°C. Probably. the formation of titanium compounds with oxygen and hydrogen during the hydrolysis and condensation process of the precursors on the surface of the ESMs provides sufficient oxygen for the oxidation reactions and subsequent volatilization of the organic matter of the membranes. This means that in a neutral (N_2) atmosphere, the loss of mass of the hybrid membrane is more pronounced than that of the membranes in nature. After about 620°C, about 11.81% by weight of TiO_2 remains.

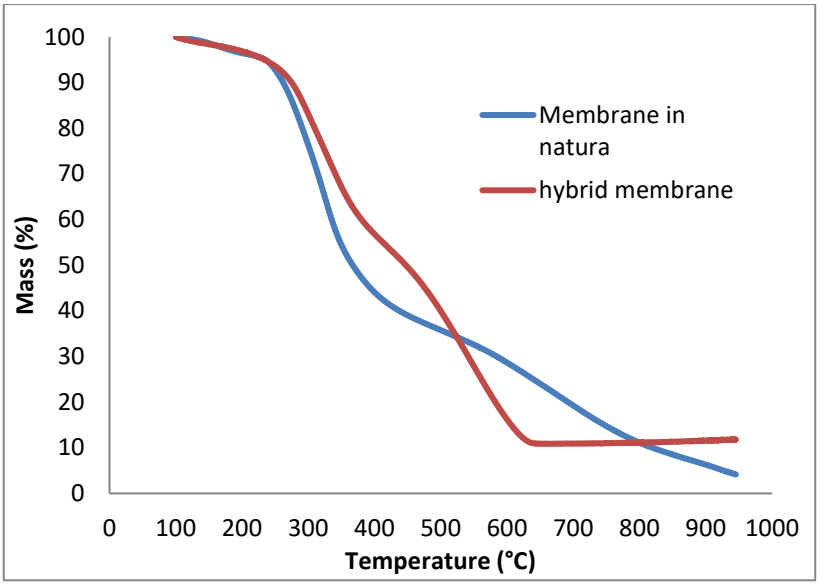

Figure 4-4: ATG in N_2 atmosphere of hybrid membrane and a membrane in natura

4.4 Decomposition of hybrid membranes prepared with different sources of zinc

As the hybrid membranes calcinate, the crystallization of ZnO and the volatilization of the organic membrane occurs simultaneously. In the TG analyses performed under N_2, we could observe that the volatilization of ESMs is influenced by the presence of the precipitation products of the Zn reactions. In the graph of Figure 4-5 we can observe that the pure membrane is completely decomposed at the end of the analysis around 950°C. Similarly, the hybrid membrane prepared using a solution of zinc nitrate apparently does not stabilize its mass until 950°C, which means there was no complete combustion of the organic membrane. On the other hand, the hybrid membrane prepared with zinc acetate had a constant mass at about 800 °C. In this case, the hydrolysis and condensation reactions are probably responsible for forming Zn compounds with larger amounts of

oxygen. This may explain the faster volatilization of the organic mass, which is first carbonized and then volatilized, mostly in the form of CO_2.

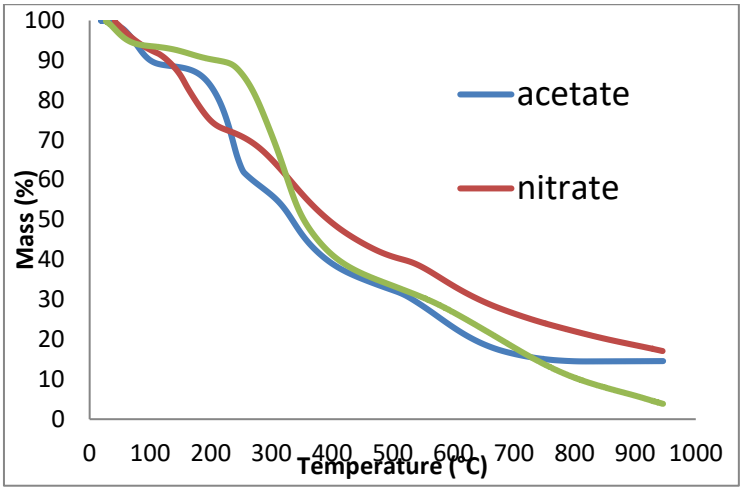

Figure 4-5: TGA of the samples prepared with different precursors

In the works of Dong et al. (2007c), Dong et al. (2007b) and Dong et al. (2008), the TG analyses left a residual mass of 17.9 and 25.2% of ZnO. In our samples, the residual mass presented by the hybrid sample with acetate was approximately 14.6% at about 800°C, while the hybrid sample with zinc nitrate presented residual mass of 17.2% at 950°C. However, we must note that even at higher temperatures, the sample prepared with zinc nitrate did not show a constant mass. This could mean it continues to decompose at higher temperatures under N_2 atmosphere.

4.5 Effect of the thermal treatment temperature on the phase formation of biomimetic TiO_2

The study of phases formed and grain growth in biomimetic TiO_2 also revealed the possibility of the formation of two phases (anatase and rutile) depending on the thermal treatment.

Through XRD analysis, it was possible to observe that only anatase crystallized at 600°C. Starting at 700°C, small peaks appear corresponding to the rutile phase. Because rutile is a stable phase, the peaks related to rutile continue to increase and, at 800°C, rutile is the predominant phase in relation to anatase. This phase transformation is expected for temperatures above 600°C. Prasad, et al. (2010), however, reported the transformation of anatase to rutile for temperatures above 650°C with either conventional heat treatment or with ultrasonic assisted heat treatment for samples prepared by sol-gel. Shao, et al. (2004) also observed the incipient formation of rutile at 600°C.

A more detailed XRD analysis of the major peaks for each phase employing the Equation 4.1, helped establish the average crystallite size (Table 4.1) for the anatase e rutile phases. We were able to verify that it is a nanostructured material. We also observed that the rutile phase has a very fast growth rate, even in smaller amount than that of anatase (observed by the relative heights of the peaks of anatase and rutile). At 700°C, rutile already has a larger crystallite size than that of the anatase phase, which was formed first.

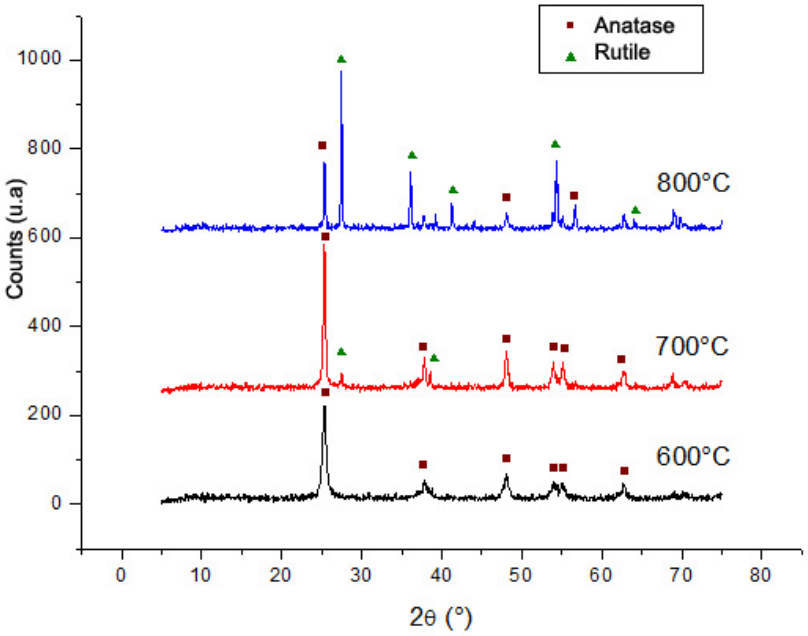

Figure 4-6: XRD of the TiO_2 samples calcined at 600, 700 and 800°C.

Table 4-1: Average crystallite sizes of the TiO_2.

	600°C	**700°C**	**800°C**
Anatase crystallite sizes (nm)	15.82	30.73	60.94
Rutile crystallite sizes (nm)	-	58.01	86.03

4.6 Effect of the thermal treatment temperature on the phases formation for biomimetic and precipitated ZnO

The samples prepared using nitrate and zinc acetate produced by biomimetization (biomimetic), precipitated from the residual solution (RP) or precipitated from a control solution (CP) had their phases and crystallite size analyzed by XRD. In all samples, only the zincite phase of the zinc oxide was identified. Figure 4-7 shows the XRD patterns obtained from samples prepared with zinc nitrate. The diffractograms only differed in the peak broadening, and for some samples, crystallite sizes of the order of a few nanometers were obtained.

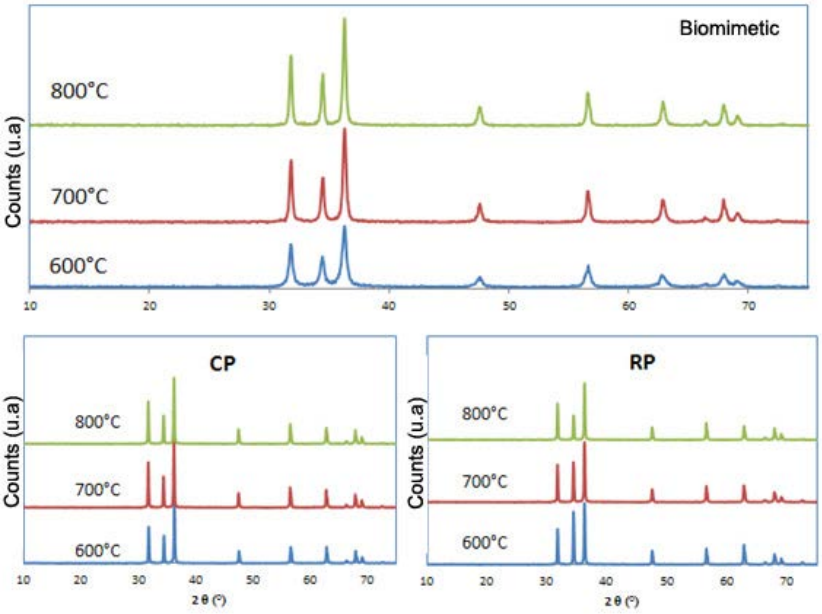

Figure 4-7. XRD patterns of samples prepared by biomimetization of the ESMs (Biomimetic), the samples precipitated from the control solution (CP) and the samples precipitated from the remaining solution of the biomimetization process (RP).

The average crystallite size, estimated by the Scherer equation (Eq. 3.1), of the samples prepared using nitrate and acetate are depicted in Table 4.2.

Table 4-2: Average values of crystallite sizes of the zincite samples.

	600°C	**700°C**	**800°C**
Biomimetic Nit	28.99 nm	44.23 nm	48.18 nm
Nit RP	103.38 nm	95.62 nm	94.62 nm
Nit CP	86.98 nm	95.83 nm	99.82 nm
Biomimetic Acet	25.65 nm	34.86 nm	49.93 nm
Acet RP	50.72 nm	63.56 nm	81.67 nm
Acet CP	58.74 nm	79.13 nm	105.68 nm

Figure 4-8 shows the XRD patterns of the major peaks of the zincite phase, from samples prepared using the zinc nitrate solution.

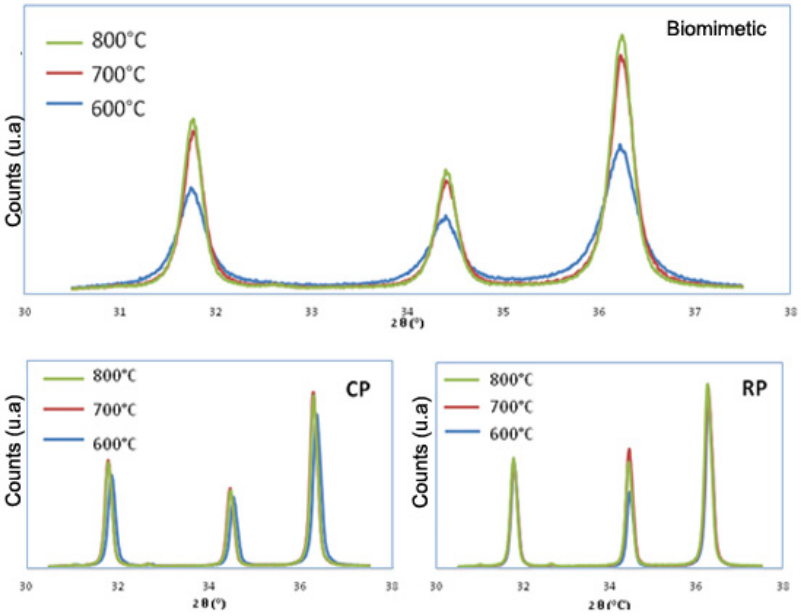

Figure 4-8. Diffractograms of the main diffraction peaks for the different zincite samples prepared with nitrate.

The crystallite size measurements revealed that, irrespective of the precursor used, the samples prepared using the ESMs as a biotemplate had a lower crystallite size than the samples produced by precipitation. This small crystallite size of the biomimetic ZnO, is probably a consequence of the large amount of crystal nuclei formed on the surface of the ESM fibers. These crystals could be competing with each other in their growth. Another hypothesis is the presence in the ESMs of elements such as sulfur, which interact with the grain growth of ZnO when volatilized during firing, reacting mainly at the grain boundaries and hindering the growth of zincite grains.

The sample prepared with zinc acetate and calcined at 700°C was analyzed by TEM to confirm the crystallite size measurements. As can be seen in Figure 4-9, the crystallite size measured by XRD is in agreement with those measured by TEM,

since the crystallite size measured by TEM ranged between 25 and 47 nm in diameter.

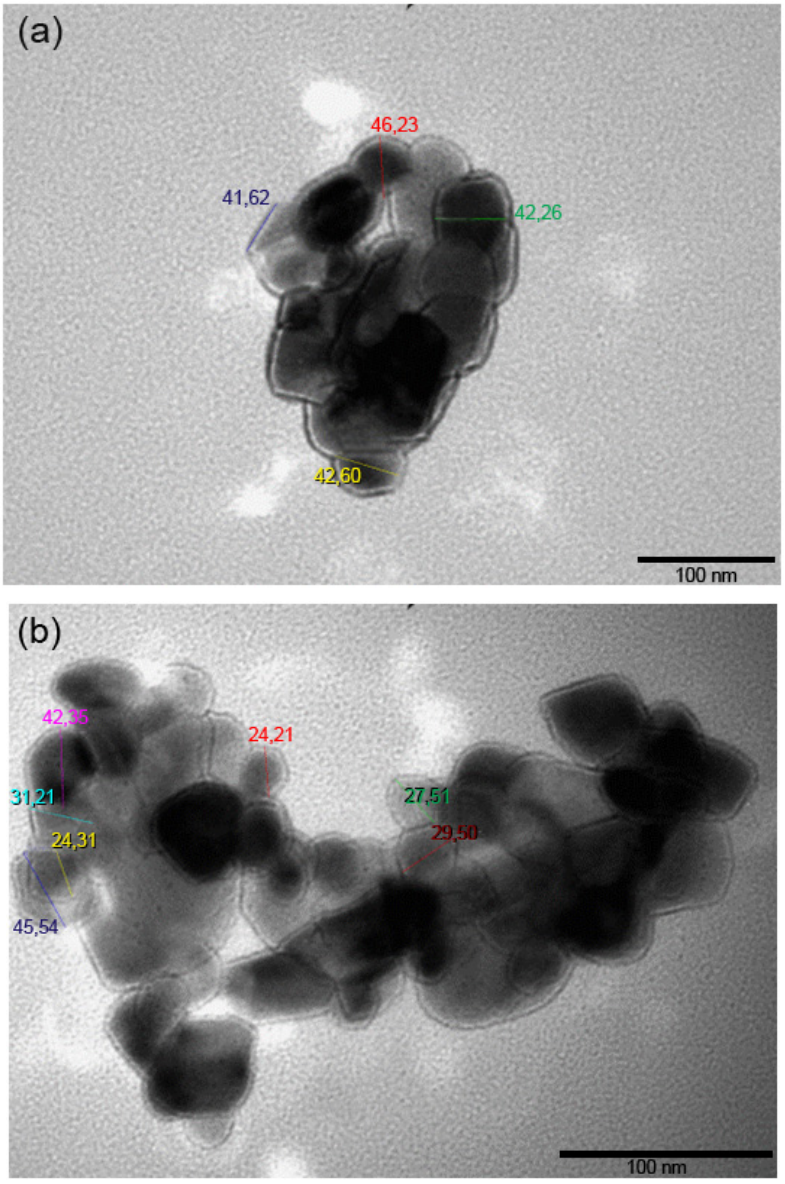

Figure 4-9: TEM of the sample prepared with zinc acetate and calcined at 700°C.

4.7 Effect of thermal treatment temperature on the morphology of biomimetic oxides

In the biomimetic synthesis of ZnO, the samples prepared in aqueous solutions of zinc acetate and nitrate, and calcined at different temperatures (600, 700, and 800°C) were analyzed by SEM. Through this analysis, it was possible to observe that the microstructure of the membranes was reproduced. This means that the hydrolysis and condensation of the inorganic phase occurred on the surface of the ESM fibers, giving rise to new, solid ZnO fibers in the same shape as the ESMs for both the precursors. Figure 4-10 shows that the microstructure of intertwoven fibers of ESMs is maintained even after calcination at 800°C. Due to the self-assembling behavior of the hydrophilic groups of the ESM glycoproteins, the Zn precursors crosslinked and polymerized to form biotemplate/inorganic phase complexes that were mesoscopically ordered. As the calcination temperature increases, it is clear that the material becomes more brittle and powdery. This can be attributed to the grain growth of ZnO when the temperature increased, making the fibers more fragile.

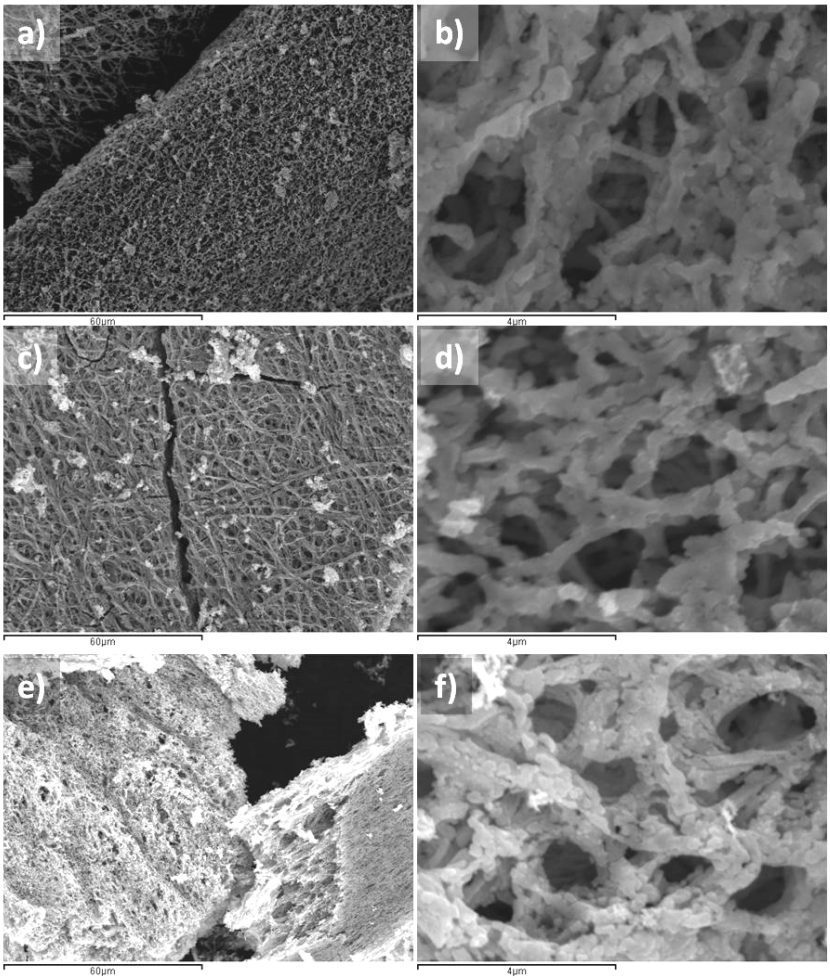

Figure 4-10: Micrographs of ZnO samples prepared using nitrate and calcined at 600°C (a and b) 700°C (c and d) and 800°C (e and f).

Figure 4-11 shows the micrograph of the sample prepared with zinc acetate as precursor. One can see that the membranes are also replicated when using zinc acetate as precursor.

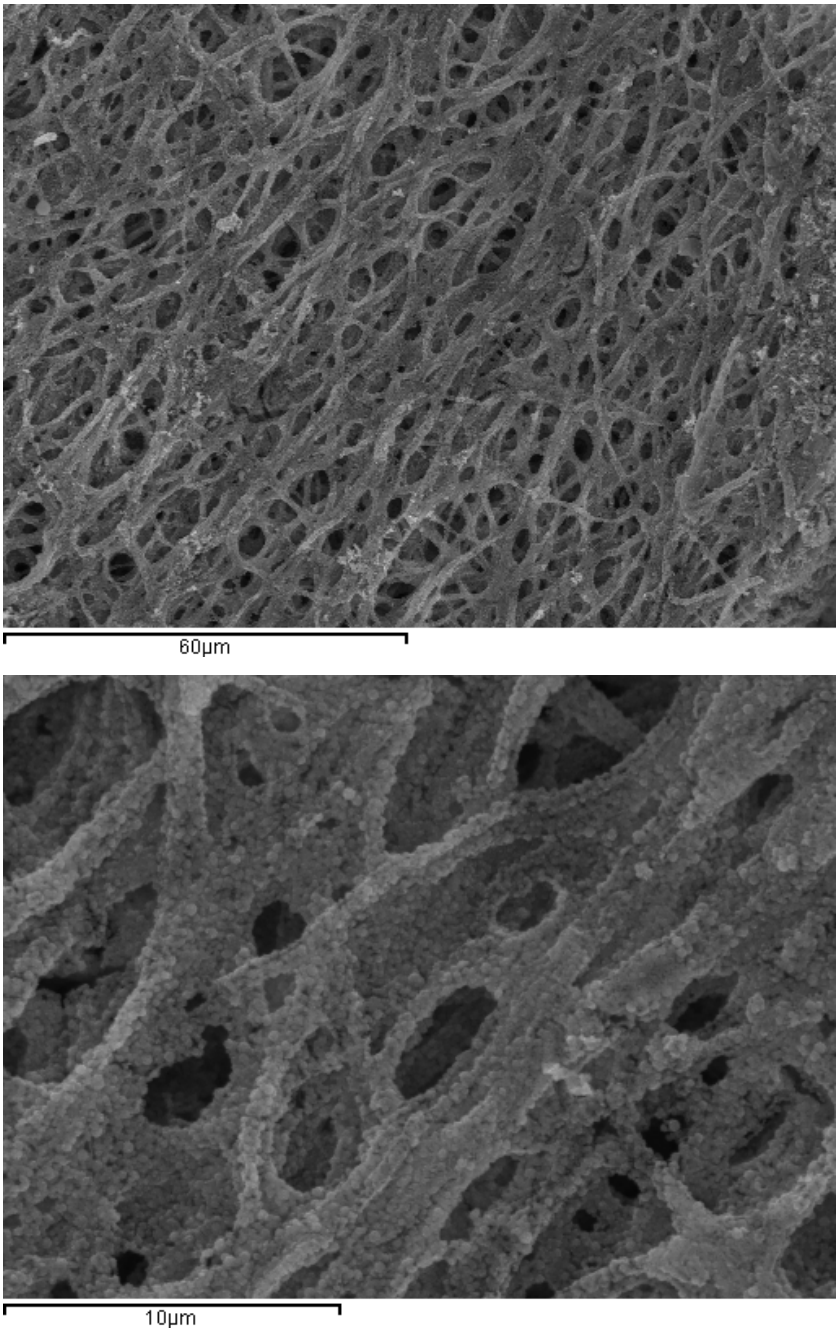

Figure 4-11: Micrograph of the sample prepared with zinc acetate and calcined at 600°C.

In the case of the biomimetic synthesis of TiO_2, we can see that the microstructure of the ESM fiber is replicated with fidelity for the synthesis temperatures tested. The phase transformation from anatase to rutile involves a change in density of 3.8 g/cm^3 for anatase to 4.25 g/cm^3 for rutile. A change in the morphology of the material obtained with the different phases should therefore also be expected. However, SEM analyses showed that even when the phases changed, the structure of interwoven fibers held together. An increase in surface roughness can be observed, however, because of the presence of the new rutile crystals (Figure 4-12).

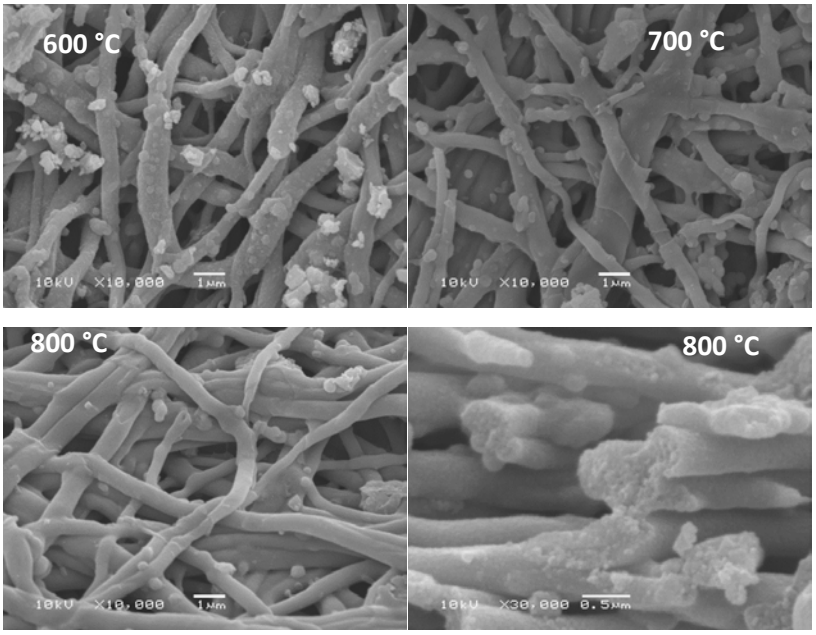

Figure 4-12: Biomimetic microstructure of TiO_2 obtained at different calcination temperatures.

4.8 Identification of contaminants of biomimetic ZnO

It has been established that the eggshell membranes are formed of organic compounds that are volatilized when burned at temperatures exceeding 600°C. EDS analyses performed in SEM

revealed the presence of small amounts of phosphorus and sulfur in the biomimetic ZnO, mainly in samples calcined at lower temperatures.

In Figure 4-13 and Figure 4-14 the EDS analysis is shown of the ZnO samples produced by biomimetization with zinc nitrate and zinc acetate, respectively. Sulfur peaks can be observed in all samples. In both the samples prepared using nitrate and those prepared using acetate, the peak intensity of sulfur is quite low and decreases with increasing calcination temperature.

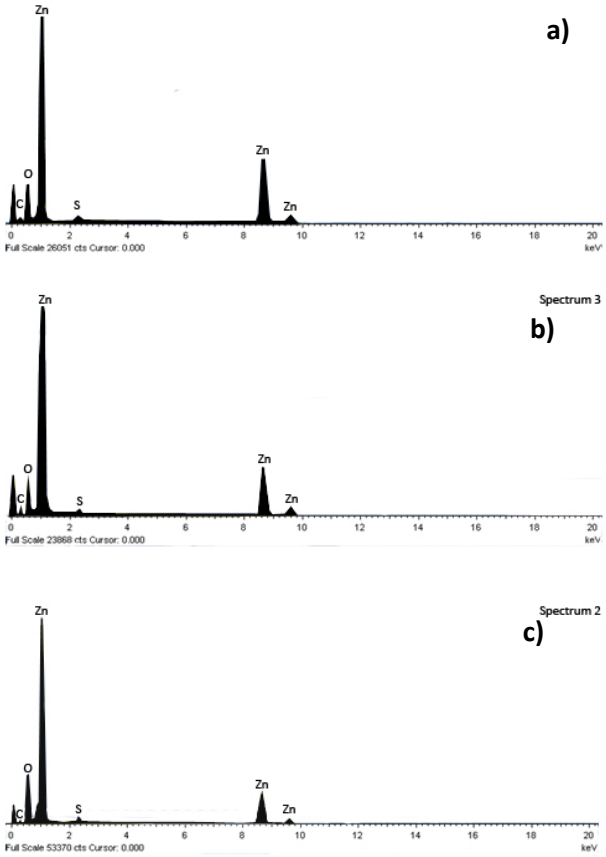

Figure 4-13: EDS elemental analysis of biomimetic samples prepared with zinc nitrate burned at 600°C (a) 700°C (b) and 800°C (c)

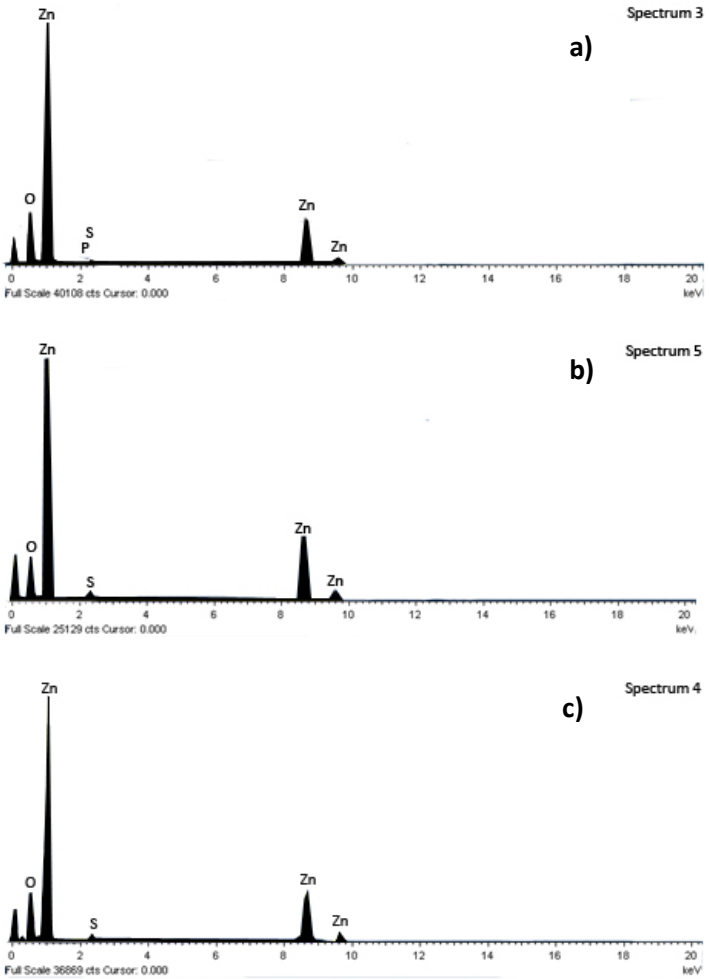

Figure 4-14: EDS elemental analysis of biomimetic samples prepared with zinc acetate burned at 600°C (a) 700°C (b) and 800°C (c).

This small amount of sulfur and phosphorus found in the samples prepared by biomimetization can be attributed to the burning of the sulfurated organic compounds of the ESMs, because in the EDS analysis of the samples prepared by precipitation of precursors, fired at 600°C (Figure 4-15), the presence of elements such as sulfur and phosphorus was not identified, which means purer ZnO samples. In Table 4.3 the mean values of 4 EDS measures for each sample are shown.

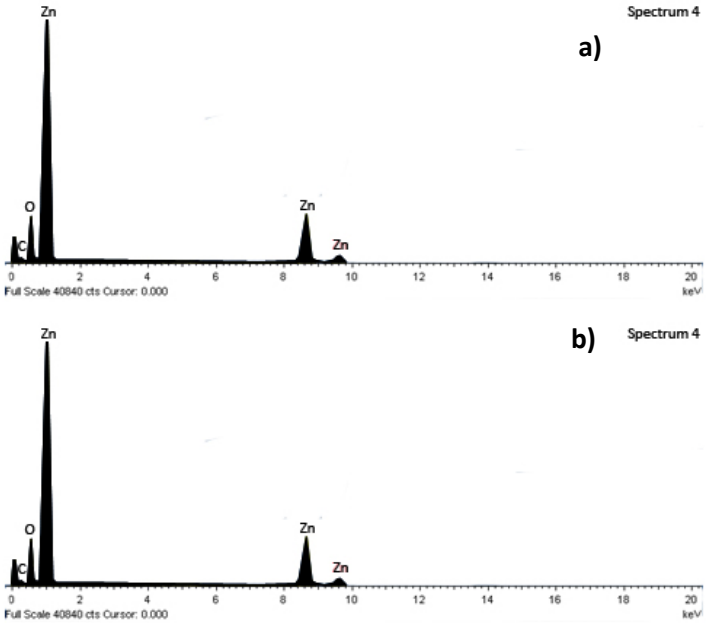

Figure 4-15: EDS elemental analysis of the samples calcinated at 600° prepared by precipitation (CP) without the presence of ESMs (a) using zinc acetate and (b) zinc nitrate

Table 4-3: Amounts of sulfur and phosphorus detected by EDS in the samples.

	P (% atomic)	**S (% atomic)**
Acetate 600 °C	0.09	0.68
Acetate 700 °C	0	0.36
Acetate 800 °C	0.175	0.18
Nitrate 600 °C	0	0.79
Nitrate 700 °C	0.05	0.35
Nitrate 800°C	0	0.22
Acetate CP 600 °C	0.0425	0
Acetate CP 700 °C	0	0
Acetate CP 800 °C	0.04	0
Nitrate CP 600 °C	0.0475	0

Nitrate CP 700 °C	0	0
Nitrate CP 800°C	0	0

4.9 Optical properties of biomimetic TiO_2 thermal treated in different temperatures

The study of the optical properties is essential for a semiconductor material whose purpose is the application as an electrode in DSSCs. As a comparison, we studied the optical behavior of TiO_2 produced by biomimetization of ESMs. The analysis of the diffuse reflectance of the TiO_2 samples (Figure 4-16) shows different behavior for the samples calcined at various temperatures. As is expected for TiO_2, there is a clear jump of reflection in the 300-400 nm range. The lower the calcination temperature, however, the more the jump in reflection is shifted to lower wavelengths.

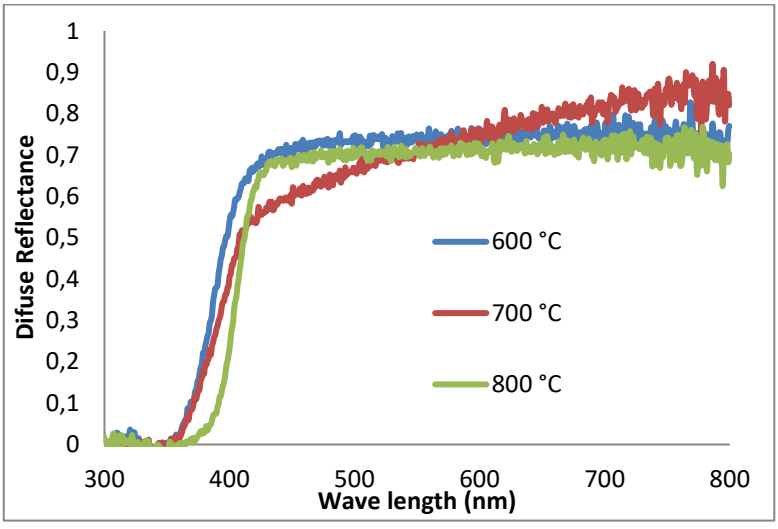

Figure 4-16: The diffuse reflectance of the TiO_2 samples calcined at 600, 700 and 800°C.

When a semiconductor absorbs photons with energies greater than its bandgap, an electron is transferred from the valence band to the conduction band, resulting in an abrupt increase of the absorption value indicating its bandgap energy. When the electron's momentum is conserved in this transition, the transition is direct. If the momentum is not conserved, however, there must be the participation of a photon. This is called, therefore, an indirect transition. The anatase phase has only indirect transitions, while the rutile can experience both types of transitions (Valencia and Juan Miguel Marín, 2010). The sample thermally treated at 600°C has an absorption maximum at lower wavelengths than the one treated at 800°C. This is caused by the predominance of rutile in the sample treated at 800°C. The indirect bandgap value was calculated using the Kubelka-Munk mathematical method (Valencia and Juan Miguel Marín, 2010); (Tsai and Cheng, 1997); (Morales et al., 2007). These results (Figure 4-17) are in agreement with the diffraction results, since the sample with a predominance of the rutile phase (calcined at 800°C) is also the one with the lowest bandgap (3.07 eV). The sample that was thermally treated at 700°C showed a unique reflection response, probably because of the incipient rutile growth, which can cause a disordering of the anatase structure. The curve obtained with the Kubelka-Munk treatment is less defined, but it can be inferred that its bandgap value is about 3.27 eV. The sample that contains only anatase as crystalline phase (calcined at 600°C), showed the highest bandgap (3.31 eV). The values obtained are slightly higher than the values found in the literature, especially for samples with lower annealing temperature. This may be to the result of the presence of amorphous material or small variations in the stoichiometry of the samples.

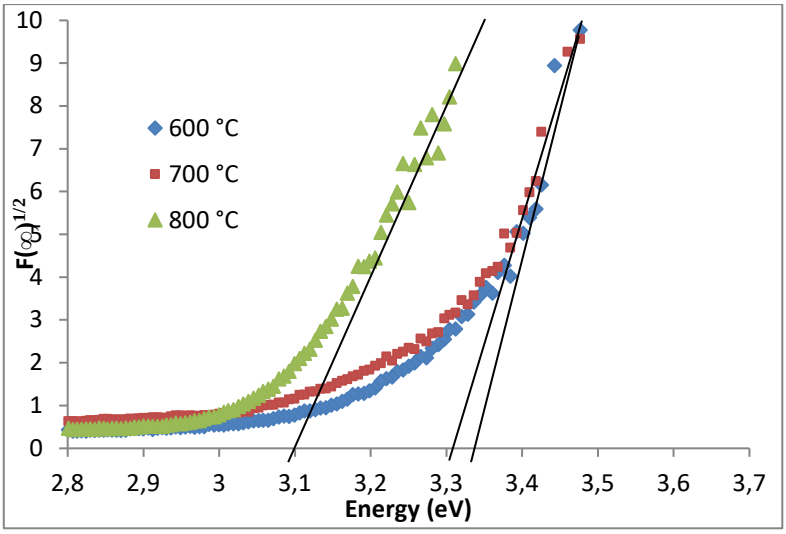

Figure 4-17: Reflectance spectrum with the Kubelka Munk transform for the TiO_2 samples.

4.10 Optical properties of biomimetic ZnO thermal treated in different temperatures

The optical behavior of ZnO depends both on the defects in its crystal structure as on the grain size and morphology of the particles. Figure 4-18 and Figure 4-19 present graphs of the diffuse reflectance and the Kubleka-Munk transform, which were used to calculate the bandgap values for the samples produced with nitrate and zinc acetate, respectively.

The diffuse reflectance analysis enables us to observe that the lower the calcination temperature, the lower the reflectance of the samples for wavelengths above 400 nm is. A couple of reasons could be responsible for this. One is the presence of charred residues of the ESMs that are still present in small amounts in calcinations up to 700°C. Another reason is the low crystallinity of the samples burned at low temperatures combined with the presence of impurities within the structure of the produced ZnO.

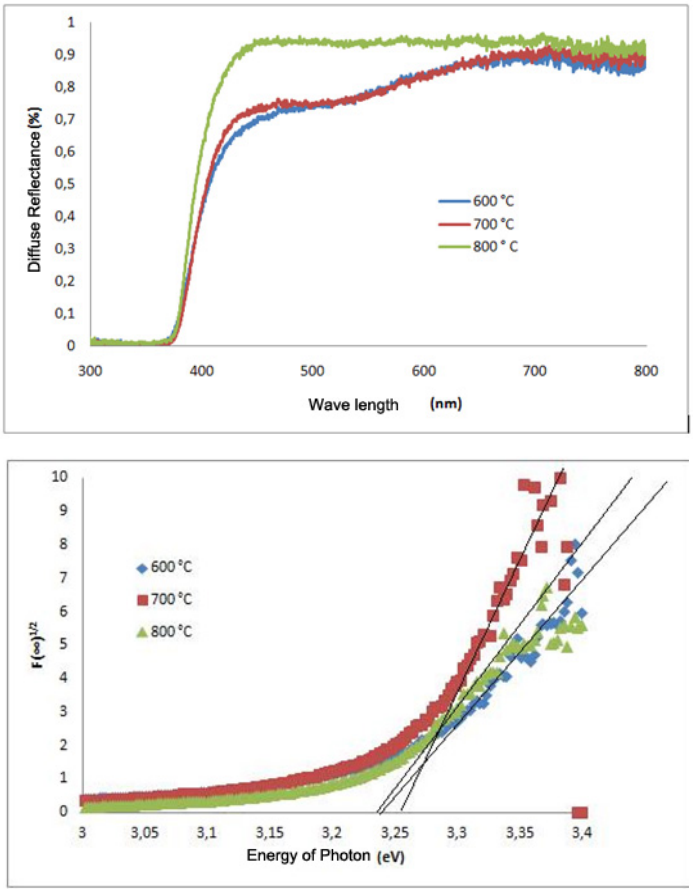

Figure 4-18: Diffuse reflectance and Kubelka-Munk transform to the samples prepared with zinc nitrate.

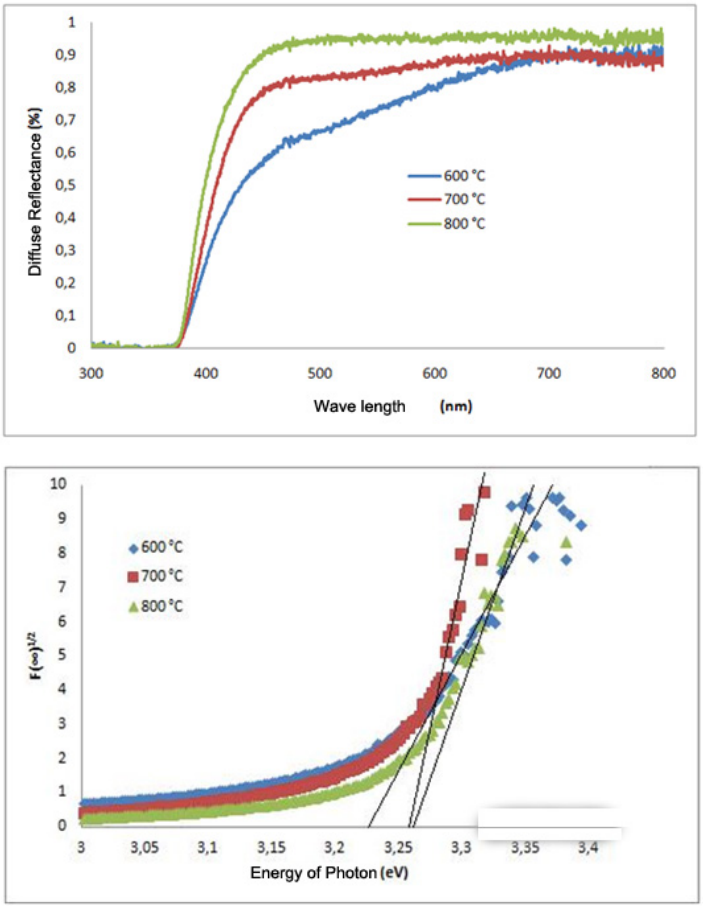

Figure 4-19: Diffuse reflectance and Kubelka-Munk transform of the samples prepared with zinc acetate.

The powders produced by precipitation from zinc acetate and nitrate (called CP) solutions revealed little difference in their optical behavior. They also revealed that the sample prepared with nitrate has a higher reflectance for larger wavelengths (> 400 nm) and a smaller bandgap value, as can be seen in Figure 4-20. The bandgap values are described in Table 4.4.

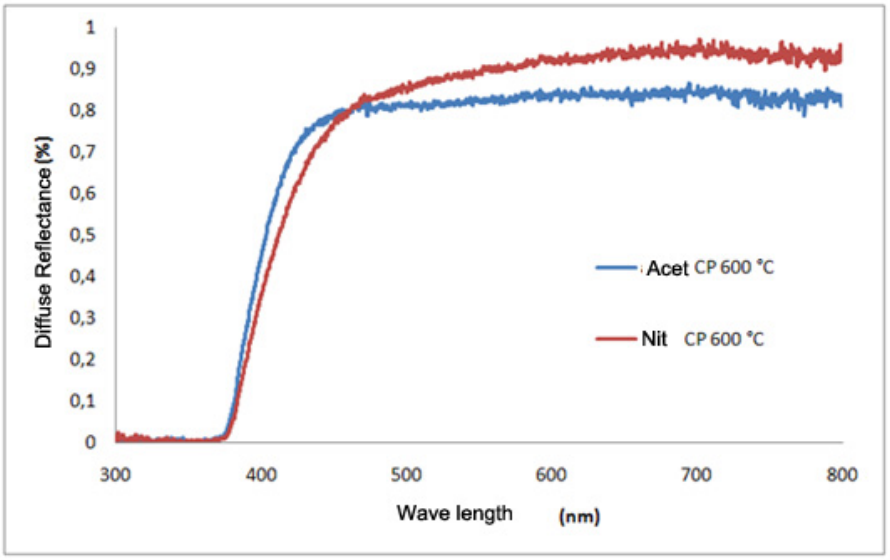

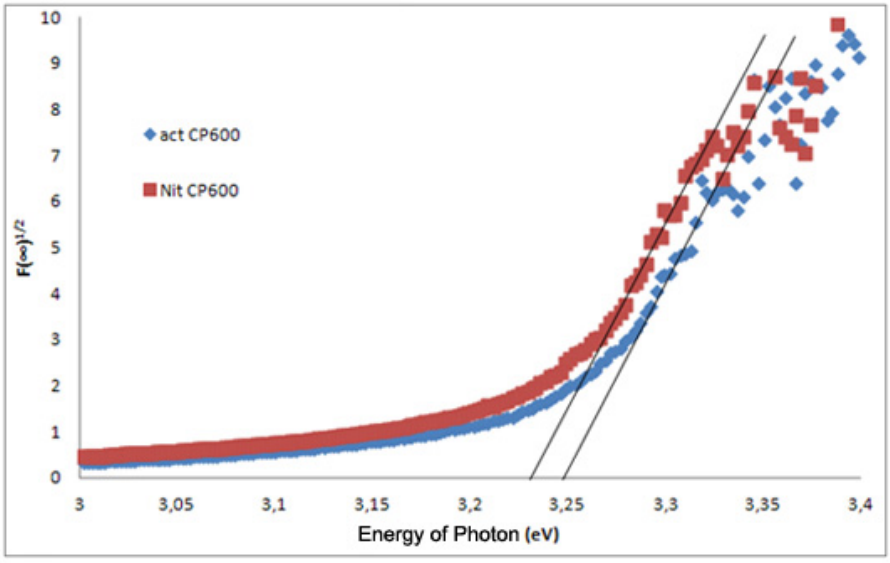

Figure 4-20: Diffuse reflectance of the CP samples prepared using zinc acetate and nitrate

Table 4-4: The bandgap values calculated using the Kubelka-Munk transform.

	Acetate 600°C	Acetate 700°C	Acetate 800°C	Nitrate 600°C	Nitrate 700°C	Nitrate 800°C	Nitrate CP 600°C	Acetate CP 600°C
Bandgap	3.23	3.26	3.26	3.23	3.25	3.23	3.23	3.25

The bandgap values found for the biomimetic and precipitated ZnO are consistent with the values described in the literature. Small variations in the figures are mainly due to experimental errors and/or the presence of impurities in the sample.

When submitted to light, the outermost electrons of ZnO are promoted to higher levels of energy. These electrons tend to return to their states of minimum energy, and when this occurs, the ZnO releases the absorbed energy as light and heat. By analyzing the light emitted by the sample, it is possible to get more information on the bandgap of the material, such as the presence of vacancy-type defects of oxygen.

The results are shown in the photoluminescence graphs of Figure 4-21. In these graphs the presence of two bands of energy emission can be seen. The first band, the narrowest, appears at lower wavelengths (~ 388 nm) and corresponds with Near Band Edge (NBE) emission. The other emission band comprises a broad spectrum of wavelengths (energy), ranging from 400 nm to almost 750 nm. This band is called Deep Level Emission (DLE). The source of these emissions has been discussed in many publications and they are attributed to the presence of both intrinsic and extrinsic defects. As can be seen, the samples prepared with the use of ESMs as templates, generally tend to

have a more intense DLE band than the samples prepared by precipitation. During the calcination process, the growth of ZnO and the expulsion of the organic membrane matter in the form of gas occur simultaneously. These gases may interfere with the growth of ZnO by changing the amount and type of defects present in the material. It is known that the membranes are composed mainly of carbon and hydrogen, with small amounts of sulfur and phosphorus. In the combustion of the membranes, oxygen is consumed. This could cause a local decrease in oxygen pressure and a larger amount of vacancy-type oxygen defects in the sample. Another possibility is the reaction of sulfur of the membranes in the formation of ZnO, which could cause impurities that may provide new possible energy states within the bandgap of ZnO and, therefore, giving rise to new electronic transitions.

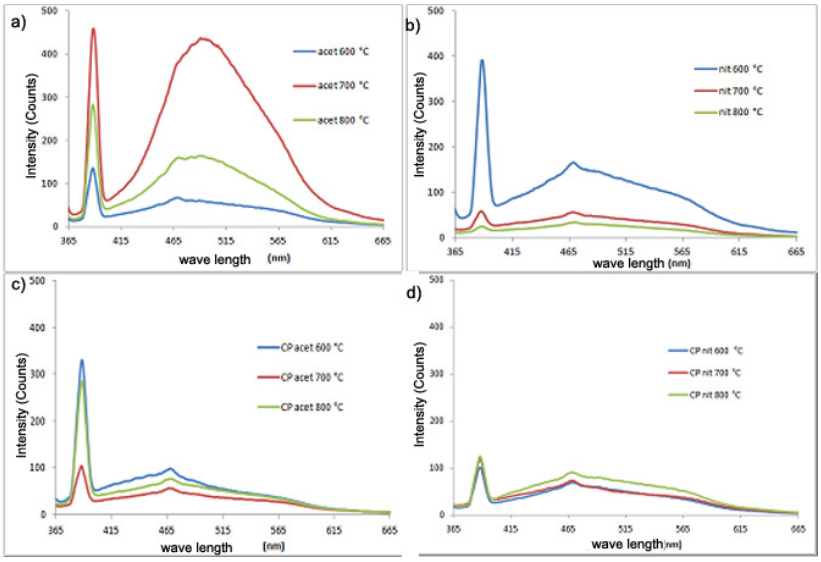

Figure 4-21: Spectrophotometer graphs using samples prepared with ESMs and zinc acetate (a), zinc nitrate (b), and the samples prepared by precipitating with zinc acetate (c) and zinc nitrate (d).

In the samples that were biomimetized using zinc acetate (Figure 4-21a), we can observe that the one calcined at 700°C has the highest deep level emission intensity. However, the

biomimetized samples prepared using zinc nitrate (Figure 4-21b) show a gradual decrease in intensity of the deep level emission band with increasing calcination temperatures, and at 600°C ZnO is obtained with higher emissions in this band. The reactions forming defects that are responsible for this emission probably occur at different temperatures for different precursors. At 800°C, the crystal structure of ZnO has a greater degree of homogeneity and does not show a high deep level emission of. The intensity of the deep level band of biomimetized samples prepared using zinc nitrate decreases gradually with increasing calcination temperature, and at 600°C ZnO is obtained with higher emissions in this band.

The samples prepared by precipitation (Figure 4-21c and Figure 4-21d) did not show an intense deep level emission. As expected, the samples prepared by precipitation have a crystalline network with fewer defects, since they form ZnO without pyrolysis of the ESMs. This is in agreement with the results for crystallite size measured by XRD, which showed faster growth of the crystallite samples produced by precipitation.

4.11 Surface area and porosity of biomimetic TiO_2

A large internal surface area is the primary requirement of a photoelectrode film in DSSCs. This way, more sensitizer molecules can be adsorbed and act as an antenna to capture the incident photons. Nanostructured materials can meet this requirement and form an interconnected porous network, which can increase the surface area by more than 1000 times when compared to solid materials (Xi et al., 2008).

It is of fundamental importance that a DSSC electrode possesses a wide bandgap and a mesoporous structure composed of nanosized particles that are sintered together to enable a good electrical conduction. The sample that was thermally treated at 600°C has the anatase phase with a wide bandgap and a crystallite size value that is suitable for the production of DSSC electrodes. It must be known if the remaining porosity and surface area favor

of this present application. The BET analysis of the samples treated at 600, 700 and 800°C revealed that the products have a large surface area and average pore diameters of a few nanometers. Observing the isotherms curves of the (Figure 4-22) and comparing with the 5 classic types of isotherms described by Brunauer, Deming and Teller, it can be associated that the samples present the Type V isotherm.

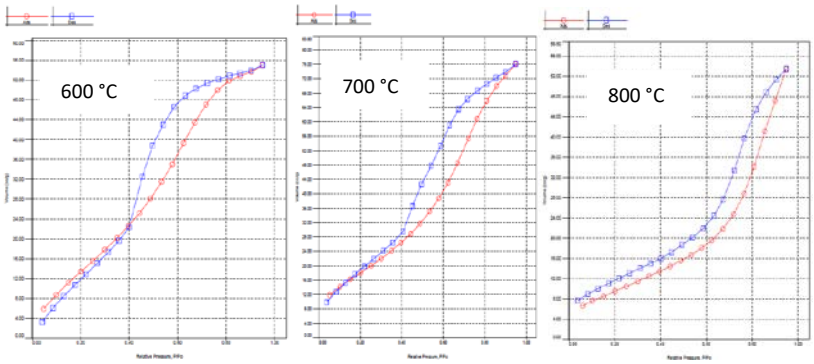

Figure 4-22: Isotherm curves of the TiO_2 samples calcined at 600, 700 and 800°C.

These curves are observed when there is low potential for interaction between adsorbate/adsorbent and when the pores (as is the case here) range from 1.5 to 100 nm. This is consistent with the associated with a surface area from 100 to 200 $m^{2} \cdot g^{-1}$ observed on the BET analysis.

4.12 Characterization of biomimetic and commercial powders used for DSSC production

To investigate the application of ZnO and TiO_2 powders produced by biomimetization of eggshell membranes as Dye Sensitized Solar Cells (DSSC) photoanodes, new biomimetic ZnO and TiO_2 powders were produced and characterized in comparison with similar commercial powders.

The biomimetic synthesis of ZnO and TiO_2, described previously, was carried out using egg shell membranes as templates for the nucleation and growth of ZnO and TiO2 crystals. The precursor solutions were: i.) 0.25 M zinc nitrate in water and ii) 0.05 M titanium isopropoxide in ethyl alcohol for the synthesis of ZnO and TiO_2, respectively. It can be notice that for this studies, the precursor of titanion dioxide was titanium isopropoxide instead titanium tetrachloride. After 24 h immersed in the precursor solutions, the membranes were dried in a drying oven at 100°C for 24h hours and calcined at 600° C for 30 min with 2.5°/min heating ramp. Commercial powders of ZnO P.A. and TiO_2 U.S.P. both brand Synth were purchased and analyzed with biomimetic samples. The samples were named according to Table 4-5:

Table 4-5: Nomenclature adopted for the oxides used.

Material	Biomimetic ZnO	Commercial ZnO	Biomimetic TiO2	Commercial TiO2
Nomenclature	ZnO-B	ZnO-C	TiO_2-B	TiO_2-C

X-ray diffraction analysis revealed the presence of only anatase phase in both commercial and biomimetic TiO_2 powders (Figure 4-23a). In the ZnO powders, only zincite was identified (Figure 4-23b). The difference of the spectra occurred in the intensities and widths of the peaks that showed smaller crystallite sizes for biomimetic powders. The crystallite size measurements are presented in Table 4-6 along with the surface areas calculated by BET.

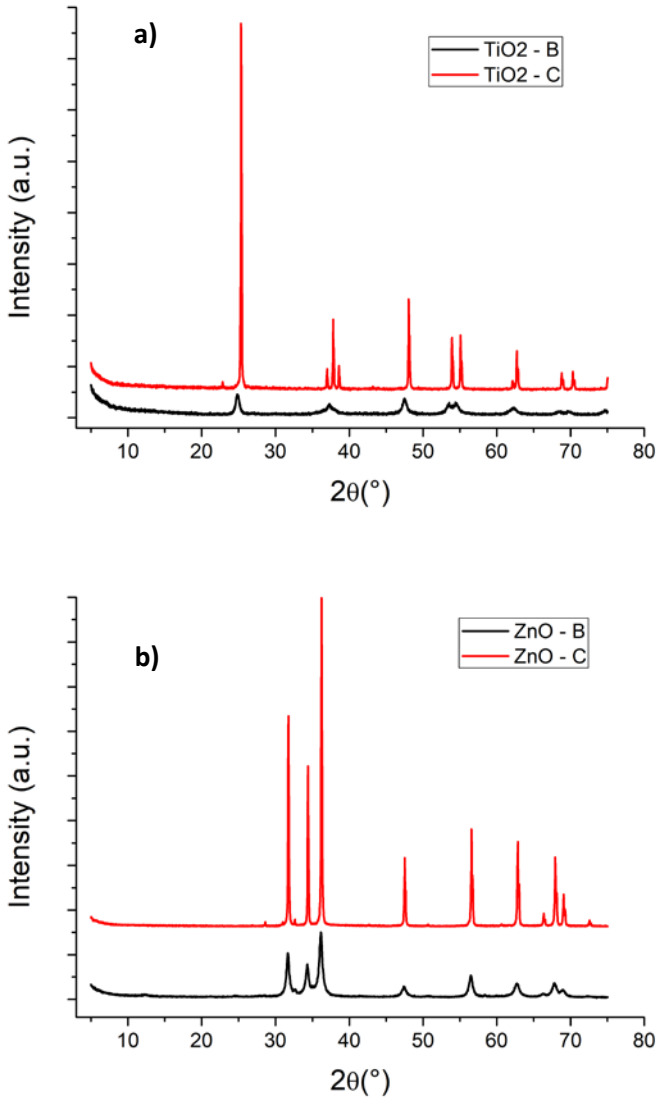

Figure 4-23: a) Diffractogram of the TiO_2 samples revealing the anatase phase. b) Diffractogram of ZnO samples showing zincite crystallization.

Table 4-6: Crystallite sizes measured by the Scherrer equation and surface areas measured by B.E.T.

	ZnO-B	ZnO-C	TiO2-B	TiO2-C
Crystallite size (nm)	10.2	75.5	12.6	86.9
Superficial area (m^2/g)	20.6	8.9	33.2	11.5
Bandgap (eV)	3.04	3.18	3.08	3.23

For a good DSSC performance, the semiconductor must have high values of electron diffusion coefficient (D) and electron recombination lifetime (τ). Nakade et al. (2003) found that for TiO_2 nanoparticles, D increases and τ decreases with increasing crystallite size up to 32 nm and therefore there is an optimal crystallite size.

For the surface area, it is expected that the larger the area, the greater the adsorption tendency of dye molecules. Therefore, biomimetic powders presented promising results regarding performance in DSSCs.

Each route of synthesis of powders leads to powders with different morphological and crystalline characteristics. The presence of crystalline defects may alter the bandgap of the semiconductor, and therefore the optical behavior of these materials should be investigated for the identification of defects as well as observation of changes in the bandgap of oxides.

The results of diffuse reflectance (Figure 4-24) showed a different behavior for the biomimetic and commercial powders since the commercial powders presented a well defined absorption jump in the violet region. It is believed that due to the higher density of crystalline defects present in the biomimetic powders, they have more acceptor and donor levels within their bandgap, causing larger wavelengths to be absorbed by the material as well. The smaller crystallite size verified by the XRD

is indicative more grain boundaries and therefore more defects in the biomimetic samples. Also accordingly to Camaratta et al. (2015), in biomimetic ZnO powders, there may be the presence of impurities such as sulfur and/or phosphorus that can contribute to the formation of point defects that contribute to the modification of the bandgap. From the diffuse reflectance data, the bandgap of the samples calculated with the Kubelka-Munk remission function. The results are presented in Table 1-1.

The calculated bandgaps differ from the results presented on points 4.9 and 4.10 (for similar samples) due to the irregularity of the samples developed from natural eggshells and note from artificially obtained nano-powders fabricated with alternative techniques.

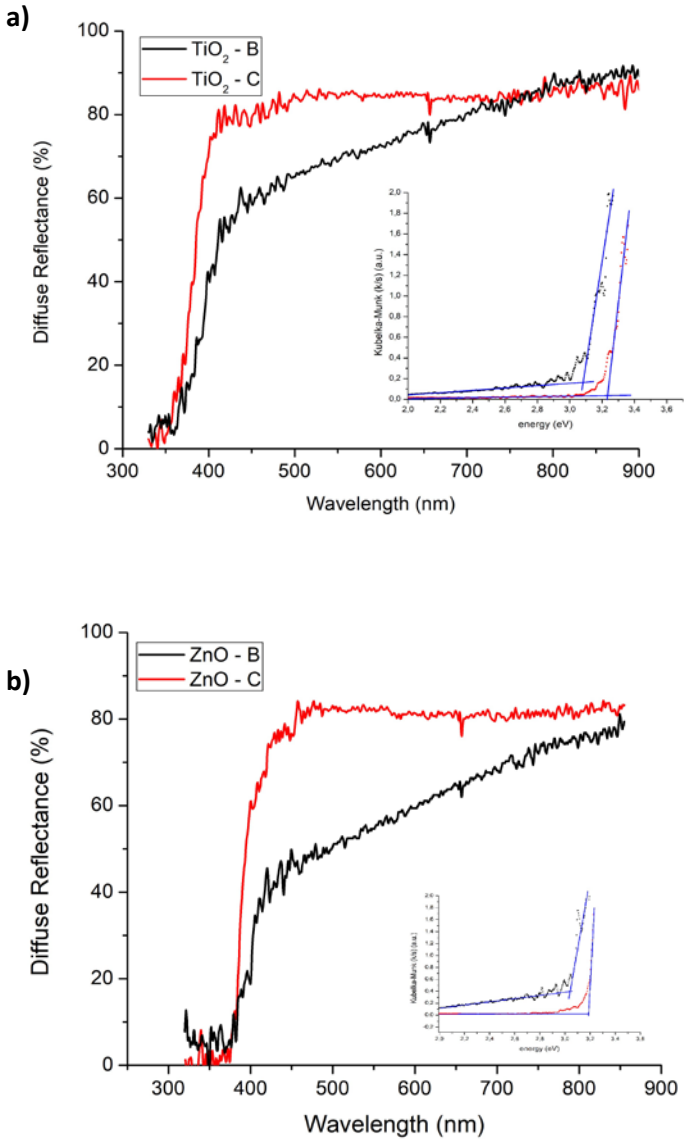

Figure 4-24: Diffuse reflectance analysis. The plot of $(\alpha h\nu)^{1/2}$ vs. $h\nu$ is shown in the inset. a) TiO_2 commercial and biomimetic and (b) ZnO commercial and biomimetic.

SEM analysis (Figure 4-25) of the biomimetic particles revealed the formation of a fragile tubular fibrous structure as well as those reported by other authors (Dong et al., 2007c)(Dong et al., 2007e)(Su et al., 2007). The structure presented by the biomimetic powders favors a higher adsorption of dye molecules because they have high porosity (proved by BET), small crystallite sizes (proven by XRD) and tubular structure that is able to trap dye molecules both on their inner walls as external.

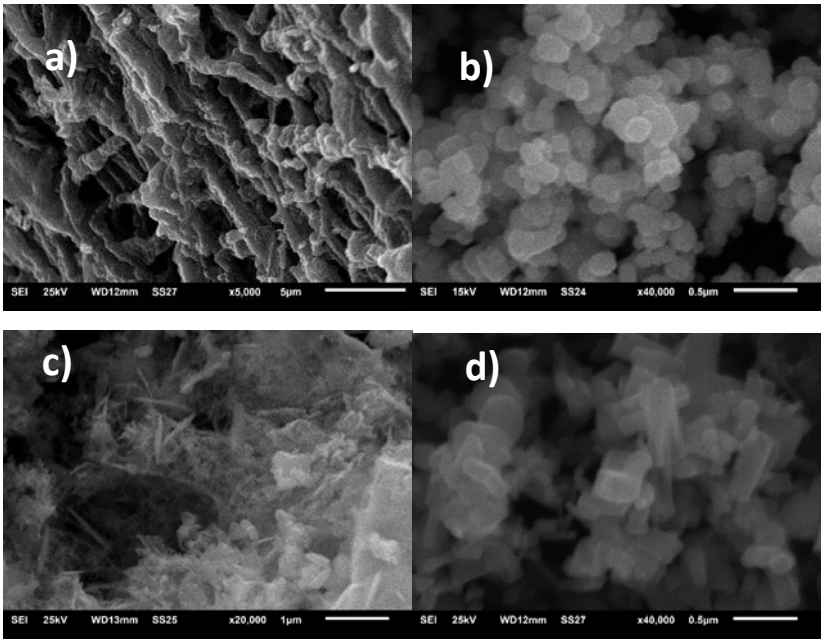

Figure 4-25: SEM images showing the fragile fiber structures of the biomimetic particles and equiaxial aspect of the commercial particles (a) biomimetic TiO_2, (b) commercial TiO_2, (c) biomimetic ZnO and (d) commercial ZnO.

4.13 Characterization of the DSSC produced with biomimetic and commercial powders

The cells assembled with the different powders had two versions each: with dye and without dye. In Figure 4-26 we can

see the great difference in colorations. It is clear that the biomimetic ZnO cell (Figure 4-26h) has become much darker with the presence of the dye, meaning that the porosity of the powders is adequate for the adsorption of large amounts of dye molecules. A similar result occurred with the TiO_2 sample, in which the biomimetic TiO_2 sample (Figure 4-26b and f) presented a higher coloration than its commercial analog (Figure 4-26a and e)

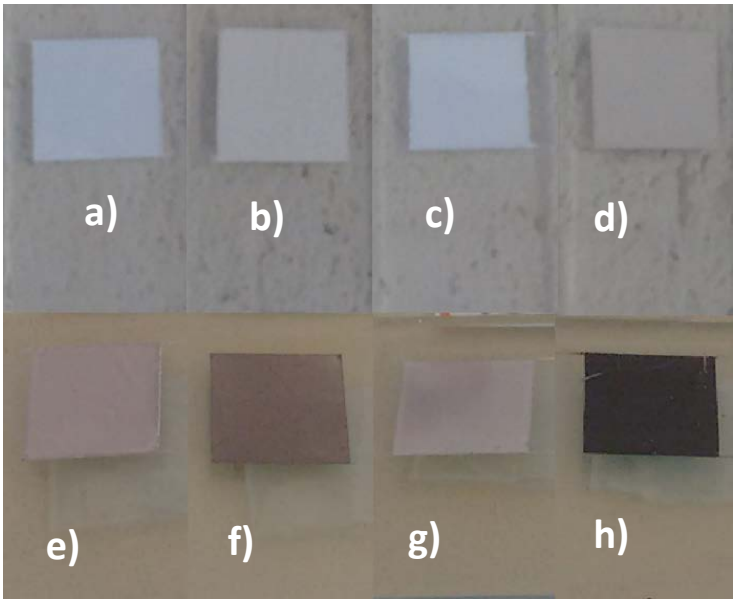

Figure 4-26: Photographs of FTO glass substrates coated with the semiconductor. (a) TiO_2-C without dye; (b) TiO_2-B without dye; (c) ZnO-C-without dye; (d) ZnO-B without dye; (e) TiO_2-C with dye; (f) TiO_2-B with dye; (g) ZnO-C-with dye; (h) ZnO-B with dye.

Analyzing the I-V curves (Figura 4-27) of the different solar cells, we can notice that the cells assembled with biomimetic and commercial TiO_2 had a very similar performance, despite the differences found in commercial and biomimetic powders. It may be noted that in these cells that the presence of the dye was not able to increase their efficiency, but instead decreased both their Voc and Jsc. In the case of ZnO, the dye potentiated the

generation of energy for both biomimetic and commercial powders. A more pronounced effect of the dye for the cell prepared with the biomimetic ZnO is also noted. The results, therefore, indicate that the presence of the N749 dye acted differently for the ZnO and the TiO_2 demonstrating to be more suitable for the use of ZnO.

The data presented show that even with the formation of anatase with small crystallite size, the biomimetic TiO_2 presented a much lower result than the biomimetic ZnO. We believe that biomimetic TiO_2 can have better results in photoconversion when thermally treated at different temperatures needing future work. The results presented by the biomimetic ZnO cells are promising and we believe that the crystalline characteristics such as low crystallite size, high surface area and presence of light absorption defects presented by ZnO-B are characteristics close to the ideal ones for the construction of ZnO DSSCs.

a)

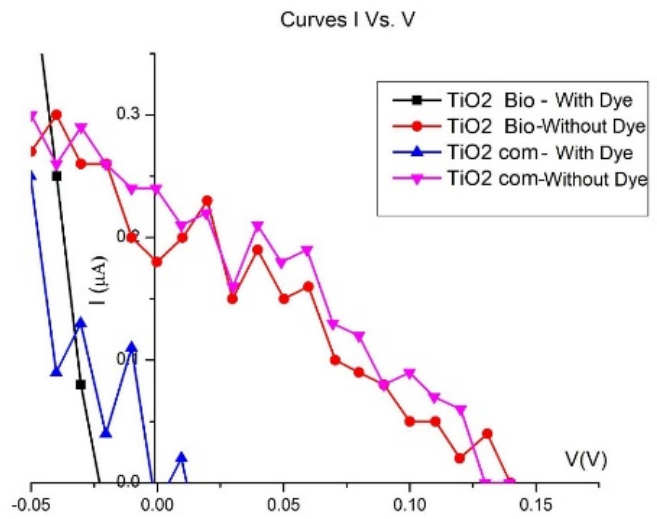

b)

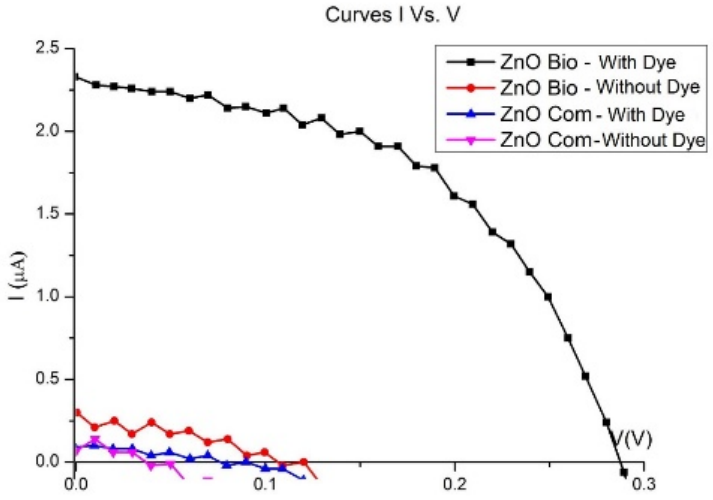

Figura 4-27: I-V curves for (a) TiO_2 cells and (b) ZnO cells.

5-Conclusions

REGARDING THE POSSIBILITY OF OBTAINING ZnO AND TiO_2 REPLICAS OF THE ESM

The microscopic structure of ESMs was replicated at all temperatures tested (600, 700, and 800 °C) for both ZnO and TiO_2.

The synthesis by biomimetization of ESMs, promotes the formation of crystal nuclei for the growth of TiO2 or ZnO (depending on the precursor) through reactions between the ingredients in solution and the bioelements of the ESM fiber surface. The calcination process thermally decomposes the ESMs, leaving only the oxides of interest in the form of a hierarchical network composed of brittle fibers of approximately 1 µm in diameter. This occurs for both oxides tested, as can be observed by SEM. Hierarchical networks of ZnO and TiO2 assembled from small nanocrystals are unusual for these synthesis temperatures.

REGARDING THE COMPARATIVE CHARACTERISATION OF THE OXIDES OBTAINED

The mimicking of the ESMs by both ZnO and TiO_2 showed promising characteristics for the use of these materials in DSSCs

In the case of TiO_2, the calcination temperature primarily affects the crystalline phase formed. At 600 °C anatase nanostructured TiO_2 is obtained and above 700 °C the crystal growth of rutile can be observed. For ZnO, the zincita phase was formed in the biomimetization, with crystallite sizes ranging between 25 and 50 nm for all tested conditions.

The ZnO zincite phase and TiO_2 anatase phase presented optical bandgap values of about 3.25 eV and 3.31 eV, respectively, while the rutile phase of TiO_2 presented a value of 3.07 eV, suggesting that anatase and zincite have greater potential for applications in DSSCs.

The ESMs play an active role in the formation of ZnO, since both the zinc acetate and zinc nitrate aqueous solutions produced replicas of ESM structures. The influence of the biotemplate synthesis could be observed by comparing the crystallite sizes obtained in the synthesis by biomimetization with the crystallite sizes obtained by precipitation of identical solutions without the use of the ESMs. The samples prepared by biomimetization of ESMs had smaller crystallite sizes than those prepared by precipitation from solutions with the same concentration.

The burning of the ESMs leaves some residues of sulfur and, possibly, carbon and phosphorus within the ZnO. These elements were identified by EDS analysis, but apparently did not interfere with the bandgap of biomimetic ZnO

REGARDING THE ASSEMBLY OF A DSSC-TYPE PHOTOVOLTAIC CELL WITH BIOMIMETIC AND COMERCIAL POWDERS

The DSSCs produced with biomimetic and commercial ZnO and TiO_2 with and without dyes demonstrated poor photovoltaic responses, probably due the absence of platinum as catalysator in the counter electrode and the absence of a blocking

layer between the porous layer and the FTO glass, but the performance of the different powders could be compared. The performance of the cells with ZnO biomimetic powders was superior to the performance of the commercial ZnO cells, whereas the TiO_2 cells had similar performance for both powders. The presence of the dye greatly increases the V_{OC} and J_{SC} values in the ZnO cells.

The photovoltaic characterization of the cell assembled with ZnO biomimetic presented distinctly better results than the others, showing the great potential of the use of ZnO biomimetic for the production of DSSCs.

6-References

Addadi, L., Weiner, S., Geva, M., 2001. On how proteins interact with crystals and their effect on crystal formation. Zeitschrift für Kardiologie 90, 92–98.

Aizenberg, J., 2006. Nanomechanics of biological single crystals, in: Nanomechanics of Materials and Structures. Springer, pp. 99–108.

Antonietti, M., Berton, B., Göltner, C., Hentze, H.-P., 1998. Synthesis of mesoporous silica with large pores and bimodal pore size distribution by templating of polymer latices. Advanced Materials 10, 154–159.

Arya, S.K., Saha, S., Ramirez-Vick, J.E., Gupta, V., Bhansali, S., Singh, S.P., 2012. Recent advances in ZnO nanostructures and thin films for biosensor applications. Analytica chimica acta 737, 1–21.

Bach, U., Lupo, D., Comte, P., Moser, J., Weissörtel, F., Salbeck, J., Spreitzer, H., Grätzel, M., 1998. Solid-state dye-sensitized mesoporous TiO2 solar cells with high photon-to-electron conversion efficiencies. Nature 395, 583–585.

Ball, P., 2001. Life's lessons in design. Nature 409, 413–416.

Breulmann, M., Davis, S., Mann, S., Hentze, H.-P., Antonietti, M., 2000. Polymer-Gel Templating of Porous Inorganic Macro-Structures Using Nanoparticle Building Blocks. Advanced Materials 12, 502–507.

Cabrera, S., El Haskouri, J., Beltrán-Porter, A., Beltrán-Porter, D., Marcos, M.D., Amorós, P., 2000. Enhanced surface area in thermally stable pure mesoporous TiO2. Solid State Sciences 2, 513–518.

Camaratta, R., Lima, A.C., Reyes, M., Hernandez-Fenollosa, M., Messana, J.O., Bergmann, C., 2013. Microstructural evolution and optical properties of TiO 2 synthesized by eggshell membrane templating for DSSCs application. Materials Research Bulletin 48, 1569–1574.

Camaratta, R., Messana, J.O., Bergmann, C.P., 2015. Synthesis of ZnO through biomimetization of eggshell membranes using different precursors and its characterization. Ceramics International 41, 14826–14833.

Carp, O., Huisman, C.L., Reller, A., 2004. Photoinduced reactivity of titanium dioxide. Progress in solid state chemistry 32, 33–177.

Caruso, R., Schattka, J., 2000. Cellulose acetate templates for porous inorganic network fabrication. Advanced Materials 12, 1921–1923.

Caruso, R.A., Antonietti, M., 2001. Sol- gel nanocoating: an approach to the preparation of structured materials. Chemistry of materials 13, 3272–3282.

Caruso, R.A., Giersig, M., Willig, F., Antonietti, M., 1998. Porous “coral-like” TiO2 structures produced by templating polymer gels. Langmuir 14, 6333–6336.

Caruso, R.A., Schattka, J.H., Greiner, A., 2001. Titanium dioxide tubes from sol-gel coating of electrospun polymer fibers. Advanced Materials 13, 1577–1579.

Carvalho, A.L.C., 2014. Metodologia para análise, caracterização e simulação de células fotovoltaicas.

Chang, Y.-J., Kong, E.-H., Park, Y.-C., Jang, H.M., 2013. Broadband light confinement using a hierarchically structured TiO 2 multi-layer for dye-sensitized solar cells. Journal of Materials Chemistry A 1, 9707–9713.

Chhabra, V., Ayyub, P., Chattopadhyay, S., Maitra, A., 1996. Preparation of acicular y-Fe2O3 particles from a microemulsion-mediated reaction. Materials Letters 26, 21–26.

Cook, G., Timms, P.L., Göltner-Spickermann, C., 2003. Exact replication of biological structures by chemical vapor deposition of silica. Angewandte Chemie International Edition 42, 557–559.

Davis, S.A., Burkett, S.L., Mendelson, N.H., Mann, S., 1997. Bacterial templating of ordered macrostructures in silica and silica-surfactant mesophases. Nature 385, 420.

Dennis, J.E., Carrino, D.A., Yamashita, K., Caplan, A.I., 2000. Monoclonal antibodies to mineralized matrix molecules of the avian eggshell. Matrix Biology 19, 683–692.

Diebold, U., 2003. The surface science of titanium dioxide. Surface science reports 48, 53–229.

Dong, Q., Su, H., Cao, W., Zhang, D., Guo, Q., Lai, Y., 2007a. Synthesis and characterizations of hierarchical biomorphic titania oxide by a bio-inspired bottom-up assembly solution technique. Journal of Solid State Chemistry 180, 949–955.

Dong, Q., Su, H., Song, F., Zhang, D., Wang, N., 2007b. Hierarchical Metal Oxides Assembled by Nanocrystallites Via a Simple Bio-Inspired Route. Journal of the American Ceramic Society 90, 376–380.

Dong, Q., Su, H., Xu, J., Zhang, D., Wang, R., 2007c. Synthesis of biomorphic ZnO interwoven microfibers using eggshell membrane as the biotemplate. Materials Letters 61, 2714–

2717.

Dong, Q., Su, H., Zhang, C., Zhang, D., Guo, Q., Kiessling, F., 2008. Fabrication of hierarchical ZnO films with interwoven porous conformations by a bioinspired templating technique. Chemical Engineering Journal 137, 428–435.

Dong, Q., Su, H., Zhang, D., Liu, Z., Lai, Y., 2007d. Synthesis of hierarchical mesoporous titania with interwoven networks by eggshell membrane directed sol-gel technique. Microporous and mesoporous materials 98, 344–351.

Dong, Q., Su, H., Zhang, D., Liu, Z., Lai, Y., 2007e. Synthesis of hierarchical mesoporous titania with interwoven networks by eggshell membrane directed sol-gel technique. Microporous and mesoporous materials 98, 344–351.

Dong, Q., Su, H., Zhang, D., Zhang, F., 2006a. Fabrication and gas sensitivity of SnO2 hierarchical films with interwoven tubular conformation by a biotemplate-directed sol-gel technique. Nanotechnology 17, 3968.

Dong, Q., Su, H., Zhang, D., Zhu, N., Guo, X., 2006b. Biotemplate-directed assembly of porous SnO2 nanoparticles into tubular hierarchical structures. Scripta Materialia 55, 799–802.

Douglas, T., 2003. A bright bio-inspired future. Science 299, 1192–1193.

Fan, T.-X., Chow, S.-K., Zhang, D., 2009a. Biomorphic mineralization: From biology to materials. Progress in Materials Science 54, 542–659. doi:10.1016/j.pmatsci.2009.02.001

Fan, T.-X., Chow, S.-K., Zhang, D., 2009b. Biomorphic mineralization: from biology to materials. Progress in Materials Science 54, 542–659.

Fujishima, A., Honda, K., 1972. Electrochemical photolysis of water at a semiconductor electrode. nature 238, 37.

Galoppini, E., Rochford, J., Chen, H., Saraf, G., Lu, Y., Hagfeldt, A., Boschloo, G., 2006. Fast electron transport in metal organic vapor deposition grown dye-sensitized ZnO nanorod solar cells. The Journal of Physical Chemistry B 110, 16159–16161.

Gao, Y., Li, X., Gong, J., Fan, B., Su, Z., Qu, L., 2008. Polyaniline nanotubes prepared using fiber mats membrane as the template and their gas-response behavior. The Journal of Physical Chemistry C 112, 8215–8222.

Gautron, J., Nys, Y., 2007. Eggshell matrix proteins. Bioactive egg compounds 103–108.

Gong, J., Sumathy, K., Qiao, Q., Zhou, Z., 2017. Review on dye-sensitized solar cells (DSSCs): Advanced techniques and research trends. Renewable and Sustainable Energy Reviews 68, 234–246.

Grätzel, M., 2001. Photoelectrochemical cells. Nature 414, 338–344.

Green, M.A., Hishikawa, Y., Warta, W., Dunlop, E.D., Levi, D.H., Hohl-Ebinger, J., Ho-Baillie, A.W., 2017. Solar cell efficiency tables (version 50). Progress in Photovoltaics: Research and Applications 25, 668–676.

Guan, J., Zhang, J., Yu, T., Xue, G., Yu, X., Tang, Z., Wei, Y., Yang, J., Li, Z., Zou, Z., 2012. Interfacial modification of photoelectrode in ZnO-based dye-sensitized solar cells and its efficiency improvement mechanism. RSC Advances 2, 7708–7713.

Haga, Y., An, H., Yosomiya, R., 1997. Photoconductive properties of TiO2 films prepared by the sol-gel method and

its application. Journal of materials science 32, 3183–3188.

Hagfeldt, A., Boschloo, G., Sun, L., Kloo, L., Pettersson, H., 2010. Dye-sensitized solar cells. Chemical reviews 110, 6595–6663.

Hall, S.R., Bolger, H., Mann, S., 2003. Morphosynthesis of complex inorganic forms using pollen grain templates. Chemical Communications 2784–2785.

Hincke, M.T., Nys, Y., Gautron, J., Mann, K., Rodriguez-Navarro, A.B., McKee, M.D., 2012. The eggshell: structure, composition and mineralization. Front Biosci 17, 1266–1280.

Hoa, M.L.K., Lu, M., Zhang, Y., 2006. Preparation of porous materials with ordered hole structure. Advances in colloid and interface science 121, 9–23.

Hong, S., Min, B., Song, J., Kim, H., 2003. Application of cold crucible for melting of UO2/ZrO2 mixture. Materials Science and Engineering: A 357, 297–303.

Hosono, E., Fujihara, S., Honma, I., Zhou, H., 2005. The fabrication of an upright-standing zinc oxide nanosheet for use in dye-sensitized solar cells. Advanced Materials 17, 2091–2094.

Hossain, M., Ghosh, S., Boontongkong, Y., Thanachayanont, C., Dutta, J., 2005. Growth of zinc oxide nanowires and nanobelts for gas sensing applications, in: Journal of Metastable and Nanocrystalline Materials. pp. 27–30.

Huang, J., Kunitake, T., 2003. Nano-precision replication of natural cellulosic substances by metal oxides. Journal of the American Chemical Society 125, 11834–11835.

Hunton, P., 2005. Research on eggshell structure and quality: An historical overview. Revista Brasileira de Ciência

Av'\icola 7, 67–71.

Ishikawa, Y., Matsumoto, Y., 2001. Electrodeposition of TiO2 photocatalyst into nano-pores of hard alumite. Electrochimica Acta 46, 2819–2824.

Izyumskaya, N., Avrutin, V., Özgür, Ü., Alivov, Y.I., Morkoç, H., 2007. Preparation and properties of ZnO and devices. physica status solidi (b) 244, 1439–1450.

Kamada, K., Mukai, M., Matsumoto, Y., 2002. Electrodeposition of titanium (IV) oxide film from sacrificial titanium anode in I 2-added acetone bath. Electrochimica Acta 47, 3309–3313.

Kang, M., 2003. Synthesis of Fe/TiO2 photocatalyst with nanometer size by solvothermal method and the effect of H2O addition on structural stability and photodecomposition of methanol. Journal of Molecular Catalysis A: Chemical 197, 173–183.

Karthikeyan, C., Thelakkat, M., Willert-Porada, M., 2006. Different mesoporous titania films for solid-state dye sensitised solar cells. Thin Solid Films 511, 187–194.

Karuppuchamy, S., Andou, Y., Endo, T., 2013. Preparation of nanostructured TiO2 photoelectrode for flexible dye-sensitized solar cell applications. Applied Nanoscience 3, 291–293.

Kavan, L., O'Regan, B., Kay, A., Grätzel, M., 1993. Preparation of TiO2 (anatase) films on electrodes by anodic oxidative hydrolysis of TiCl3. Journal of Electroanalytical Chemistry 346, 291–307.

Kim, C.-S., Moon, B.K., Park, J.-H., Chung, S.T., Son, S.-M., 2003. Synthesis of nanocrystalline TiO2 in toluene by a solvothermal route. Journal of crystal growth 254, 405–410.

Lagziel-Simis, S., Cohen-Hadar, N., Moscovich-Dagan, H., Wine, Y., Freeman, A., 2006. Protein-mediated nanoscale biotemplating. Current opinion in biotechnology 17, 569–573.

Lee, Y.-J., Lee, J., Park, Y., Yoon, K., 2001. Synthesis of large monolithic zeolite foams with variable macropore architectures. Advanced Materials 13, 1259–1263.

Li, D., Zhou, H., Hibino, M., Honma, I., 2003. Sol-gel Synthesis of Porous Crystalline TiO2-P2O5 Oxide with Thermal Stability. Journal of materials research 18, 2743–2746.

Lim, K.T., Hwang, H.S., Ryoo, W., Johnston, K.P., 2004. Synthesis of TiO2 nanoparticles utilizing hydrated reverse micelles in CO2. Langmuir 20, 2466–2471.

Liu, J., Wu, Q., Ding, Y., 2005. Morphologies-controlled synthesis of CaWO4 crystals by a novel supramolecular template method. Journal of crystal growth 279, 410–414.

Liu, J.-K., Wu, Q.-S., Ding, Y.-P., Yi, Y., 2004. Assembling synthesis of barium chromate nano-superstructures using eggshell membrane as template. Bulletin of the Korean Chemical Society 25, 1775–1778.

Liu, S., Gan, L., Liu, L., Zhang, W., Zeng, H., 2002. Synthesis of single-crystalline TiO2 nanotubes. Chemistry of materials 14, 1391–1397.

Luque, A., Hegedus, S., 2011. Handbook of photovoltaic science and engineering. John Wiley \& Sons.

Meldrum, F.C., Seshadri, R., 2000. Porous gold structures through templating by echinoid skeletal plates. Chemical Communications 29–30.

Morales, A.E., Mora, E.S., Pal, U., 2007. Use of diffuse reflectance spectroscopy for optical characterization of un-

supported nanostructures. Revista mexicana de fIsica 53, 18–22.

Nagaveni, K., Hegde, M., Ravishankar, N., Subbanna, G., Madras, G., 2004a. Synthesis and structure of nanocrystalline TiO2 with lower band gap showing high photocatalytic activity. Langmuir 20, 2900–2907.

Nagaveni, K., Sivalingam, G., Hegde, M., Madras, G., 2004b. Solar photocatalytic degradation of dyes: high activity of combustion synthesized nano TiO2. Applied Catalysis B: Environmental 48, 83–93.

Nakade, S., Saito, Y., Kubo, W., Kitamura, T., Wada, Y., Yanagida, S., 2003. Influence of TiO2 nanoparticle size on electron diffusion and recombination in dye-sensitized TiO2 solar cells. The Journal of Physical Chemistry B 107, 8607–8611.

Nys, Y., Gautron, J., 2007. Structure and formation of the eggshell. Bioactive egg compounds 99–102.

Nys, Y., Gautron, J., Garcia-Ruiz, J.M., Hincke, M.T., 2004. Avian eggshell mineralization: biochemical and functional characterization of matrix proteins. Comptes Rendus Palevol 3, 549–562.

Palomares, E., Clifford, J.N., Haque, S.A., Lutz, T., Durrant, J.R., 2003. Control of charge recombination dynamics in dye sensitized solar cells by the use of conformally deposited metal oxide blocking layers. Journal of the American Chemical Society 125, 475–482.

Pedraza, F., Vazquez, A., 1999. Obtention of TiO2 rutile at room temperature through direct Oxidation of TiCl3. Journal of Physics and Chemistry of Solids 60, 445–448.

Perraud, I., Ayral, R.-M., Rouessac, F., Ayral, A., 2012. Combustion synthesis of porous ZnO monoliths for sulfur

removal. Chemical engineering journal 200, 1–9.

Pillai, V., Kumar, P., Hou, M., Ayyub, P., Shah, D., 1995. Preparation of nanoparticles of silver halides, superconductors and magnetic materials using water-in-oil microemulsions as nano-reactors. Advances in Colloid and Interface Science 55, 241–269.

Poznyak, S., Kokorin, A., Kulak, A., 1998. Effect of electron and hole acceptors on the photoelectrochemical behaviour of nanocrystalline microporous TiO2 electrodes. Journal of Electroanalytical Chemistry 442, 99–105.

Putnam, R., Nakagawa, N., McGrath, K., Yao, N., Aksay, I., Gruner, S., Navrotsky, A., 1997. Titanium dioxide- surfactant mesophases and Ti-TMS1. Chemistry of materials 9, 2690–2693.

Rani, S., Suri, P., Shishodia, P., Mehra, R., 2008. Synthesis of nanocrystalline ZnO powder via sol-gel route for dye-sensitized solar cells. Solar Energy Materials and Solar Cells 92, 1639–1645.

Reis, R., 2003. Biomietics. Current Opinion in Solid State & Materials Science 7, 2.

Robel, I., Subramanian, V., Kuno, M., Kamat, P.V., 2006. Quantum dot solar cells. Harvesting light energy with CdSe nanocrystals molecularly linked to mesoscopic TiO2 films. Journal of the American Chemical Society 128, 2385–2393.

Shin, Y., Li, X.S., Wang, C., Coleman, J.R., Exarhos, G.J., 2004. Synthesis of Hierarchical Titanium Carbide from Titania-Coated Cellulose Paper. Advanced Materials 16, 1212–1215.

Shin, Y., Liu, J., Chang, J.H., Nie, Z., Exarhos, G.J., 2001. Hierarchically Ordered Ceramics Through Surfactant-Templated Sol-Gel Mineralization of Biological Cellular

Structures. Advanced Materials 13, 728–732.

Shin, Y., Wang, C., Exarhos, G.J., 2005. Synthesis of SiC ceramics by the carbothermal reduction of mineralized wood with silica. Advanced Materials 17, 73–77.

Singhal, B., Porwal, A., Sharma, A., Ameta, R., Ameta, S.C., 1997. Photocatalytic degradation of cetylpyridinium chloride over titanium dioxide powder. Journal of Photochemistry and Photobiology A: Chemistry 108, 85–88.

Sivakumar, S., Pillai, P.K., Mukundan, P., Warrier, K., 2002. Sol-gel synthesis of nanosized anatase from titanyl sulfate. Materials letters 57, 330–335.

Spanhel, L., Anderson, M.A., 1991. Semiconductor clusters in the sol-gel process: quantized aggregation, gelation, and crystal growth in concentrated zinc oxide colloids. Journal of the American Chemical Society 113, 2826–2833.

Stone, V.F., Davis, R.J., 1998. Synthesis, characterization, and photocatalytic activity of titania and niobia mesoporous molecular sieves. Chemistry of Materials 10, 1468–1474.

Su, B., Wang, K., Zuo, X., Mu, H., Dong, N., Tong, Y., Bai, J., Lei, Z., 2007. Facile synthesis of ZnO hollow fibres. Bulletin of Materials Science 30, 571–574.

Su, H., Dong, Q., Han, J., Zhang, D., Guo, Q., 2008a. Biogenic Synthesis and Photocatalysis of Pd- PdO Nanoclusters Reinforced Hierarchical TiO2 Films with Interwoven and Tubular Conformations. Biomacromolecules 9, 499–504.

Su, H., Han, J., Wang, N., Dong, Q., Zhang, D., Zhang, C., 2008b. In situ synthesis of lead sulfide nanoclusters on eggshell membrane fibers by an ambient bio-inspired technique. Smart Materials and Structures 17, 015045.

Sugathan, V., John, E., Sudhakar, K., 2015. Recent improvements in dye sensitized solar cells: A review. Renewable and Sustainable Energy Reviews 52, 54–64.

Thieme, M., Schüth, F., 1999. Preparation of a mesoporous high surface area titanium oxo phosphate via a non-ionic surfactant route. Microporous and Mesoporous Materials 27, 193–200.

Thoms, H., Epple, M., Froba, M., Wong, J., Reller, A., 1998. Metal diolates: useful precursors for tailor-made oxides prepared at low temperatures. Journal of Materials Chemistry 8, 1447–1451.

Tsai, S.-J., Cheng, S., 1997. Effect of TiO2 crystalline structure in photocatalytic degradation of phenolic contaminants. Catalysis Today 33, 227–237.

Tullett, S., 1984. The porosity of avian eggshells. Comparative Biochemistry and Physiology Part A: Physiology 78, 5–13.

Valencia, S., Juan Miguel Marín, G.R., 2010. Study of the bandgap of synthesized titanium dioxide nanoparticules using the sol-gel method and a hydrothermal treatment. The Open Materials Science Journal 4, 9–14.

Valtchev, V., Smaihi, M., Faust, A.-C., Vidal, L., 2003. Biomineral-silica-induced zeolitization of Equisetum arvense. Angewandte Chemie International Edition 42, 2782–2785.

Wang, C., Li, Q., Wang, R., 2004. Synthesis and characterization of mesoporous iron-doped TiO2. Journal of materials science 39, 1899–1901.

Wang, X.W., Wang, Y.F., Zeng, J.H., Shi, F., Chen, Y., Jiang, J., 2017. Quantum dot sensitized solar cells: light harvesting versus charge recombination, a film thickness consideration. Chemical Physics Letters.

Watson, S.S., Beydoun, D., Scott, J.A., Amal, R., 2003. The effect of preparation method on the photoactivity of crystalline titanium dioxide particles. Chemical Engineering Journal 95, 213–220.

Wu, T.-M., Rodriguez, J.P., Fink, D.J., Carrino, D.A., Blackwell, J., Capalan, A.I., Heuer, A.H., 1995. Crystallization studies on avian eggshell membranes: Implications for the molecular factors controlling eggshell formation. Matrix Biology 14, 507–513.

Xi, Y., Hsu, Y., Djurivsic, A., Chan, W., 2008. Electrochemical synthesis of ZnO nanoporous films at low temperature and their application in dye-sensitized solar cells. Journal of the Electrochemical Society 155, D595–D598.

Xie, J., Li, Y., Zhao, W., Bian, L., Wei, Y., 2011. Simple fabrication and photocatalytic activity of ZnO particles with different morphologies. Powder Technology 207, 140–144.

Yang, D., Qi, L., Ma, J., 2003. Hierarchically ordered networks comprising crystalline ZrO2 tubes through sol-gel mineralization of eggshell membranes. Journal of Materials Chemistry 13, 1119–1123.

Yang, D., Qi, L., Ma, J., others, 2002. Eggshell membrane templating of hierarchically ordered macroporous networks composed of TiO2 tubes. Advanced Materials 14, 1543–1546.

Yang, P., Zhao, D., Margolese, D.I., Chmelka, B.F., Stucky, G.D., 1998. Generalized syntheses of large-pore mesoporous metal oxides with semicrystalline frameworks. Nature 396, 152–155.

Yin, S., Fujishiro, Y., Wu, J., Aki, M., Sato, T., 2003. Synthesis and photocatalytic properties of fibrous titania by solvothermal reactions. Journal of Materials Processing

Technology 137, 45–48.

Zhang, B., Davis, S.A., Mann, S., 2002. Starch gel templating of spongelike macroporous silicalite monoliths and mesoporous films. Chemistry of Materials 14, 1369–1375.

Zhang, B., Davis, S.A., Mendelson, N.H., Mann, S., 2000. Bacterial templating of zeolite fibres with hierarchical structure. Chemical Communications 781–782.

Zhang, Q., Dandeneau, C.S., Zhou, X., Cao, G., 2009. ZnO nanostructures for dye-sensitized solar cells. Advanced Materials 21, 4087–4108.

Zhang, R., Gao, L., 2002. Preparation of nanosized titania by hydrolysis of alkoxide titanium in micelles. Materials Research Bulletin 37, 1659–1666.

Zhang, X., Yao, B., Zhao, L., Liang, C., Zhang, L., Mao, Y., 2001. Electrochemical fabrication of single-crystalline anatase TiO2 nanowire arrays. Journal of The Electrochemical Society 148, G398–G400.

Zhang, Y.-H., Reller, A., 2001. Nanocrystalline iron-doped mesoporous titania and its phase transition. Journal of Materials Chemistry 11, 2537–2541.

Zhitomirsky, I., 1998. Cathodic electrosynthesis of titanium and ruthenium oxides. Materials Letters 33, 305–310.

Zhu, K., Kopidakis, N., Neale, N.R., van de Lagemaat, J., Frank, A.J., 2006. Influence of surface area on charge transport and recombination in dye-sensitized TiO2 solar cells. The Journal of Physical Chemistry B 110, 25174–25180.

7-Future works

In this doctoral thesis ZnO and TiO_2 powders were synthesized through the biomimetization of egg shell membranes. Therefore, the experience gained from these syntheses will serve as a basis for further investigating the use of the same synthesis process for other metal oxides such as SnO_2, Nb_2O_5, etc.

The phases presented by TiO_2 are very dependent on the heat treatment temperature. In this thesis, solar cells were assembled with low crystallite size anatase, but we believe that because they have a very small crystallite size (being almost an amorphous material), this material does not have adequate electrical conductivity to provide a photocurrent. Studies with the application of TiO_2 with different crystallinities should be conducted to optimize the energy generation with the biomimetic TiO_2.

Still on the study of the application of the biomimetic powders in DSSC, studies with cells constructed not for the simple comparison between different semiconductors, but to reach high efficiencies should be conducted. For this, the cell must be constructed with the presence of a blocking layer, as well as a catalyst in the counter-electrode. For the catalyst, it will be sought to employ the graphene oxide.